Lifetime measurements in the neutron-rich ^{148}Ce nuclide at the low-Z boundary of the $N = 90$ shape-phase transition

Lebensdauermessungen im neutronenreichen Nuklid ^{148}Ce an der niedrig-Z Grenze des $N = 90$ Form-Phasenübergangs

Zur Erlangung des Grades eines Doktors der Naturwissenschaften (Dr. rer. nat.) genehmigte Dissertation von Pavlos Koseoglou aus Herrenberg

Tag der Einreichung: 29. January 2019, Tag der Prüfung: 18. February 2019
Darmstadt — D 17

1. Gutachten: Prof. Dr. Dr. h.c. Norbert Pietralla
2. Gutachten: Prof. Dr. Joachim Enders

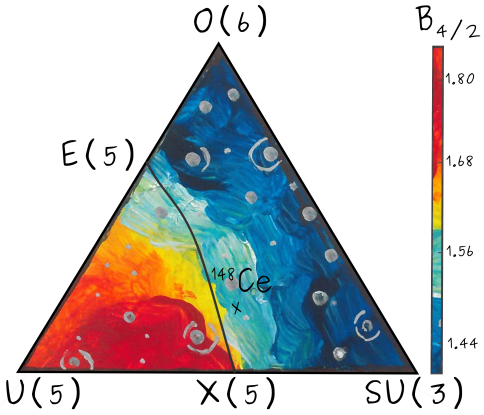

TECHNISCHE UNIVERSITÄT DARMSTADT

Fachbereich Physik
Institut für Kernphysik
AG Pietralla

Lifetime measurements in the neutron-rich ^{148}Ce nuclide at the low-Z boundary of the $N = 90$ shape-phase transition
Lebensdauermessungen im neutronenreichen Nuklid ^{148}Ce an der niedrig-Z Grenze des $N = 90$ Form-Phasenübergangs

Genehmigte Dissertation von Pavlos Koseoglou aus Herrenberg

1. Gutachten: Prof. Dr. Dr. h.c. Norbert Pietralla
2. Gutachten: Prof. Dr. Joachim Enders

Tag der Einreichung: 29. January 2019
Tag der Prüfung: 18. February 2019

Darmstadt — D 17

Bitte zitieren Sie dieses Dokument als:
URN: urn:nbn:de:tuda-tuprints-85923
URL: http://tuprints.ulb.tu-darmstadt.de/8592

Dieses Dokument wird bereitgestellt von tuprints,
E-Publishing-Service der TU Darmstadt
http://tuprints.ulb.tu-darmstadt.de
tuprints@ulb.tu-darmstadt.de

Die Veröffentlichung steht unter folgender Creative Commons Lizenz:
Namensnennung – Keine kommerzielle Nutzung – Keine Bearbeitung 4.0 International
http://creativecommons.org/licenses/by-nc-nd/4.0/

Στην οικογένειά μου

Abstract

A quantum shape phase transition (QSPT) in atomic nuclei is characterized by a sudden change of the shape of the nucleus due to changes in the location of the nuclear potential minimum. A first-order QSPT exists in the transition from spherical shapes to the axially symmetric deformed shapes. There are models describing even-even nuclei in terms of their shape and their oscillations and rotations symmetries, such us the U(5) symmetry (for spherical shapes - vibrator) and SU(3) symmetry (for axially symmetric deformed shapes - rotor). Along the QSPT the spherical minimum, corresponding to a spherical shape, starts vanishing and the deformed one, corresponding to a deformed shape, appears. While the nuclear potentials of a vibrator and a symmetric rotor have one minimum, the potential of a nucleus near the critical point (CP) of the first-order QSPT between them presents the two competing minima. The X(5) model provides some signatures of the isotopes at the CP.

A first-order QSPT is known in the even-even $N = 90$ isotones with $Z = 60 - 66$. With $Z = 58$, ^{148}Ce lies in the low-Z boundary of this transition from spherical to axially symmetric deformed shapes. This nucleus is studied in this work. Key observables revealing the nuclear shape, such as the energy ratio $R_{4/2} = E(4_1^+)/E(2_1^+)$ and the transition strength ratio $B_{4/2} = B(E2; 4_1^+ \rightarrow 2_1^+)/B(E2; 2_1^+ \rightarrow 0_1^+)$, are compared with the predictions from models describing nuclei along this transition and specially near the CP.

The experimental analysis to obtain the lifetimes of the first 2^+ and first 4^+ states of ^{148}Ce using fast-timing techniques is shown in this work. The data were taken within the EXILL&FATIMA campaign performed at the high-flux reactor of the Institut Laue-Langevin in Grenoble, where fission fragments of ^{235}U and ^{241}Pu were measured by a hybrid spectrometer, consisting of high-resolution germanium and fast-responding lanthanum bromide scintillator detectors. The measurement of the lifetime of the first 4^+ state of ^{148}Ce allows the calculation of the $B_{4/2}$ observable and contributes in the study of the shape of the nucleus.

Beside the comparison with the models, the whole N≈90 region is being investigated within the interacting boson model. The shape evolution of the cerium, the neodymium and the samarium chains is studied and shows the importance of the increasing axially asymmetry.

Zusammenfassung

Ein Quantenformphasenübergang (QSPT) in atomaren Kernen wird durch eine plötzliche Veränderung der Kernform auf Grund von örtlichen Verschiebungen der Kernpotentialminima charakterisiert. Ein solcher Phasenübergang erster Ordnung findet sich in der Übergangsregion von sphärischen Atomkernen zu axialsymmetrisch deformierten Atomkernen. Es gibt Modelle, die gerade-gerade Kerne bezüglich ihrer Form und ihrer Vibrations- und Rotationssymmetrien beschreiben, wie z.B. die U(5)-Symmetrie (für sphärische Kerne - Vibratoren) und die SU(3)-Symmetrie (für axialsymmetrisch deformierte Kerne - Rotoren). Entlang des QSPT beginnt das sphärische Minimum (sphärische Formen) zu verschwinden und das deformierte Minimum (deformierte Form) erscheint. Während die Kernpotentiale eines Vibrators und eines Rotors nur ein Minimum besitzen, hat das Kernpotential eines Atomkerns nahe dem kritischen Punkt (CP) eines QSPT erster Ordnung zwei konkurierende Minima. Das X(5)-Modell stellt einige Kennzeichen solcher Isotope am CP bereit.

In den gerade-gerade $N = 90$ Isotonen mit $Z = 60-66$ is ein QSPT erster Ordnung bekannt. Das Isotop ^{148}Ce liegt mit $Z = 58$ bezüglich Z am unteren Ende dieser Übergangsregion zwischen sphärischen und axialsymmetrisch deformierten Kernen. Dieser Kern wird in dieser Arbeit untersucht. Schlüsselobservablen, die Aussagen übe die Kernfom machen, wie das Energieverhältnis $R_{4/2} = E(4_1^+)/E(2_1^+)$ und das Verhältnis der Übergangsstärken $B_{4/2} = B(E2; 4_1^+ \rightarrow 2_1^+)/B(E2; 2_1^+ \rightarrow 0_1^+)$, werden mit Vorhersagen von Modellen verglichen, die Kerne entlang des Phasenübergangs, und insbesondere am CP, beschreiben.

Die Analyse zur experimentellen Bestimmung der Lebensdauer der ersten angeregten 2^+ und 4^+ Zustände von ^{148}Ce unter Benutzung der Fast-Timing Methode wird in dieser Arbeit vorgestellt. Die Daten wurden während der EXILL&FATIMA-Kampagne am Höchstflussreaktor des Instituts Laue Langevin in Grenoble aufgenommen. Spaltfragmente von ^{235}U und ^{241}Pu wurden mittels eines Hybrid Spektrometers, bestehend aus energetisch hochauflösenden Germanium Detektoren und schnellen Szintillationsdetektoren aus Cerium-dotiertem Lanthanumbromid untersucht. Die Messung der Lebensdauer des ersten 4^+-Zustands von ^{148}Ce ermöglicht die Berechnung des $B_{4/2}$-Verhältnisses und trägt zur Untersuchung der Kernform dieses Isotops bei.

Neben dem Vergleich mit Modellen wird die gesamte Region um $N \approx 90$ im Rahmen des Interacting Boson Modells untersucht. Dabei wird die Kernformentwick-

lung in den Iostopenketten von Cer, Neodym und Samarium untersucht und die Bedeutung zunehmend axialler Asymmetrie aufgezeigt.

Contents

1 Introduction - Motivation

There are four fundamental interactions in physics, known as the fundamental forces, namely: the gravitational, the electromagnetic, the strong and the weak interaction [1]. Matter interacts by these four forces following the "laws" of interaction of each one of them. Quarks [2] forms hadrons via the strong interaction. Hadrons, like protons and neutrons, which are clusters of quarks, interact with each other by the nuclear force which is the residuum of the strong interaction between the quarks [3]. Examining the interactions of hadrons experimental data can be provided for testing theories for the nature of this force.

The theories that have been developed try to interpret hadron systems. Such systems are the atomic nuclei, consisting of protons and neutrons. A nucleus consists of a number of nucleons, from 1, for ^{1}H, up to 294, for ^{294}Og [4] which is the hadron-richest system found experimentally so far. The shape of the nucleus depends on the number of hadrons. The understanding of the evolution of the shapes along the nuclear chart can reveal features of the hadrons' interaction.

There are microscopic theories which consider the potential of each hadron individually and examine the interactions between them. Alternatively the theories consider the potential of the whole or the majority of the hadrons, and the analysis is made for the interaction between the mean field and the valance hadrons to analyze the behavior of the nucleus. The macroscopic, also called phenomenological or collective, models consider a collective field that interprets the behavior of the nucleus. This is done because of the complexity of the interactions of a large number of hadrons for which the current computing power of the computers can not carry out the numerical calculations. In both approaches, the results of the calculations are compared with experimental data.

In this work, a region of the nuclear chart where the nuclei consist of a large number of protons and neutrons, with mass numbers larger than 144, will be examined. The evolution of shapes in this region will be studied. In the next sections an introduction to the collective models which will be used, the specific physics case which will be examined and the key experimental observables for the study of this case will be given.

1.1 Collective models

The first Nobel Prize in Physics given to nuclear structure was in 1963 to Eugene Paul Wigner (1/2 of the prize) for his discovery and application of fundamental symmetry principles, and to Maria Goeppert Mayer (1/4) and J. Hans D. Jensen (1/4) for their discoveries concerning nuclear shell structure [5, 6]. The second Nobel Prize in nuclear structure was given in 1975 jointly to Aage Niels Bohr, Ben Roy Mottelson and Leo James Rainwater for their discovery of the connection between collective motion and particle motion in atomic nuclei and the development of the theory of the collective model [7].

The shell model successfully describes spherical nuclei with proton and/or neutron numbers near the magic numbers. Between the magic numbers the deformation increases (see Figure 1.1, the magic numbers are marked with dashed lines). In these areas of the nuclear chart the number of the valance protons or/and neutrons is too large for the shell model to be used because of the complicated and hard to solve (even today) calculations for many-body systems. The collective models can give insight for deformed nuclei and interesting phenomena as the octupole deformation, the shape phase transitions and its critical point (CP).

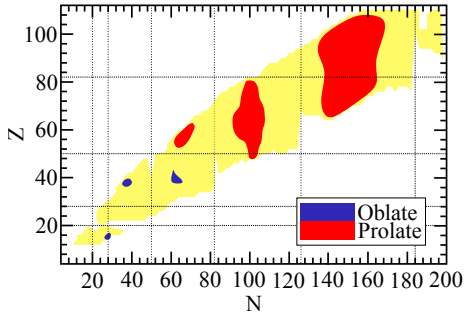

Figure 1.1.: Nuclear deformation chart, all experimentally observed nuclei are shown. The oblate and prolate nuclei are marked with blue and red respectively. The nuclei along the magic numbers, marked with dashed lines, are spherical. The calculations were made using the Hartree-Fock-Bogoliubov theory extended by the generator coordinate method and mapped onto a five-dimensional collective quadrupole Hamiltonian [8].

In quadrupole-collective models the nucleus can be investigated by two collective degrees of freedom, β and γ, instead of the number of valence protons and neutrons. β represents the magnitude of deviation from the spherical shape. The γ

is the angle related to axial symmetry. For γ=0^o the model describes prolate nuclei (rugby ball shape), for γ=30^o the nucleus presents the maximum triaxiality and for γ=60^o the model describes oblate nuclei (pancake shape).

1.2 Interacting Boson Model

In 1974 F. Iachello and A. Arima introduced the interacting boson model (IBM) [9]. The model bridges the collective models with the microscopic theories by replacing pairs of valence protons and neutrons by bosons. In almost empty large shells and only for a small number of bosons this can give good approximation of the system and successfully explain the low energy spectra of heavy nuclei. In the simplified IBM-1 there is no distinction between the proton and neutron, this happens only in IBM-2.

The IBM has a U(6) dynamical symmetry with three sub-symmetries, the U(5), the SU(3) and the O(6), each can describe one of the three main nuclear collective shapes describing even-even nuclei in a sense of their shape and their oscillations and rotations, namely the spherical harmonic vibrator, the symmetric rotor and the γ-soft rotor respectively. The symmetries derive from the symmetry chains shown in Table 1.1. Additionally the $\overline{SU(3)}$ symmetry describes oblate rotors.

In the dynamical symmetries the Hamiltonian can be written in terms of Casimir operators and be solved analytically. The solution of the Hamiltonian can provide observables which can be compared with the experimental data of an isotope and provide information about its shape. The $R_{4/2}$ and $B_{4/2}$ ratios are key fingerprints of the nucleus shape, where $R_{4/2} = E(4_1^+)/E(2_1^+)$ is the energy ratio between the energy of the first 4^+ and the first 2^+ exited states and $B_{4/2} = B(E2;4_1^+ \rightarrow 2_1^+)/B(E2;2_1^+ \rightarrow 0_1^+)$ is the ratio between the transition strengths of the $4_1^+ \rightarrow 2_1^+$ and $2_1^+ \rightarrow 0_1^+$ transitions. As an example one could refer to the spectrum of ^{118}Cd, with $R_{4/2}$=2.39 [10]. The observables of the U(5) symmetry (with typical value of $R_{4/2}$=2) reproduce the experimental data of the isotope and mark it as a spherical nucleus, see Figure 1.2. In the case of ^{166}Er, with $R_{4/2}$=3.29 [10], the experimental data are fitting well with the SU(3) symmetry (with $R_{4/2}$=3.33), marking the nucleus as a prolate symmetric rotor, see Figure 1.2. The reader should keep in his mind that no theoretical model perfectly fits the experimental data of any nucleus.

The three symmetries, of the three main nuclear collective shapes, can be placed at each vertex of a symmetry triangle as shown in Figure 1.3. The "so-called" IBM symmetry triangle (or Casten triangle) [11] is divided in two areas, the spherical-one where nuclei with spherical shape are placed, and the deformed-one where nuclei with deformed shapes are placed. The line on the border of

Table 1.1.: Sub-symmetries of the U(6) dynamical symmetry in the IBM.

Symmetry	Symmetry chain	Main nuclear collective shape described	γ
$U(5)$	$U(6) \supset U(5) \supset O(5) \supset SO(3)$	spherical	0^o
$O(6)$	$U(6) \supset O(6) \supset O(5) \supset SO(3)$	γ-soft rotor	30^o
$\overline{SU(3)}$	$U(6) \supset \overline{SU(3)} \supset SO(3)$	prolate symmetric rotor	0^o
$\overline{SU(3)}$	$U(6) \supset \overline{SU(3)} \supset SO(3)$	oblate symmetric rotor	60^o

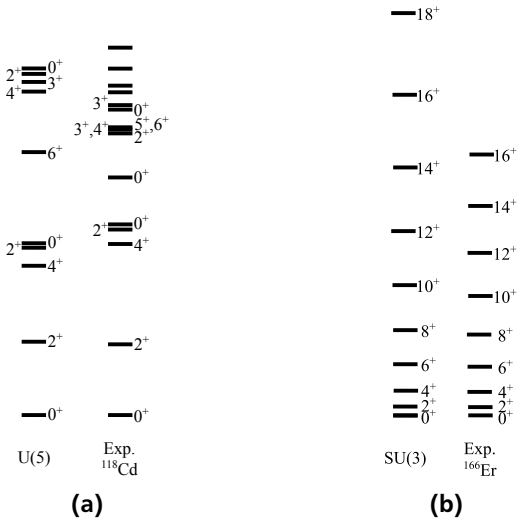

Figure 1.2.: Comparison of (a) ^{118}Cd spectrum with U(5) and (b) ^{166}Er spectrum with SU(3).

the two areas is the transitional area. More about how this line can be defined in the triangle is presented in Chapter 3. The nuclei which are placed along this line undergo a shape phase transition (PT), from spherical to deformed shapes. In the next section the first-order quantum shape phase transition (QSPT) will be discussed, X(5) in Figure 1.3.

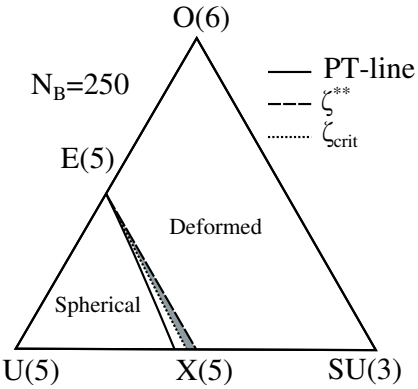

Figure 1.3.: The IBM symmetry triangle (or Casten triangle).

1.3 Quantum Shape Phase Transition

The nuclear potentials of nuclei placed on the U(5) and SU(3) vertexes of the IBM symmetry triangle, calculated using the coherent state formalism of the IBM [12] by equation (3.7) in Chapter 3, are shown in Figure 1.4. One can see the typical shape of the potential of the harmonic oscillator for the nuclei in the U(5) symmetry, which corresponds to a nucleus with a spherical shape. The minimum of the potential is at $\beta=0$. In the potential for the SU(3) symmetry the minimum is at a larger β value, this shape corresponds to a prolate-deformed nucleus.

The E(5) and the X(5) models are geometrical solutions of the Hamiltonian describing nuclei in the CPs of the second- and first-order PT, respectively [13, 14]. E(5) is the CP between U(5) and O(6) and X(5) between U(5) and SU(3). A QSPT in atomic nuclei is characterized by a sudden change of the shape of the nucleus due to changes in the location of the nuclear potential minimum. While the nuclear potentials of a vibrator and a symmetric rotor have one minimum, the potential of a nucleus at the CP of the first-order QSPT between them has two competing minima (Figure 1.4b). Along this PT the spherical minimum, corresponding to spherical shapes, starts vanishing and the deformed one, corresponding to deformed shapes, appears. The CP of the transition is where the contribution of the two minima degenerates.

As it was said earlier in this Chapter, experimental observables for nuclei described by the dynamical symmetries derive from the solution of the Hamiltonian. In the case of the first-order CP the X(5) geometrical solution [14] approaches

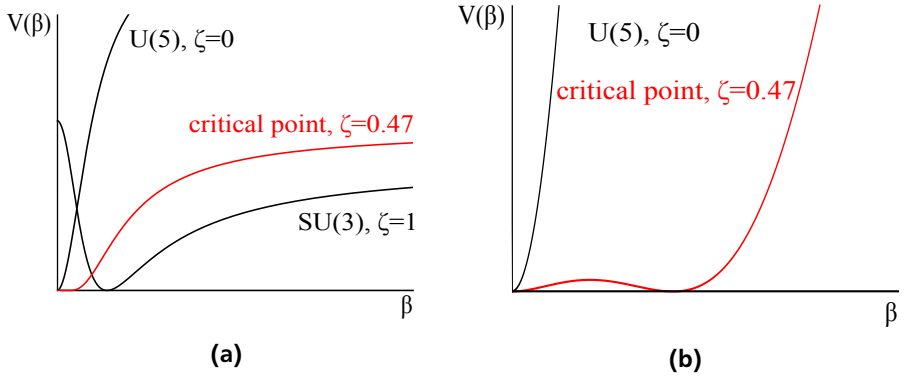

Figure 1.4.: (a) Nuclear potential as a function of the deformation parameter β obtained using the coherent state formalism of the IBM [12] for nuclei in the U(5), SU(3) symmetries and on the CP of the QSPT (χ=0). See equation (3.7) in Chapter 3. (b) Zoom on the β=0 region.

the nuclear potential by neglecting the barrier between the two minima (spherical and deformed, see also red curve in Figure 1.4) and considering the potential as a square-well in the variable β. Fingerprints for this CP can be obtained from the analytical solution. These include the characteristic level schemes and transition strengths, or their ratios. The X(5) model will be described in details in Chapter 2 together with other geometrical models describing the region around this critical symmetry point.

1.4 Physics Motivation - Fingerprints

A first-order QSPT is known in the even-even $N = 90$ isotones with $Z = 60 - 66$ [15]. Using the adopted experimental data [10], the discussed PT can be observed in a $R_{4/2}$ plot of these isotopes over their neutron number (Figure 1.5a). Not all isotopic chains in this PT region show the same behavior. The sharp transitions in the gadolinium and samarium isotopic chains [16, 15, 17] from spherical nuclei ($R_{4/2} = 2 - 2.4$) to deformed ones ($R_{4/2} = 3 - 3.33$) around $N = 90$ are less pronounced in the neodymium and cerium chains. For cerium and neodymium the transitions from $N = 88$ to $N = 90$ are more smooth. To gain additional information for the shape of the nuclei, an other fingerprint, the $B_{4/2}$ ratio ($B_{4/2} = 2$ for spherical symmetry, $B_{4/2} = 1.4$ for γ-rigid and γ-soft deformed), is shown in

figure 1.5b as a function of the neutron number for gadolinium, samarium and neodymium isotopes. In agreement with the picture from the $R_{4/2}$ ratios, the transition from $N = 88$ to $N = 90$ from near spherical symmetry to quadrupole deformed shapes is sharp for gadolinium and samarium and less so for neodymium.

The $R_{4/2} = 2.9$ and the $B_{4/2} = 1.58$ are benchmarks for a nucleus at the X(5) CP [14]. As indicated in Figure 1.5, all $N = 90$ isotopes lie near the X(5) model, hence near the CP of the PT.

In the case of neodymium's and cerium's isotopic chains the smooth behavior of the observables is questioning the point where, or whether at all, the QSPT happens and how sharp the transition is. Additionally, for ^{148}Ce, which is at the low-Z boundary of the N=90 shape PT region, the $B_{4/2}$ ratio was not known, since the lifetime of the first 4^+ state was not measured before this work.

There are analytical solutions of the geometrical Hamiltonian which describe nuclei near the CP, like the X(5)-β^{2n} models [18] and the CBS rotor model [17]. Key observables, such as energy and B(E2) ratios, of these models can be compared with the experimental data of the isotopes near the PT and mark the shape of the nuclei. More about the comparison of the experimental data with the models can be seen in Chapter 2.

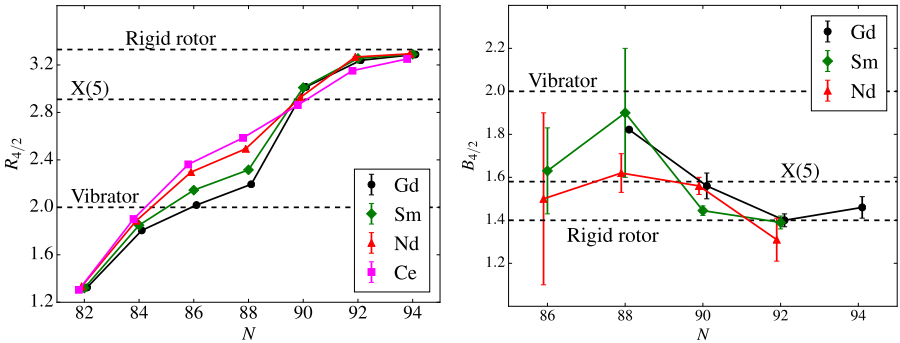

Figure 1.5.: (a) $R_{4/2}$ ratios for Gd, Sm, Nd and Ce isotopic chains as a function of neutron number. The sharp transition of Gd and Sm from spherical nuclei ($R_{4/2} = 2$) to deformed ones ($R_{4/2} = 3.33$) is not present in Nd and Ce chains. (b) $B_{4/2}$ ratios for Gd, Sm and Nd isotopic chains as a function of the neutron number. The transition from $N = 88$ to $N = 90$ from near spherical symmetry to γ-rigid and γ-soft symmetry is sharp for Gd and Sm but not for Nd. Data taken from [10].

The X(5) model, as all models, does not consider the finite number of nucleons in the nucleus [19]. Contrarywise, studies within the IBM-1 have shown the dependence of the values of the benchmarks of the first-order critical symmetry point on the number of valence nucleons [20, 19, 21, 22].

Following the previous, in the next Chapters

- the analysis for the "missing" lifetime of the first 4^+ state of ^{148}Ce will be presented (Chapter 6),
- the experimental data for ^{148}Ce will be compared with geometrical models (Chapter 7),
- the whole phase transitional N=90 region of the nuclear chart will be studied within the IBM-1, aiming in the determination of the CP of each isotopic chain (Chapter 7),
- microscopic calculations for the ^{148}Ce will be presented (Chapter 7).

2 Geometrical models

2.1 Basics

Collective models are of great importance to the understanding of nuclear structure. The liquid drop model [23] is a very good approximation to describe the nuclei shape. Both spherical and deformed shapes can be modeled by the harmonic vibrations and the rotational and vibrational modes of a liquid drop. The surface of the nucleus (liquid drop) can be described by a multiple expansion of the radius [23]

$$R(\theta,\phi) = R_o[1 + \sum_{\lambda\mu} \alpha_{\lambda\mu} Y^*_{\lambda\mu}(\theta,\phi)] \tag{2.1}$$

where R_o is the equilibrium spherical radius, $Y_{\lambda\mu}$ are the standard spherical harmonics and the coefficients $\alpha_{\lambda\mu}$ show the deviations from the spherical shape. The multipolarity of the shape is described by the order of the spherical harmonic λ. The λ=0 term describes fluctuations of the spherical density. The λ=1 term describe possible displacement of the center of mass. The λ=2,3,4 terms correspond to quadrupole, octupole and hexadecapole deformation, respectively. In order to study the low-lying collective structure, where the quadrupole deformation plays the major role (λ=2), by keeping the density constant ($\lambda \neq 0$) and by excluding any displacement of the center of mass ($\lambda \neq 1$), the equation (2.1), for quadrupole deformation reduces to

$$R(\theta,\phi) = R_o\Big[1 + \sum_{\mu} \alpha_{2\mu} Y^*_{2\mu}(\theta,\phi)\Big]. \tag{2.2}$$

The excitations in spherical nuclei refer to shape fluctuations centered around a spherical shape, while the excitations in deformed nuclei refer to shape fluctuations centered around a quadrupole deformed shape. It is convenient to describe the nucleus in a coordinate system fixed in the body of the nucleus with the commonly used β and γ deformation parameters [23, 7]. This is done by relating the

coordinates in the body-fixed system to the coordinates in the space-fixed system through

$$\alpha_\nu = \sum_\mu D^2_{\mu\nu}(\theta_i)\alpha_\mu \tag{2.3}$$

where $D_{\mu\nu}(\theta_i)$ are the transformation functions for the spherical harmonics and θ_i are the three Euler angles. To describe the system in terms of the three Euler angles and the two deformation parameters, usually the frame of reference is chosen such that $\alpha_{21} = \alpha_{2-1} = 0$ and $\alpha_{22} = \alpha_{2-2}$ [24].

By aligning the coordinate axes along the principle axes of the quadrupole shape, the β and γ deformation parameters are related to the $\alpha_{2\nu}$ coefficients as

$$\alpha_{20} = \beta\ \cos\gamma \tag{2.4}$$

and

$$\alpha_{22} = \frac{1}{\sqrt{2}}\beta\ \sin\gamma. \tag{2.5}$$

The parameter β corresponds to the degree of quadrupole deformation and the parameter γ corresponds to the degree of axial asymmetry.

Fully spherical nuclei are described by $\beta = 0$ value. Deformed axially symmetric nuclei are described by non-zero β and $\gamma = 0^o$ values. Prolate deformed nuclei are described by $\beta > 0$ values (American-football-shaped), while oblate deformed nuclei (disk-like for $\gamma = 60^o$) are described by $\beta < 0$. Axially asymmetric deformed nuclei, which are deformed in direction perpendicular to the symmetry axis, are described by non-zero γ values. As the γ value increases from 0^o to 30^o the shape of a deformed nucleus ($\beta \neq 0$) changes from prolate to fully axially asymmetric shapes, the latter nuclei are called γ-soft nuclei.

The Bohr Hamiltonian in the above given parametrization is given by [23, 7]

$$H = -\frac{\hbar^2}{2B}\left[\frac{1}{\beta^4}\frac{\partial}{\partial\beta}\beta^4\frac{\partial}{\partial\beta} + \frac{1}{\beta^2\sin 3\gamma}\frac{\partial}{\partial\gamma}\sin 3\gamma\frac{\partial}{\partial\gamma} - \frac{1}{4\beta^2}\sum_\kappa \frac{Q_\kappa^2}{\sin^2(\gamma - \frac{2}{3}\pi\kappa)}\right] + V(\beta,\gamma) \tag{2.6}$$

where $Q_\kappa$are the angular momentum operators in the Euler angles variables and B is the mass parameter. Different shapes of the potential $V(\beta,\gamma)$ approximates different nuclear shapes. For some shapes (like the spherical) the potential is approximated by a simple analytic function where the Schrödinger equation with the Bohr Hamiltonian can be analytically solved. The solutions give several observables, such us the level energies and the transition strengths of the electromagnetic

decays between levels. The electromagnetic transitions rates can be calculated by the matrix elements of the quadrupole operator

$$T(E2) = t\alpha_{2\mu} \tag{2.7}$$

where t is a scaling factor. The transition strength ($B(E2)$) between two levels (J_i and J_f) is given by

$$B(E2; J_i \rightarrow J_f) = \frac{1}{2J_i + 1} |\langle \psi_f || T(E2) || \psi_i \rangle|^2. \tag{2.8}$$

For some nuclear shapes the potential used depends only on β, this allows separation of the β and γ variables [25]. Such as for spherical nuclei with $V(\beta) = \frac{1}{2} C\beta^2$. In this case the solution of the Schrödinger equation with the Bohr Hamiltonian is analytical solvable in the U(5) dynamical symmetry. The same occurs for axially symmetric deformed nuclei in the SU(3) dynamical symmetry.

It has been found [26, 27] that the shape PT between spherical, U(5), and γ-soft, O(6), shapes is second-order, while the transition between spherical, U(5), and symmetric axially deformed shapes, SU(3), is first-order. Both are described within the framework of the Bohr Hamiltonian. The second-order transition is described by the E(5) model [13], while the first-order transition is approximated by the X(5) model [14].

In the β potential of a spherical vibrator, U(5), one minimum appears in the $\beta = 0$. In the β potential of a deformed nucleus the minimum appear on a non-zero β value. As the shape evolves from spherical to deformed, for a region near and around the CP the two minima coexist and compete. At the CP of the PT the contribution of the two minima to the shape of the nucleus degenerates.

In both E(5) and X(5) CPs the β potential can be approached by a infinite square-well potential as shown in Figure 2.1. The difference between the two models stems from the γ dependence taken in the Hamiltonian. For E(5) the analysis is simpler cause the Baohr Hamiltonian is independent of the γ degree of freedom. This allows an exact analytic solution which describes the CP of the U(5)-O(6) shape PT by the separation of the two structural parameters. For X(5) this separation of the structural parameters is not possible to be done in the same way.

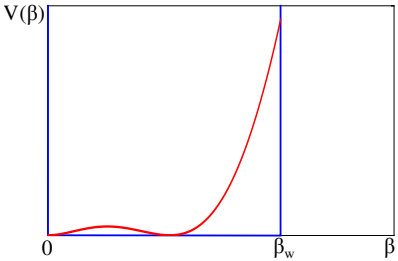

Figure 2.1.: Nuclear potential as a function of the deformation coordinate β on the CP of a shape PT (red). The infinite square-well potential (blue) used to approach the β potential.

2.2 X(5)

An approximate analytic solution is taken for the CP by exploiting the special character of the potential at this point (shown in Figure 2.1) and by an approximate separation of the two structural parameters. The β-part of potential is considered as an infinite square-well, with β_w the position of the right wall,

$$V(\beta,\gamma) = \left\{ \begin{array}{ll} 0, & \text{for } \beta \leq \beta_w \\ \infty, & \text{for } \beta > \beta_w \end{array} \right\} + V_\gamma(\gamma).$$

The $V_\gamma(\gamma)$ includes the axially symmetric degree of freedom. The γ-part of the potential is considered as a harmonic oscillator. By this assumption and the analytical solution the level structure of a nuclei in the spherical to axially symmetric deformed QSPT derives, together with the transition strengths between them. These observables are plotted in Figure 2.2 and comprise fingerprints of a nucleus on the CP of the PT.

The levels derive from the X(5) model are classified by the quantum number s (giving the different bands) and J specifying the angular momentum. For the $s = 1$ both the energy spacing and the transition strengths within the band are between the values of the U(5) and the SU(3) symmetries. The two observables which are strongly related and considered to be benchmarks of any symmetry are the $R_{4/2}$ and the $B_{4/2}$ ratios. For X(5) are $R_{4/2}$=2.9 and $B_{4/2}$=1.58. Another key observable of the CP is the placement of the $s = 2$ band. The energy ratio $E_{0_2^+}/E_{2_1^+}$ for X(5) is 5.65.

Nuclei with $R_{4/2}$<2.9 are consider to be before the CP of the QSPT, to be mostly spherical since the main contributor to their shape is the spherical minimum, on

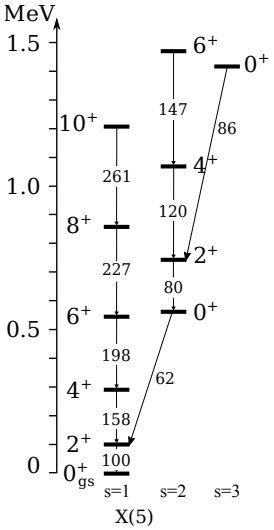

Figure 2.2.: Level scheme and transition strengths derive from the X(5) model.

the other hand, nuclei with $R_{4/2}>2.9$ are considered to be deformed. In the IBM symmetry triangle, introduced in Chapter 1 and discussed in details in Chapter 3, the first will be placed on the left side of the X(5), towards U(5), and the latter on the right side of it, towards SU(3). Of course it has to be noted that this is the case for axially symmetric nuclei ($\gamma=0^o$).

2.3 Solutions along the QSPT: X(5)-β^{2n} and CBS models

There are geometrical solutions of the Hamiltonian which describe nuclei near the CP, like the X(5)-β^{2n} models [18] and the "confined β-soft" (CBS) rotor model [17]. In the big picture, one could say that the X(5)-β^{2n}, the X(5) and the CBS models can describe nuclei along the U(5) to SU(3) transition for axially symmetric nuclei, either before (X(5)-β^{2n}) or after (CBS) the CP in terms of increasing deformation of the potential's minimum. In both models the γ term of the potential is considered to be a harmonic oscillator.

The β term of the potentials in X(5)-β^{2n} models are of the form $u_{2n}(\beta) = \beta^{2n}/2$, with n being an integer. Starting with the harmonic oscillator for $n = 1$, the potentials approach the infinite square-well of X(5) by increasing n (see Figure 2.3a). Parameter-free (up to overall scale factors) observables emanate for each

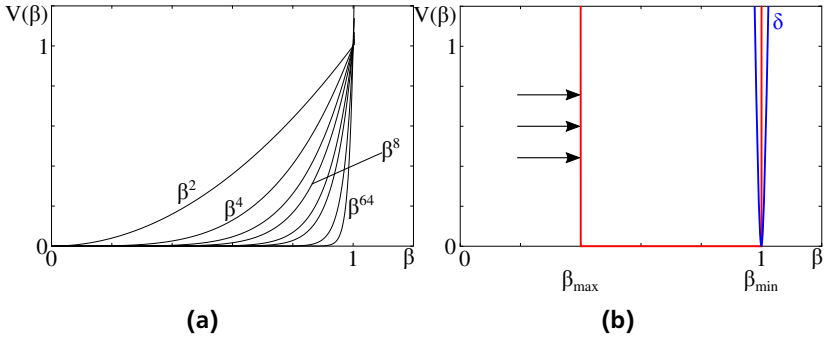

Figure 2.3.: Approximations of the β potentials for (a) the X(5)-β^{2n} and (b) CBS models.

n value. The $R_{4/2}$ for n=1, n=2, n=3 and n=4 are 2.64, 2.78, 2.84 and 2.85, respectively. These values are between the $R_{4/2}$=2 of a spherical nucleus and the $R_{4/2}$=2.9 of the X(5) CP. The same picture occurs for the energy ratio $E_{0_2^+}/E_{2_1^+}$, for large n the values approach the X(5) value. Nuclei with $R_{4/2}$ ratios smaller than the X(5) benchmark, in principle, can be described by one of the X(5)-β^{2n} models and marked as spherical, since the spherical minimum is the one which dominates the potential.

The CBS model considers as potential an infinite square-well with a moving wall. For different widths of the well the model describes nuclei between the CP and the fully axially symmetric deformed shape, the shape of a rigid-rotor [15]. The $r_\beta = \beta_{min}/\beta_{max}$ parameter describes the width of the well, with β_{min} the position of the moving wall of the well and β_{max} the position of the stable wall of the well, see Figure 2.3b. For $r_\beta = 0$ the potential is equivalent to X(5)'s infinite square-well and by increasing r_β ($r_\beta \to 1$) the model approach the rigid-rotor (δ function on β_{max}). As the width of the well is getting narrower the $2_1^+ \to 0_1^+$ energy difference shrinks by a larger fraction than the $4_1^+ \to 2_1^+$ difference. Hence the $R_{4/2}$ ratio of the ground band increases with increasing r_β up to the limit of the rigid-rotor ($R_{4/2} = 3.33$ for $r_\beta \to 1$). The model can be used to describe nuclei with $R_{4/2}$>2.9 and mark them as deformed nuclei. In the N=90 QSPT region the model was used, for different r_β values, to describe the even-even $^{152-156}$Sm [17] and $^{150-156}$Nd [28] isotopes analytically.

One of the most important feature of these two models (X(5)-β^{2n} and CBS) is the capability of changing the model parameter (n and r_β) in order to describe nuclei of a, shape-wise, evolving isotopic or isotonic chain.

3 IBM-1

In the framework of the IBM Arima and Iachello describe collective excitations of nuclei in terms of bosons as pairs of valence fermions [29]. Whereas the geometrical models presented before, the IBM has been proven, for the first time in the Sm isotopic chain [30], to be able to describe the collective properties of nuclei with a large range of structures.

3.1 Basics

Key features of the IBM can be considered the connections of it with the phenomenological geometric approach, which give the advantage of exact solutions (sometimes analytical), and the bonds to the microscopic foundations (shell model) [31], by assigning the bosons to valence nucleons. These valence nucleons are assumed to be the only ones contributing to any low-lying excitations. In the model these low-lying collective excitations in the medium-heavy nuclei can be studied as excitations of bosonic pairs with angular momenta $L = 0$ and $L = 2$. The model is structured by two bosons, the s boson, with angular momentum and parity $\lambda^{\pi} = 0^{+}$, and the d boson, with $\lambda^{\pi} = 2^{+}$. Bosons with higher momenta, L, can be included in the model space in order to describe certain collective states. In the present work they will not be discussed.

The main idea of using bosons instead of fermions comes from the *bosons mapping* techniques where, in order to solve the many-fermion Schrödinger equation and find the transition matrix elements between eigenstates, the fermion operators are replaced with boson operators using only a minimal number of boson degrees of freedom.

The simpler version of the IBM is the, so called, sd-IBM-1 or IBM-1. In a more simplified model, a single boson, the "s+d", represent a fermion pair, with no distinction between protons and neutrons [29]. With total boson number the $N_B = (n_\pi + n_\nu)/2$, where n_π is the valence proton and n_ν is the valence neutron numbers. In IBM-1 the model is treated as a six-dimensional space, as a U(6) algebraic group. This is because the s bosons, with momenta $L = 0$, have one magnetic substate, and d bosons, with $L = 2$, have five magnetic substates. The s and d bosons can be created and annihilated by the corresponding operators, the $s^{\dagger}$,$d^{\dagger}$ creation operators and the $\tilde{s}$,$\tilde{d}$ annihilation operators.

The "generators" of the U(6) group are the following 36 operators, $s^\dagger\tilde{s}$, $s^\dagger\tilde{d}_\mu$, $d^\dagger_\mu\tilde{s}$ and $[d^\dagger_\mu\tilde{d}_\mu]$, with L=0,1,2,3,4 and $|\mu| \leq L$. All operators are close on commutation, which means that for any pair of A and B in the group, either A or B commute, or [A,B] is equal to a linear combination of the other members of the group. The boson number N_B is the "Casmir operator" of the U(6) group, which can be expressed in terms of s and d creation and annihilation operators as

$$N_B = s^\dagger\tilde{s} + d^\dagger\tilde{d}, \tag{3.1}$$

commutes with all generators of the group. This means that all 36 generators of the U(6) group conserve the boson number and make it a "good" quantum number for all states in the IBM-1.

The connection of the model with the collective picture for even-even nuclei is made through the three dynamical sub-symmetries of the U(6) group. Each one of them is related with one of the three main collective models (vibrational, rotational and γ-soft). From 1976 to 1979 the model was investigated in three limits, the vibrational limit [32] using the U(5) sub-symmetry, the rotational limit [33] using the SU(3) sub-symmetry and the O(6), γ-soft, limit [34] using the O(6) sub-symmetry. For each of the limits many observables have been calculated, such as the low-energy spectra (energies of the low-lying states) and transition strengths between the low-lying states of even-even nuclei. Beside the three main collective models the IBM-1 is able to describe nuclei in the transitional region from one to an other symmetry.

3.2 IBM Consistent Q Formalism

For nuclei in a PT the Hamiltonian its more efficient, parameter-wise, to be expressed in the standard notation of the extended constant Q formalism (ECQF) [35, 36, 37],

$$H = \epsilon\hat{n}_d - \kappa\hat{Q}^\chi\hat{Q}^\chi, \tag{3.2}$$

$$H = c[(1-\zeta)\hat{n}_d - \frac{\zeta}{4N_B}\hat{Q}^\chi\hat{Q}^\chi], \tag{3.3}$$

where

$$\zeta = \frac{4N_B}{(\frac{\epsilon}{\kappa} + 4N_B)} \tag{3.4}$$

and

$$\hat{Q}^{\chi} = (s^{\dagger}\tilde{d} + d^{\dagger}\tilde{s}) + \chi(\tilde{d}d^{\dagger})^{(2)} = T(E2)/e_B. \tag{3.5}$$

Q^{χ} is the quadrupole operator, T(E2) is the electric quadrupole transition operator with the effective boson charge e_B, with $\hat{n}_d = \tilde{d}d^{\dagger}$ the d-boson number operator, $\epsilon = c(1-\zeta)$ and $\kappa = -\frac{c\zeta}{4N_B}$. Where c is a scaling factor and N_B the number of valence bosons.

In equation (3.2) the first part has higher symmetry and the second one lower symmetry, in other words for every nucleus the ratio ϵ/κ (or ζ) is representing the competition between spherical and deformed shapes [15].

The ζ and χ are used as structural parameters in the IBM. The IBM symmetry triangle can be mapped with $\zeta \ni [0,1]$ and $\chi \ni [-\sqrt{7}/2, 0]$ parameters, see Figure 3.1. With this parametrization the three collective symmetries have the following coordinates: U(5): $\zeta = 0$ and any χ, SU(3): $\zeta = 1$ and $\chi = -\sqrt{7}/2$ and O(6): $\zeta = 1$ and $\chi = 0$.

The parameters (ζ,χ) can be plotted in the symmetry triangle by converting them into the polar coordinates [38]

$$\rho = \frac{\sqrt{3}\zeta}{\sqrt{3}\cos\theta_{\chi} - \sin\theta_{\chi}} \quad \text{and} \quad \theta = \frac{\pi}{3} + \theta_{\chi}, \tag{3.6}$$

where $\theta_{\chi} = (2/\sqrt{7})\chi(\pi/3)$.

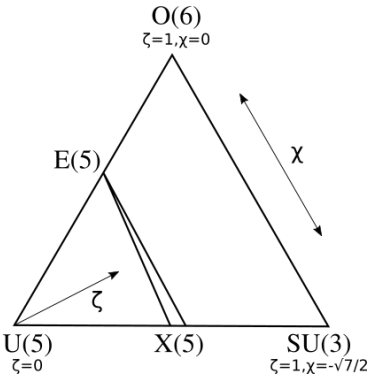

Figure 3.1.: The IBM symmetry triangle can be mapped with the $\zeta \ni [0,1]$ and the $\chi \ni [-\sqrt{7}/2, 0]$ parameters.

An other important and useful feature of the IBM-1 is its connection with the Bohr-Mottelson geometrical deformation parameters β and γ [7] through the Coherent State Formalism [39, 40]. By the work of van Isacker and Chen in Ref. [41], an expression of the energy potential surface, also called scaled total energy ($\mathscr{E}$), for the ground state of the system under study, in terms of the Hamiltoniam parameters and β and γ, was derived. The energy potential surface, $\mathscr{E}(\beta,\gamma)/(cN_B)$, which in the ECQF has the form

$$\begin{aligned}\mathscr{E}(\beta,\gamma) &= \frac{\beta^2}{1+\beta^2}\left[(1-\zeta)-(\chi^2+1)\frac{\zeta}{4N_B}\right] \\ &\quad -\frac{5\zeta}{4N_B(1+\beta^2)}-\frac{\zeta(N_B-1)}{4N_B(1+\beta^2)^2} \\ &\quad \times\left[4\beta^2-4\sqrt{\frac{2}{7}}\chi\beta^3\cos 3\gamma+\frac{2}{7}\chi^2\beta^4\right], \end{aligned} \tag{3.7}$$

was computed from the general IBM-1 Hamiltonian [41, 24]. More informations for this equation can be found in the references given above. In this work it will be used to plot the energy potential surface of nuclei for the three collective shapes (on the three sub-symmetry limits) and of the isotopes along the shape PT under investigation. Qualitatively speaking, the energy potential surface and the nuclear potential of a nucleus show the same shape [12]. Therefore, from now on conclusions for the shape of nuclear potential will be derived from the shape of the energy potential surface, $V(\beta)$.

In Figure 3.2 the total scaled energy is plotted over β for nuclei at the U(5), SU(3) and O(6) symmetries. At the U(5) symmetry the potential shows the typical shape of a vibrator. The minimum is at $\beta=0$. For a nucleus at the SU(3) symmetry a minimum appears in the potential at $\beta_{SU(3)}$, with $\beta_{SU(3)}>0$. This minimum is called "deformed" because a wave function of an eigenstate of a Hamiltonian with this potential would exhibit a deformed probability distribution. For a nucleus at the O(6) symmetry again a minimum appears at $\beta_{O(6)}$, with $\beta_{SU(3)}>\beta_{O(6)}>0$.

What is interesting to investigate, in the frame of the transitional region of the present study, is the evolution of the shape of the nuclear potential along the U(5) to SU(3) shape PT. For this equation (3.7) was used for $N_B=250$, in order to stay far from effects from the finite boson number (more informations on this later in this Chapter), $\gamma=0$ and $\chi=-1.32$ in order to stay on the U(5)-SU(3) leg of the symmetry triangle and not include any effect due to increasing γ-softness. In Figure 3.3 the energy potential surface is plotted for several ζ values, from 0 to 0.5, from U(5) to SU(3) respectively. For $\zeta=0$ only the spherical minimum is present. As ζ increases, the deformed minimum appears. For $\zeta=0.47$ the two minima degenerate. As

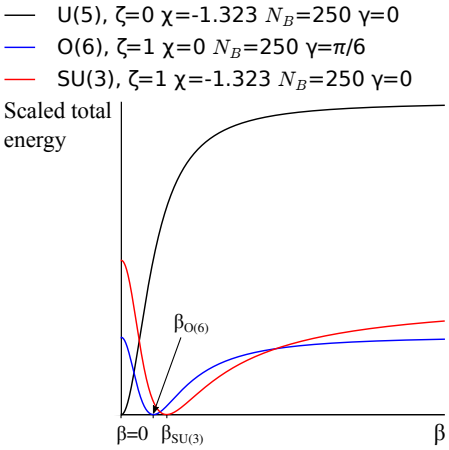

Figure 3.2.: The energy potential surface obtained using the ECQF of the IBM [12] for nuclei in the the three symmetries. The curves were calculated, using equation (3.7), for N_B=250, ζ, γ and χ according to the text for each symmetry.

ζ increases more, the deformed minimum is getting the main contributor to the shape of the nucleus and the spherical miminum disappears.

It is often formulated that the CP of the first order shape transition is at the point where the degeneration of the two minima happens. So the degeneration of the two minima can work as a good benchmark of the CP [1]. So, as it is shown in Figure 3.3, the CP along the U(5)-SU(3) leg of the symmetry triangle is at ζ=0.47 and χ=0. The calculations have been made for N_B=250.

3.3 Phase Transition lines

From equation (3.3) is clear that ζ can work as a parameter defining how spherical is a nucleus. Spherical nuclei are described by small ζ. As ζ increases the deformed minimum on the potential appears and increasing against the spherical. The deformed minimum appears where $\partial^2\mathscr{E}/\partial\beta^2|_{\beta\neq 0} = 0$, for ζ^*, analytical expression in

[1] The reader should notice that in a more correct description of the CP, it should be said that the CP is at the point where the degeneration of the effect of the two minima happens.

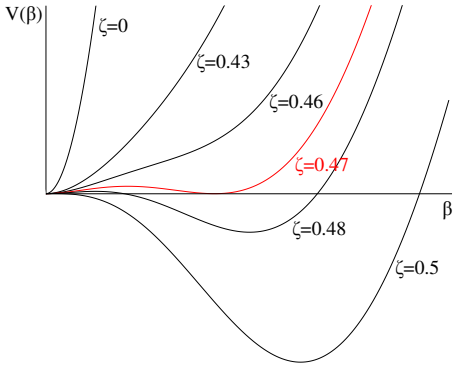

Figure 3.3.: Evolution of the energy potential surface near the first order CP. The curves were calculated for N_B=250, γ=0, χ=-1.32, using equation (3.7).

Ref. [24, 12]. The degeneration of the two minima occurs where the first derivative of the $\mathscr{E}_{min}$ is discontinuous, for

$$\zeta_{crit} = \frac{16N_B}{34N_B - 27} \tag{3.8}$$

and $\chi = -\sqrt{7}/2$ [24, 12]. The ζ_{crit} can also be considered to coincide with ζ^* [12, 20]. The spherical minimum disappears where $\mathscr{E}$ becomes flat at $\beta = 0$, $\partial^2\mathscr{E}/\partial\beta^2|_{\beta=0} = 0$, for

$$\zeta^{**} = \frac{4N_B}{8N_B + \chi^2 - 8}. \tag{3.9}$$

The above conditions mark the region of shape/phase coexistence inside the IBM symmetry triangle between two lines. The lines meet on the $U(5)-O(6)$ leg of the triangle at $\chi = 0$ and

$$\zeta = N_B/(2N_B - 2) \tag{3.10}$$

[12], in the second order critical symmetry point. In Figure 3.4 the two lines are plotted for $N_B = 250$ and $N_B = 8$. The potential of the nuclei placed on the right side of the ζ^{**} line inside the triangle, present only the deformed minimum, the two minima coexist on the grayed area, they degenerate on the ζ_{crit}, and only the spherical minimum exists on the left of the grayed area.

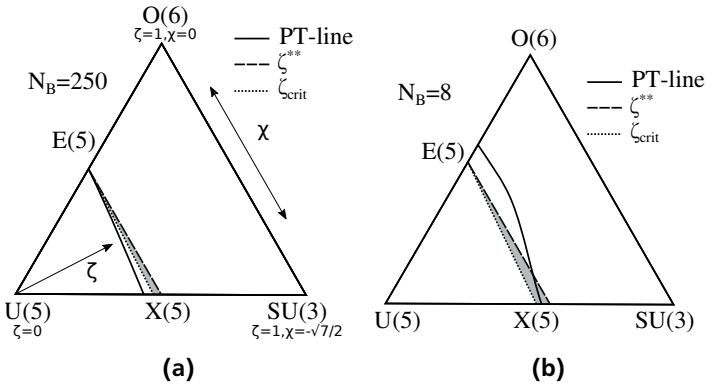

Figure 3.4.: The ζ^{**}, ζ_{crit} and PT -lines in the IBM symmetry triangle, the calculations were made, using the code IBAR [42], for (a) $N_B = 250$ and (b) $N_B = 8$.

3.3.1 Binding energy derivatives and the PT-line

As defined above the CP of the PT is where the first derivative of the $\mathscr{E}_{min}$ is discontinuous. Following the concept of the Ehrenfest classification [43] in Ref. [20] derivatives of several observables were used to determine the CPs of the QSPT in a finite-N system, over different and constant χ parameters. The most common used observable is the $R_{4/2}$ ratio [15, 20].

In this work the CP is determined by the second derivative of the binding energy (BE) [20, 22]. The slope of the binding energy is the order parameter of the many-body system. In the IBM-1 calculations for the binding energy the first-order PT is known to show a second-order PT behavior. Even in the large boson number limit.

In Figure 3.5a the binding energy over ζ for $N_B = 250$ is plotted for several χ parameters, the first and second derivatives are also plotted (Figure 3.5b and 3.5c). The calculations have been made with IBAR code which performs IBM-1 calculations [42].

For small boson numbers the binding energy does not show strongly the phase transitional behavior. See Figures 3.5d-3.5f for $N_B = 8$. The reason for this is that the small number of bosons can not present features of a system in equilibrium.

For each boson number and χ parameter the maximum of the second derivative of the binding energy defines the location of the CP as a function of ζ:

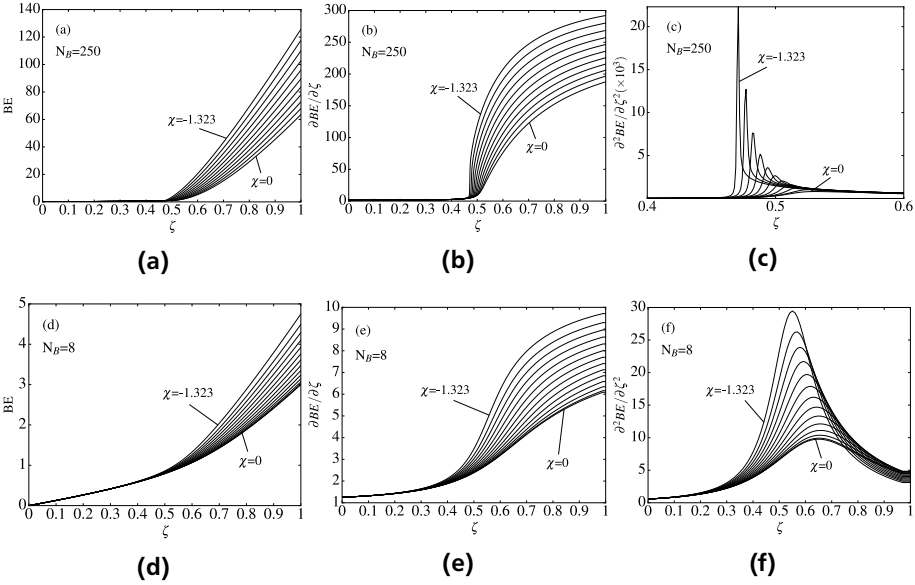

Figure 3.5.: The binding energy, the first and second derivatives for multiple χ parameters for (a-c) $N_B = 250$ and (d-f) $N_B = 8$. χ in steps of ≈0.1.

$\zeta_{QSPT}(N_B, \chi)$. These trajectories as a function of χ, for now on referred to as phase-transition lines (PT-lines), are plotted for various boson numbers of interest over the IBM symmetry triangle in Figure 3.6a.

As the N_B increases the PT-line moves towards the U(5) vertex. For large boson number (N_B=250), the trajectory approaches the shape/phase coexistence region, plotted inside the triangle by using equations (3.9), (3.8) and (3.10) (Figure 3.4a). For small boson number, $N_B = 8$, the trajectory inside the triangle is far from the shape/phase coexistence region defined by the equations (Figure 3.4b). This difference also occurs because the IBAR calculations take in account the kinetic energy of the nucleus, while equations (3.9), (3.8) and (3.10) do not.

It is shown that the phase-transitional region in the symmetry triangle depends on N_B. Nuclei with spherical shape will be placed on the left (towards U(5)) of the corresponding PT-line according on the number of their valance nucleons. Respectively, nuclei with deformed shape will be placed on the right (towards SU(3)-O(6) leg) of the corresponding PT-line according on the number of their valance nucleons. Nuclei near a QSPT region (like the $N = 90$ isotones we study in this work) will be placed near the PT-line. One

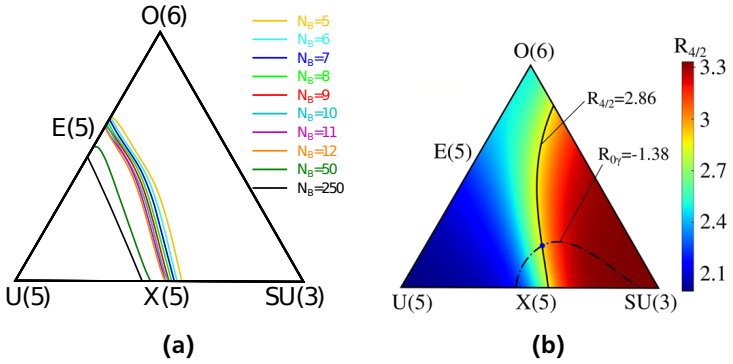

Figure 3.6.: (a) PT-lines for several boson numbers 5-12, 50 and 250. For increasing boson number the PT-line moves towards the U(5)-O(6) leg of the triangle, towards the ζ_{def} and ζ_{deg} lines. (b) The $R_{4/2}$ contours. The crossing of two contours, the $R_{4/2}$=2.86 and the $R_{0\gamma}$=1.38, is shown.

should expect that for an isotopic chain of nuclei, which evolves from spherical to deformed shapes, the PT-line will be between the "last" spherical and the "first" deformed nucleus.

In order to study the QSPT on the $N = 90$ region and specially on the cerium chain, which is mainly under study in this work, a well developed method - used for more than 20 years - of finding the position inside the IBM symmetry triangle which can describe in the best way the experimental data for nuclei was used [44, 38, 45, 24, 31, 22]. This method, of placing the isotopes in the IBM symmetry triangle [2], will be presented in the next Section.

3.4 Placement of isotopes in the IBM triangle

IBM-1 calculations for various ζ and χ parameters provide a lot of observables along the triangle. Contours of those observables run the whole IBM symmetry triangle. These contours together with the experimental data can be used for the placement of isotopes in the triangle [44, 38, 45, 24, 31]. There are a lot of experimental observables which provides acumen into the nucleus shape. The basic observables which are also experimentally most known are the low-spin yrast ener-

[2] Described like that in a schematic way.

gies, the energy of the first excited 0^+ state, $E(0_2^+)$, the energy of the quasi-2_γ state, $E(2_\gamma^+)$, the transition strengths and their ratios.

In Figures 3.6b and 3.7 the observables $R_{4/2}$, $B_{4/2}$ and the $R_{0\gamma}$ (see below) are mapped in the IBM symmetry triangle after performing IBM-1 calculations with the code IBAR for N_B=8 and a mesh of ζ and χ values. The contours where determined from parameter sets giving constant values for the observables.

For the $R_{4/2}$ contours (Figure 3.6b), the region around U(5) gives values close to the vibrational limit ($R_{4/2}$=2). By increasing ζ, the values approach the $R_{4/2}$=3.33 near the SU(3) vertex. It is clear that with alone the $R_{4/2}$ contours the placement of the isotopes is not possible cause they trace lines inside the triangle running "vertically". Similar contours, cutting the triangle "vertically", are the observables $E(O_2^+)/E(2_1^+)$, $E(2_\gamma^+)/E(2_1^+)$, which are presented in Ref. [45] and $B_{4/2}$, shown in Figure 3.7a.

In Ref. [45], the suggested observable,

$$R_{0\gamma} = \frac{E(0_2^+) - E(2_\gamma^+)}{E(2_1^+)}, \tag{3.11}$$

has a more "horizontal" trajectory (shown in Figure 3.7b). These contours are sensitive to the relative movement of the 0_2^+ and 2_γ^+ states. A nucleus with $E(0_2^+)<E(2_\gamma^+)$ is described by parameters near the bottom leg of the triangle (the U(5)-SU(3) leg), whereas a nucleus with $E(0_2^+)>E(2_\gamma^+)$ is described by parameters near the top of the triangle (near O(6)). In this work the orthogonal crossing of the two contours, the $R_{4/2}$ and $R_{0\gamma}$, was used in order to place the isotopes in the IBM symmetry triangle.

3.5 The $\gamma_{eff.}^{appr.}$ parameter

Once the nucleus is placed in the IBM symmetry triangle, and the ζ and χ coordinates are defined, the IBM-1 calculation can provide a large number of observables, like the B(E2) transition strengths. These observables can be used in order to gain information for the shape of the nucleus.

The quadrupole shape invariants [46, 47, 48], introduced by Kumar are model independent and direct observables related to the shape of a nucleus. The cubic shape parameter K_3, which derives from the q_2 and q_3 shape invariants, is related to triaxiality. In Ref. [49] it was shown that K_3 can be obtained with good accuracy, $K_3 \approx K_3^{appr.}$, from only four B(E2) values. The approximate effective value of the γ deformation ($\gamma_{eff.}^{appr.}$) in the ground state is possible to derive from the $K_3^{appr.}$. Note,

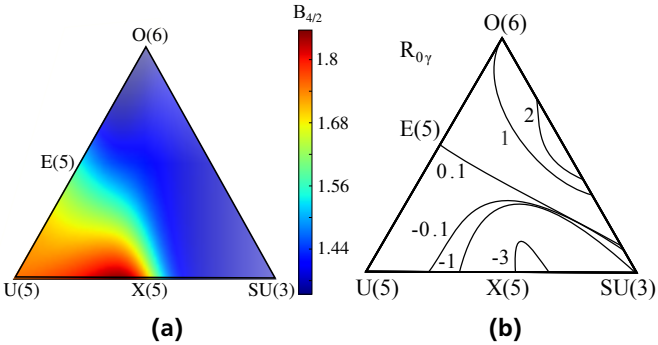

Figure 3.7.: (a) $B_{4/2}$ and (b) $R_{0\gamma}$ contours for N_B=8.

that one talks of effective γ deformation, since the nucleus does not have a rigid triaxiality.

The $K_3^{appr.}$ derives from the equation:

$$K_3^{appr.} = \sqrt{\frac{7}{10}} sign(Q(2_1^+)) \left[\sqrt{\frac{B(E2;2_1^+ \to 2_1^+)}{B(E2;2_1^+ \to 0_1^+)}} - 2 \frac{\sqrt{B(E2;2_1^+ \to 0_1^+) B(E2;2_2^+ \to 2_1^+)}}{B(E2;2_1^+ \to 0_1^+)} \right], \tag{3.12}$$

where $B(E2;2_1^+ \to 2_1^+)$ is given from the quadrupole moment $Q(2_1^+)$,

$$B(E2;2_1^+ \to 2_1^+) = \frac{35}{32\pi} Q(2_1^+)^2. \tag{3.13}$$

The $\gamma_{eff.}^{appr.}$ derives from

$$K_3^{appr.} = -\cos(3\gamma_{eff.}^{appr.}). \tag{3.14}$$

The differences between the exact $\gamma_{eff.}$ and the approximate $\gamma_{eff.}^{appr.}$ were shown not to excite the 2.5^o [49] for N_B=10 and any ζ, χ combination. One should expect the case to be the same for N_B=7-12.

The interested reader can read more about the quadrupole shape invariants and the shape parameters in the references given above. In the present work the Eqs. 3.12 and 3.14 will be used in Chapter 7 for the calculation of the $\gamma_{eff.}^{appr.}$ of nuclei near the N=88-90 QSPT.

4 Experimental techniques of lifetime measurements

In this short Chapter the reader will be introduced to fast timing techniques. The basics of fast electronic timing measurements will be described here. For more details the reader can refer to the references given in the text.

4.1 Lifetime techniques

There are several fast timing techniques which can be used for the measurement of a lifetime of a state of an exited isotope. One has to consider the time range of the lifetime to be measured and the way to populate the state of interest in order to choose the appropriate technique. Lifetimes in the micro- and nanosecond range are generally measured with delayed coincidence techniques using planar germanium detectors [50] and the lifetime is extracted with the slope method [51, 52]. For lifetimes in the pico- and femtosecond range several techniques have been developed. For lifetimes in the picosecond region the Generalized Centroid Difference Method (GCDM) was developed [53], based on the centroid shift method [54]. Both the slope method and the GCDM are based on coincidence measurements where the timing information is obtained from γ-γ delayed coincidence between fast timing detectors. Not only γ-γ delayed coincidence can be used, different coincidences can be used, for example β-γ using a β-detector [55]. The time-resolution of the individual detectors is limiting the capabilities of the experimental setup. Using the $LaBr_3$ scintillators' excellent time-resolution, lifetimes down to the picosecond range can be measured.

In Figure 4.1a a level scheme is plotted. Each one of the states is noted with its life time (τ_1,τ_2 etc.). The γ rays emitted during the de-excitation of the nucleus are also noted (γ_1,γ_2 etc.). Nuclei in excited states decay following the exponential decay equation

$$\frac{N(t)}{N_o} = e^{-\lambda \cdot t}, \tag{4.1}$$

with

$$\lambda = \frac{1}{\tau},\ \lambda = \frac{ln(2)}{t_{1/2}}, \tag{4.2}$$

where $N(t)$ the number of exited nuclei, N_o the number of the exited nuclei at $t_o = 0$, λ the decay constant, τ the mean lifetime and $t_{1/2}$ the half-life.

In order to measure the lifetime of a state (for example τ_1), using either the slope method or the GCDM, the time difference (Δt) between the γ ray (γ_2) feeding the state and the γ ray (γ_1) decaying from it has to be measured. The two γ rays have to be recorded in the fast-response detectors of the experimental setup and the signals to be fed to a time-to-amplitude converter (TAC) module. In Figure 4.1b the arrangement of a simple fast-timing setup of only two detectors is shown. The γ rays interact with the detector; the photons produced in the scintillator strike the photosensitive surface of the photomultiplier, the photocathode, causing it to emit photoelectrons; the photoelectrons are focused electrostatistically onto the first of a series of dynodes. The dynode emits more electrons than receives thus amplifying the signal; the amplified signal is collected at the anode and passes out to the measurement circuits [56].

Through the multiple dynodes the photoelectrons are multiplied and the signal, after an amplification, is large enough to be measured by the analog-to-digital converted (ADC) and then stored in order to provide the energy information. In order to measure the time of the hit, a synchronous signal to the signal on the first dynode is fed in a constant fraction discriminator (CFD) and send it to the TAC to provide the start/stop signal. The signal on the stop branch is delayed before fed in the TAC. A general and simple description of these basics modules (photomultiplier, CFD) is given in Ref. [56].

The time-difference spectrum, also called "time-spectrum", provided by the TAC contains the time distribution D(t) and is the convolution of a prompt time-distribution, P(t), and an exponential decay with decay constant λ,

$$D(t) = n\lambda \int_{-\infty}^{t} P(t' - t_o) e^{-\lambda(t-t')} dt', \tag{4.3}$$

where n is the total number of detected γ-γ events and t_o is the centroid of the P(t) (see below the definition of the "centroid"). The shape of the prompt time-distribution is shown in Figure 4.2a with red. In the same Figure a typical time-difference spectrum is shown in blue for a long (in the few-nanoseconds region) lifetime. A slope appears on one side of the spectrum corresponding to the lifetime [51, 52] due to the exponential decay law. In slope method this slope is fitted and

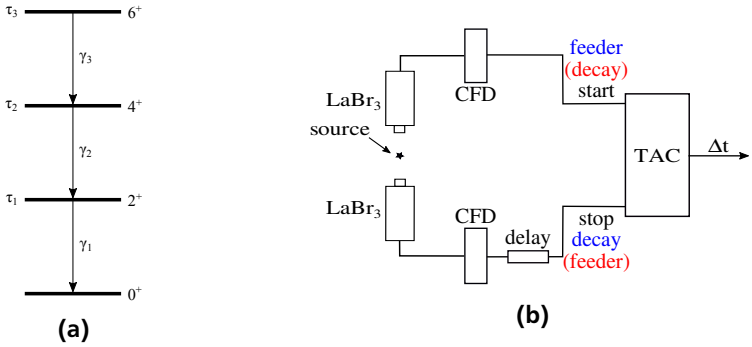

Figure 4.1.: (a) Simple level scheme. (b) A simple case of a fast-timing experimental setup of just two detectors.

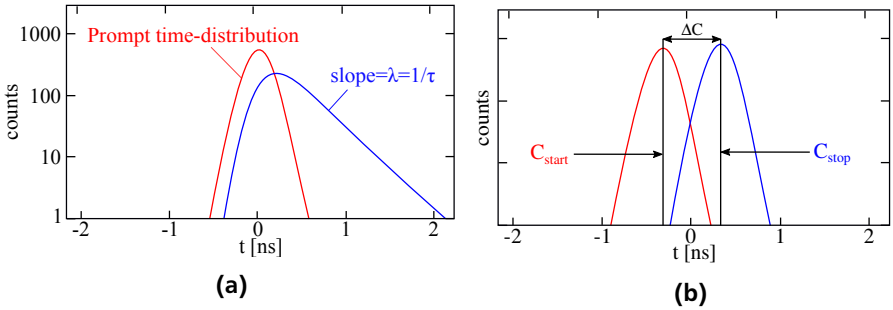

Figure 4.2.: (a) Prompt time-distribution (red curve) and typical time distribution for long (in the region on ns) lifetimes (blue curve). (b) The two time-distribution spectra. Two time spectra can be produced depending on whether the decay gamma is providing the start (with the corresponding centroid, C_{start}) or stop (with the corresponding centroid, C_{stop}) signal (whether the feeder-gamma is providing the stop or start signal respectively).

the lifetime derives. For short lifetimes this slope can not be separated from the prompt time distribution due to the time resolution of the spectrum.

Two time spectra can be produced, by the TAC, depending on whether the decay gamma is providing the start or stop signal (whether the feeder-gamma is providing the stop or start signal respectively). The two spectra are called $delayed$ and $anti-delayed$, respectively. In Figure 4.2b the two time-distribution spectra are shown. The spectra presented corresponds to a short lifetime (in the picosecond range), which is the reason for the prompt shape.

For the time distributions of the Figure 4.2b the "center of gravity" [57], centroid, can be found. In the start spectrum the centroid (C_{start}) is shifted to smaller times by one lifetime, while in the stop spectrum the centroid (C_{stop}) is shifted to larger times. This shift is used by GCDM to extract the lifetime by

$$\Delta C = C_{stop} - C_{start} = PRD + 2\tau, \tag{4.4}$$

where ΔC the centroid difference, PRD is the prompt response difference and τ the lifetime [53].

The PRD (formula 4.5) is one of the key features of the fast-timing technique. In particular, the PRD curve of the fast-timing setup, which reflect the different time that the setup requires to record gammas with different energies [58] (the so-called *"time walk"*). A typical-shaped PRD curve is given in Chapter 5 in Figure 5.7, the calibration procedure is also described.

$$PRD = PRD(E_{feeder} - E_{decay}) = PRD(E_{feeder}) - PRD(E_{decay}) \tag{4.5}$$

The full-width-half-maximum (FWHM) [56] of the prompt time-distribution does not represent directly the time-limitations of the fast-timing setup, it indicates the method that is needed to be used for each lifetime range. For lifetimes longer than the FWHM the slope method can be used. For lifetimes shorter than the FWHM the GCDM can be used.

The contributions on the FWHM of the prompt time-distribution are the following. Not all of the γ interact in the same location inside the crystal causing a constant time-spread (time-jitter). In addition to the time-jitter is included the different time-of-flight of the photons before hitting the photocathode; not all of them reflects the same times in the reflecting coating of the detector [59]. The reflecting coating is placed around the crystal to maximize the amount of the produced light hitting the photocathode. The FWHM also depends on the energy of the γ ray, and this because the different energy transfer from the radiation to the optical level of

the scintillator, the scintillation light conversion efficiency of he photocathode and the photoelectron gain variance of the photomultiplier [59, 53].

In the next chapter (Chapter 5), where the experimental setup will be described, the fast-timing properties of the setup used will be presented.

5 EXILL&FATIMA setup and calibration

In this chapter the experimental setup of the EXILL&FATIMA campaign will be presented. For more details the reader can refer to the references given in the text.

5.1 Setup

Fission data were collected in this campaign including the neutron-rich ^{148}Ce isotope of interest. The EXILL&FATIMA campaign took place at the high-flux reactor at the Institut Laue-Langevin (ILL) in Grenoble, France. Cold neutrons from the reactor were used to induce fission of ^{235}U and ^{241}Pu [60, 61]. The duration of this campaign was in total 23 days, as part of the EXILL campaign which lasted 100 days [62].

5.1.1 Reactor

The ILL research reactor has the most intense continuous neutron flux in the world. The flux in the reactor is approximately $1.5 \cdot 10^{15} n/cm^2 \cdot s$. There is a large number of neutron guides for transferring the neutrons from the reactor several meters away to the experimental areas. The most intense-one is the ballistic super mirror guide H113 [63, 64] feeding the cold-neutron beam-facility PF1B [62] (see Figure 5.1), in which the EXILL&FATIMA campaign was performed.

The neutron flux at the target position during the campaign was approximately $9 \cdot 10^7 n/cm^2 \cdot s$. The beam profile was shaped by a dedicated collimation system in a 14-mm-diameter cycle at the target position, see Figure 5.2 which was adapted from Ref. [62]. This collimation system consisted of a sequence of circular apertures. Two 1-cm thick B_4C ceramic apertures each mounted on a 5-cm thick lead aperture (for the absorption of the gammas emitted from boron) followed by three 5-mm thick ^{6}LiF ceramic apertures each mounted on a 3-cm thick borated polyethylene and 5-cm thick lead aperture. They were placed downstream the neutron beam direction in a total length of 4 m. The collimation system was place behind the neutron guide and before the target chamber.

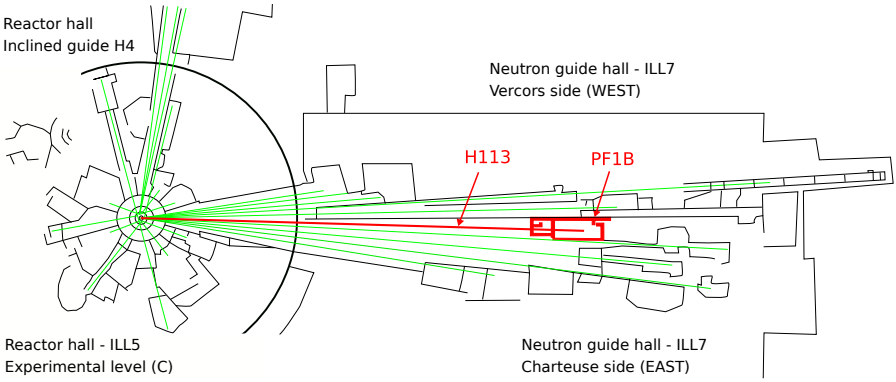

Figure 5.1.: Layout of the neutrons guides of the reactor of the ILL. The PF1B experimental zone, where the EXILL&FATIMA spectrometer was placed, and the neutron guide providing the neutrons to the setup are indicated with red. The rest of the neutron guides are shown with green.

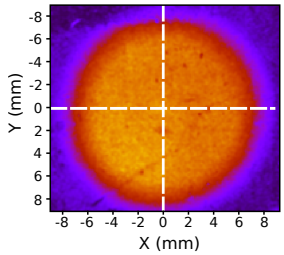

Figure 5.2.: Neutron beam profile measured in target position with film containing ^{6}Li. The orange/red color shows the profile of the beam. Adapted from Ref. [62].

For the experiment's needs the target chamber should have had low gamma absorption and low gamma scattering properties. The chamber should also not generate high gamma-background and the procedure of changing the target should be easy. In the case of the radio-toxic ^{241}Pu target the chamber should secure the area for any leak. For this, two configurations of the target chamber were used, one for the ^{235}U target and one for the ^{241}Pu target.

In the first case the target was placed in an aluminum chamber, held in a teflon bag fixed via teflon wires to a small metal frame (Figure 5.3, lower). The radio-

toxic ^{241}Pu target was first placed in an second inner target chamber (plotted with green in Figure 5.3, upper) which was sealed and vacuum pumped in ILL's alpha activity laboratory. In this case the neutron beam had to enter and exit the chamber through 200-μm thick zirconium windows. The outer chamber, the collimation system and the beam dump-pipe were filled with helium gas at a pressure of 50 mbar which was monitored during the experiment. The target chamber was followed by a 1-m long beam dump-pipe ending with a 5-mm thick ^{6}LiF ceramic.

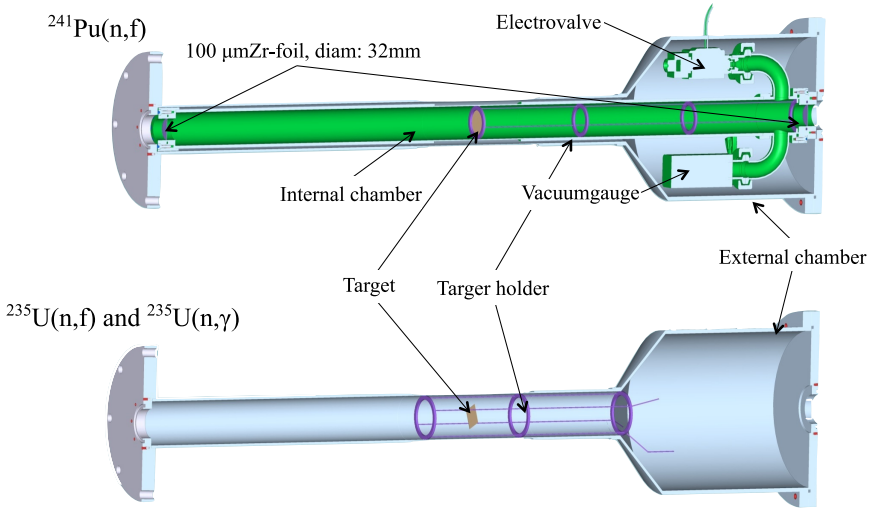

Figure 5.3.: The two configurations of the target chamber. Upper for the radiotoxic ^{241}Pu target, lower for the ^{235}U target. Adapted from Ref. [62].

The uranium fission-target, consisted of 0.8 mg $^{235}UO_2$ (0.675 mg ^{235}U) tightly sandwiched between two 25-μm-thick Be backings, was irradiated for 13 days. The plutonium target, which was as well sandwiched between two 25-μm-thick Be backings, was irradiated for 10 days. The ^{241}Pu amount was 0.3 mg [62].

A precise description of the neutron beam profile and flux, the collimation system, the targets' chambers and the targets can be found in Ref. [62].

All fission fragments were stopped within $\sim$ 1 ps by the thick backing of the targets. More than 100 different isotopes were produced from the fission, including isotopes in the vicinity of N=90.

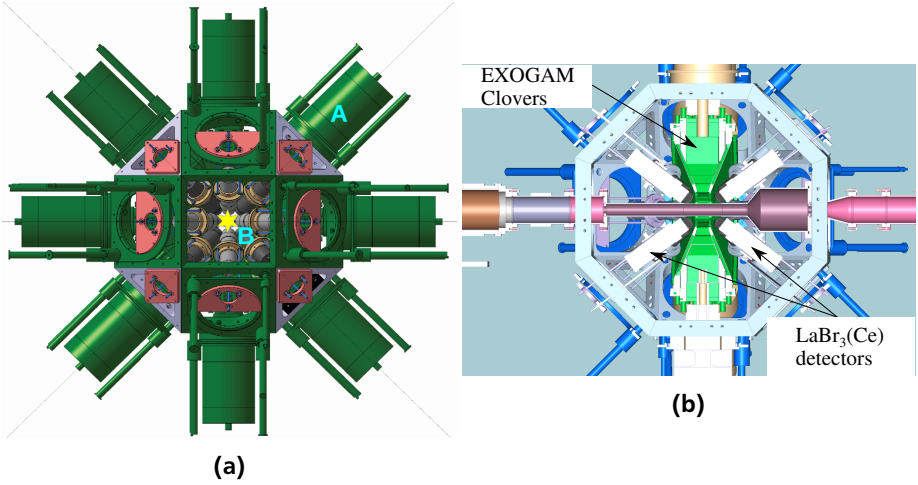

Figure 5.4.: The EXILL&FATIMA spectrometer. In (a) the marker A shows an EXOGAM Clover detector, B shows a $LaBr_3$ detector and the star shows the position of the target. (a) Taken from Ref. [71] and (b) adapted from Ref. [62].

5.1.2 Spectrometer

In order to measure the lifetimes of interest the nucleus was selected among all deferent fission fragments and the feeding and decaying gamma-rays of the state of interest provided the time information. The prompt γ-rays from the fission fragments were detected using a hybrid array of High-Purity Germanium (Ge) and Ce-doped Lanthanum bromide ($LaBr_3$) detectors, the EXILL&FATIMA spectrometer [65, 66], see Figure 5.4. The excellent energy resolution of the Ge detectors was used in order to isolate from the data the nucleus of interest by gating on a gamma-ray of its cascade. On the other hand, the excellent time performance of the $LaBr_3$ detectors allowed the measurement of lifetimes in the order of some ps. In Figure 5.5 the energy efficiency of the two arrays used are presented. The supreme energy resolution of the Ge detectors can be seen.

The EXILL array was composed of 8 BGO-shielded EXOGAM Clover detectors [62, 67, 68, 69], each one consisting of 4 Ge crystals. The target-to-detector distance was 14.5 cm. The array was placed at 90° relative to the beam direction, in a ring arrangement. This allowed precise energy gates to be set on a γ ray of the cascade of interest and, hence, the nuclei of interest. The BGO (Bismuth

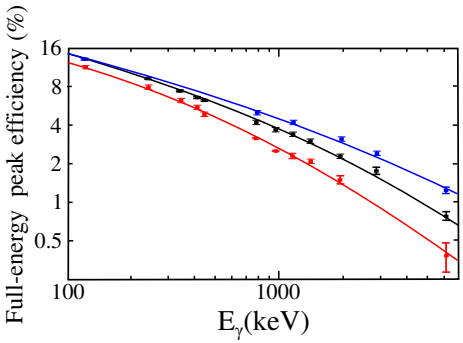

Figure 5.5.: The full-energy efficiency curves for the FATIMA array (red), the EXILL array without (black) and with (blue) the add-back option.

germanate)-shields were used in order to suppress the "Compton background" on the Ge detectors.

In energy spectra the term "Compton background" refer to the signals originating from γ rays which did not deposit their whole energy in the detector [56]. After Compton scattering the photon can escape the detector. In this case the hit will be registered as a hit of a lower energy γ ray, contributing to a continuous background. If the rest of the energy is deposited in a Ge detector belonging to the same clover the reconstruction of the full-energy of the γ ray is possible. It is also possible the escaping photon, after a Compton interaction, to be detected in the BGO shield. By rejecting all hits in coincidence with the BGO the Compton background can be suppressed. Of course the environmental background can also be detected from the BGO shield. Therefore, it is needed to discriminate the hits originating from the environmental background from the escaped photons. An individual energy threshold per BGO shield can be set below which all signals from the clover detector (shielded by the specific BGO) in coincidence are rejected.

FATIMA consisted of 16 (5% Ce-doped) $LaBr_3$ detectors arranged in two rings, at 40° and 140° relative to the beam direction. Since the FATIMA efficiency was crucial for the experiment, the detectors were placed as close as possible to the target, at 8.5 cm, almost touching each other. The $LaBr_3$ crystals differed only slightly in their length, 8 of them were 1.5 in. longe, while the other 8 were 2 in. long.

To achieve a high timing performance the crystals were connected with the Hamamatsu R9779 photomultiplier tube (PMT) for its excellent energy and timing performance. The time information was provided by the $LaBr_3$ detectors through

an analogue electronic "fast-timing" circuit (Figure 5.6). The time signal from the first dynode of the PMT was fed to a constant fraction discriminator (CFD), from there to a system of multiple multi-channel logic fan-in/fan-out (FAN) modules connected with N-1 time-to-amplitude converters (TAC), where N=16 is the number of the $LaBr_3$ detectors used. As it is illustrated in Figure 5.6, $TAC_{i,j}$ could be started only by detector i and stopped by detector $j \ni [i+1, N]$. With this principle it was possible to know which of the gamma-rays providing the time signals to the TAC was providing the start and which the stop signal. This is very essential in the fast timing techniques where the lifetime of the state derives from the delayed and the anti-delayed time spectra, see chapter 4.

A complete description of the analogue electronic "fast-timing" circuit can be found in Ref. [70]. A full description of the EXILL&FATIMA spectrometer can be found in Ref. [65].

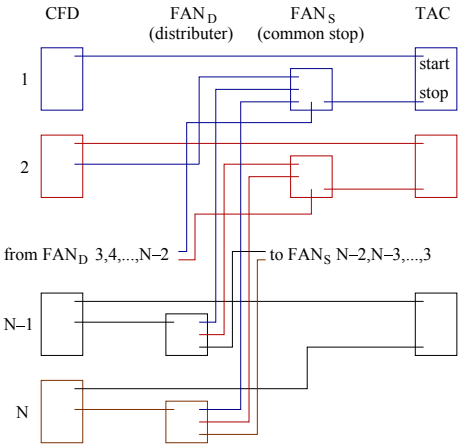

Figure 5.6.: The analogue electronic "fast-timing" circuit. Adapted from Ref. [70].

5.2 Calibration of the spectrometer

To measure short lifetimes, shorter than the time-resolution of the $LaBr_3$ detectors' used, the calibration of the timing response of the setup it is of great importance. As explained in chapter 4, the PRD represents the linearly combined $\gamma-\gamma$ time-walk characteristics of two detector timing systems. Any $\gamma-\gamma$ cascade of known lifetimes can be used to calibrate the PRD curve ($PRD(E_\gamma)$). For the FATIMA the experimental (mean) $\overline{PRD}$ was obtained after the superposition of N(N-1) aligned

$TAC_{i,j}$ time-spectra from all $LaBr_3$ detector combinations. All time-spectra were aligned using constant-shift values ($shift_{i,j}$). Those were derived by aligning the stop signal from a specific $\gamma-\gamma$ cascade to all $LaBr_3$ i,j combinations. A ^{152}Eu γ-ray source provided more than 20 cascades for the $\overline{PRD}$ calibration of the energy region of 40 keV<E_γ<1300 keV. Additionally the decay of ^{49}Ti, produced from the neutron-capture reaction ^{48}Ti$(n_{th},\gamma)^{49}$Ti, provided data for the energy region 137 keV<E_γ<6800 keV. The europium source was placed in the center of the array for both the energy and $\overline{PRD}$ curve calibrations. The titanium target was placed in the target position and irradiated with cold neutrons from the reactor. The reference energy (E_{ref}) (see Ref. [58]) of the $\overline{PRD}$ curve was chosen to be the 344 keV γ-ray from the $2_1^+ \rightarrow 0_{gs}^+$ transition of ^{152}Gd. The $\overline{PRD}$ of the FATIMA array is shown in Figure 5.7 together with the fitted curve using the equation

$$\overline{PRD}(E_\gamma) = \frac{a}{\sqrt{E_\gamma + b}} + cE_\gamma + dE_\gamma^2 + e. \tag{5.1}$$

As can be seen the curve meets zero on the E_{ref}=344 keV. The $\overline{PRD}$ for all energy combinations can be calculated with the equation

$$\overline{PRD}(E_1 - E_2) = \overline{PRD}(E_1) - \overline{PRD}(E_2), \tag{5.2}$$

where E_1 and E_2 can be E_{feeder} and E_{decay} the energy of the feeding and the decaying γ-rays of the state of interest, respectively.

Another important feature of the fast timing setup is the time resolution of the setup, e.g. the FWHM of the time response of the detectors. This can be seen in the time-difference spectra from prompt γ rays. The FWHM is dependent on the γ-ray energy of both the feeding and the decaying transitions, the ones which are providing the start and stop signals to the TAC. In Ref. [65] the FWHM for the the energies combination 40 keV-444 keV is reported to be $FWHM_{40-444}$=820 (8) ps. Additionally it is reported that $FWHM_{3026-3733}$=272 (3) ps. Figure 5.8 was adapted from Ref. [65] and presents the FHWM of the time spectra over the smaller energy of the two γ rays of the $\gamma-\gamma$ cascade. As it was explained in chapter 4, for lifetimes longer than the time resolution of the setup the slope method is used and for lifetimes shorter than the time resolution of the setup the GCDM is used. A detailed description of the $\overline{PRD}$ calibration procedure is given in Refs. [72, 71].

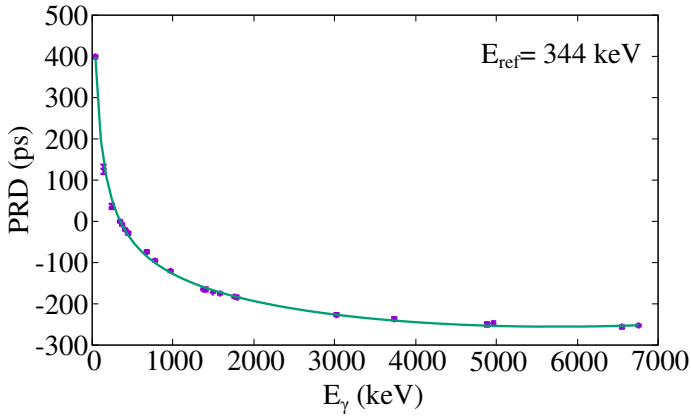

Figure 5.7.: $\overline{PRD}$ curve.

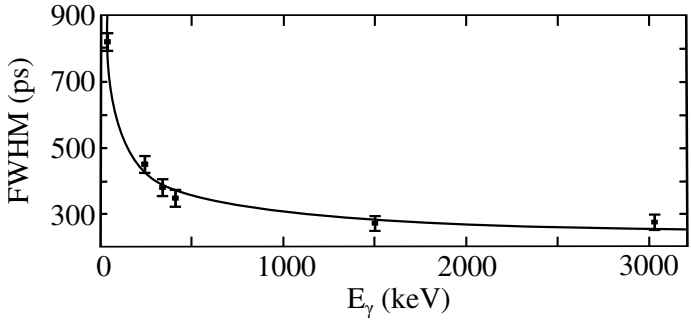

Figure 5.8.: Time resolution of the FATIMA array. The FWHM is dependent on the γ-ray energy of both γ-rays providing the start and stop signals. The energy of the data points corresponds to the smaller energy of the two γ rays. Adapted from Ref. [65].

6 Data analysis

In this Chapter the analysis of the experimental data will be presented. The reader will not be introduced to the fundamental principals of γ-spectroscopy and the coincidence method since this is not the purpose of this Doctoral thesis. The reader can refer to Ref. [56] and to the references given in Chapter 4.

6.1 SOCOv2 Code

The huge number of isotopes produced by fission enforced the usage of multiple coincidences to choose the isotopes of interest. Ge-$LaBr_3$-$LaBr_3$ coincidences were used to select the cascade of interest and derive the time information. Because of the low energy resolution of the $LaBr_3$ detectors, the purity of the $LaBr_3$ energy gate-conditions had to be verified. For this Ge-Ge, Ge-Ge-Ge and Ge-$LaBr_3$-Ge coincidences were obtained. For this multi-gate analysis a C++ software package, the code "SOCOv2" [73], has been created by the Institute of Nuclear Physics of Cologne for the analysis of the trigger-less list-mode data. In the rest of this Chapter the "gate" or "gate-condition" will refer to conditions applied to the data in order to select specific signals in coincidence.

Here the steps of the data management using the code SOCOv2 will be presented. A precise description can be found in Ref. [73] and in the manual of the code. The trigger-less data stream collected from the experiment is pre-sorted into events. The event building procedure allows the selection of many requirements. One can choose the number of hits considered as coincidence, the type of detectors recording the hits (only Ge, only $LaBr_3$ or any mixture, like Ge-$LaBr_3$-$LaBr_3$ coincidences), the coincidence time-window size, the usage of "add-back" on the Ge hits and using the hits on the BGO detectors as anti-coincidence. An example of the command used for the event-building and the files requiring and specifying all above is presented in Appendix B.

All possible options provided by the code allow to check different parameters for the analysis of the data and find the appropriate ones depending on the experiment. For the EXILL&FATIMA data and especially for the selection of ^{148}Ce, a time-window of 200 ns (typical time resolution of the Ge detectors) was selected in order to not lose any statistic on the Ge energy gate-condition set on the data

to select the cascade of interest. No background-correction analysis on this time-window selection was performed. To measure lifetimes in the order of some ns or ps the feeder/populating and decaying γ-rays had to be recored in the fast-responding $LaBr_3$ detectors, additionally the cascade of interest had to be selected by setting a energy gate-condition on the high energy-resolution Ge detectors. For this in the event-building the Ge-$LaBr_3$-$LaBr_3$ coincidences were selected. Because of the low energy-resolution of the $LaBr_3$ detectors the set energy gate-conditions had to verified to be free of any contaminations, like energy peaks near the desired ones (feeder and decaying γ-rays of the state of interest). The same gate-conditions had to be checked for the Ge detectors. For this the data were additionally event-build choosing Ge-Ge-$LaBr_3$ coincidences.

To select the energy gate-conditions which will allow the lifetime measurement, gated coincidence energy spectra were generated using the code SOCOv2. During the generation of the gated coincidence energy spectra using the code SOCOv2 there are a lot of options which can be enabled. The reconstruction of the full energy of a γ ray escaping the crystal after a Compton interaction [56] is possible, when the escaping γ ray is detected by a Ge detector in the same clover. In code SOCOv2 this is enabled with the so-called "add-back" option. In this way the Compton background [56] is reduced and the volume of the full energy peak increases. By enabling the "BGO-shield" option the coincidence event is being rejected, if the escaping photon, after a Compton interaction, has been detected in the BGO shield. In this way the Compton background is suppressed.

The "Compton background" of the $LaBr_3$ detectors is suppressed by the "exclude" option. With this option neighboring $LaBr_3$ detectors are excluded during the generation of the gated coincidence energy spectra. In order to get the $LaBr_3$-$LaBr_3$ coincidences the constant-shift values ($shift_{i,j}$) is used for the alignment of the TACs (see Chapter 5.2 and Ref. [73]). Examples of the command used for the generation of the gated coincidence energy spectra and the files needed are given in Appendix B.

After specifying the proper energy gate-conditions and verifying that they do not include contributions which will effect the lifetime measurement, with the help of the gated coincidence energy spectra, the fast-timing matrices can be build. This matrices includes the time-difference spectra between $LaBr_3$-$LaBr_3$ hits. Again the number and the type of detectors used can be chosen. For the EXILL&FATIMA data and specially for the selection of ^{148}Ce, one energy gate-condition was selected in the Ge detectors in order to select the isotope of interest. As in the case of the generation of the gated coincidence energy spectra, the "add-back" option, the BGO's threshold option, the exclusion neighboring $LaBr_3$ detectors coincidences option and applying the $shift_{i,j}$ values for the alignment of the TACs option could

be used. In Appendix B are given examples of the command used for the generation of the fast-timing matrices and the files needed.

The code, in order to calculate the fast-timing matrices, requires the energy gate-condition for one of the two $LaBr_3$ hits. By using the assumption that a TAC_i can only be started by $LaBr_i$ and stopped by $LaBr_j$, with j>i, the code can distinguish whether the specific hit provided the start or stop signal to the TAC and increments the right matrix respectively. The start-matrix in Figure 6.1 is created by the condition that the specified, through the energy gate-condition, γ ray is the one providing the start signal to the TAC fired. The energy of the γ ray which provides the stop signal is given by one of the matrix's dimensions. The other two dimensions are the time-difference, given by the TAC fired, and the counts. Respectively, in the stop-matrix the specified, through the energy gate-condition, γ ray is the one providing the stop signal.

In Figure 6.1c the energy projection of the stop-matrix (Figure 6.1b) is shown. By setting an energy gate-condition the resulting time-difference spectrum can be generated (Figure 6.1d). In the case that the energy gated-condition to create the fast-timing matrix is the energy of the γ ray feeding the state of interest and the set energy gate-condition on the stop(start)-matrix is the energy of the decay γ ray of the state of interest, the time-difference spectrum is the (anti-)delayed time-difference spectrum, defined in Chapter 4.

As explained in Chapter 4, if the lifetime of the state is in the order of some ns then a slope appears in the time-spectrum corresponding to the lifetime (slope method). If the lifetime is in the ps range, it can be measured using the centroids of the two time-difference spectra (GCDM). In the case of the lifetime of the 2_1^+ state of ^{148}Ce the slope method was used. In the case of the ps range lifetime of the 4_1^+ state of ^{148}Ce the GCDM was used. The analysis of the data from the fission of ^{235}U (from which the ^{148}Ce was highly produced) is presented below (sections 6.2 and 6.3).

6.2 2_1^+ lifetime using the slope method

To derive the lifetime of the 2_1^+ state of ^{148}Ce, in the order of ns, the slope method [51, 52] was used. The procedure described above was followed. The two γ-rays providing the time information were originating from the 4_1^+ state decaying to the 2_1^+ state with an energy of 295.07 (9) keV [10] (for simplicity in this section refereed to as the feeding γ-ray) and the 2_1^+ state decaying on the ground state with an energy of 158.468 (5) keV [10] (for simplicity in this section refereed to as the decaying γ-ray). The level scheme of ^{148}Ce is shown in Figure 6.2.

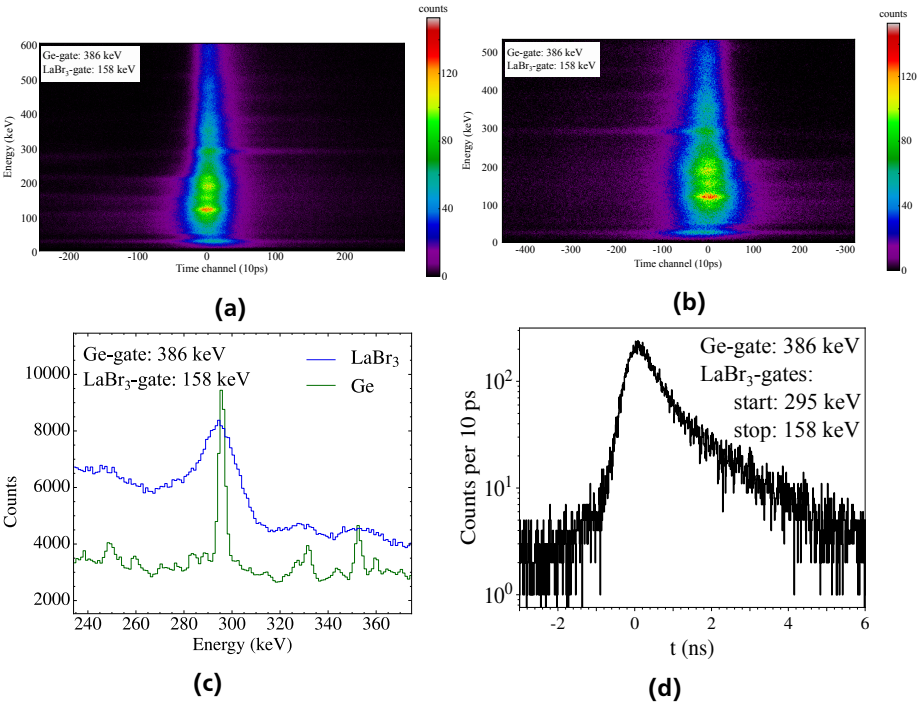

Figure 6.1.: The fast-timing matrices gated on the 386 keV in the Ge detectors and on 158 keV in $LaBr_3$ detectors. (a) Start- and (b) stop-matrix. (c) Energy projection of the stop-matrix. The blue spectrum corresponds to the $LaBr_3$ spectrum, while the green one corresponds to the Ge spectrum obtained by applying the same gate conditions in the Ge-$LaBr_3$-Ge sorted data in order to verify the purity of the gates. (d) Time-difference spectrum resulting from the cut on the 295 keV peak (energy channels 290 - 300 keV). The start signal to the TAC was provided by the 295 keV γ-ray and the stop by the 158 keV γ-ray.

In order to pre-select the isotope of interest an energy gate , S1, was set on the $6_1^+ \rightarrow 4_1^+$ transition in the EXILL Ge detectors. The widths of the gate - the ranges of the gate-conditions - for all gate conditions applied are shown in Table 6.1. The resulting Ge and $LaBr_3$ spectra are shown in Figure 6.3a. Both peaks (at 158 keV and 295 keV) corresponding to the feeding and decaying γ-rays, are

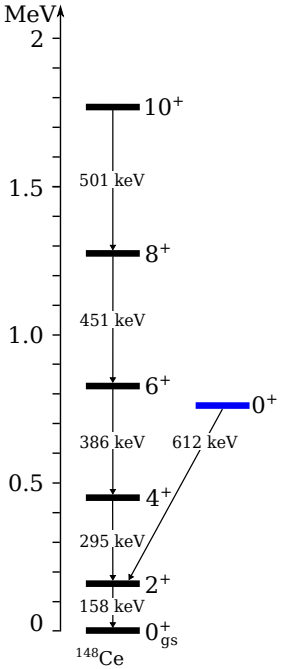

Figure 6.2.: Partial level scheme of ^{148}Ce [10].

clearly seen in both the Ge and the $LaBr_3$ spectra. Both of the peaks are clean of any contamination.

The start and stop fast-timing matrices (Figures 6.1a and 6.1b) were produced by applying an additional energy gate-condition, A (shown in Figure 6.3a), on the $2_1^+ \rightarrow 0_1^+$ transition.

To obtain the time-difference spectra between the $4_1^+ \rightarrow 2_1^+$ and $2_1^+ \rightarrow 0_1^+$ γ-rays, a second energy gate-condition, B (shown in Figure 6.3a), was set on the respective peaks in the FATIMA $LaBr_3$ detectors. The gate-condition in the $LaBr_3$ detectors were verified to be clean of any other contaminations by applying the same energy gates in the Ge-$LaBr_3$-Ge sorted data. In Figure 6.1c the purity of the gate-condition B in the $LaBr_3$ detectors can be seen in the Ge spectrum obtained for same gate-conditions applied in the Ge-$LaBr_3$-Ge sorted data.

The two time-difference spectra are shown in Figure 6.4. The black curve (start) corresponds to the condition that the 295 keV γ-ray of the $4_1^+ \rightarrow 2_1^+$ transition was recorded as start signal to the TAC (delayed time spectrum). The red one

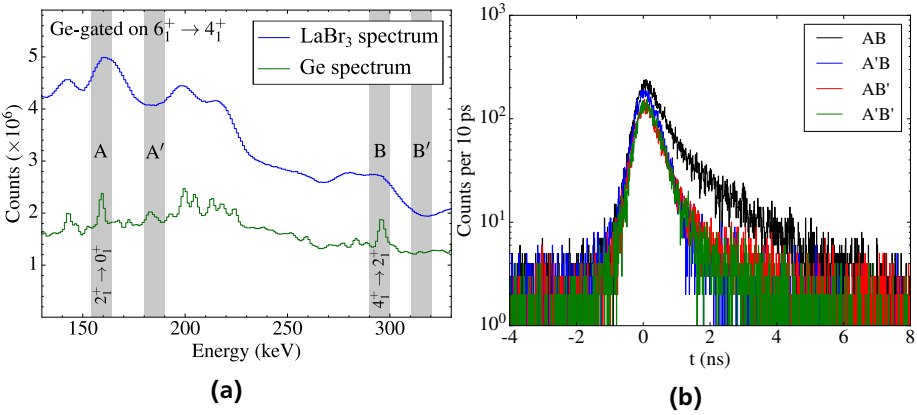

Figure 6.3.: (a) Energy spectra from the EXILL&FATIMA array gated on the $6_1^+ \rightarrow 4_1^+$ transition of ^{148}Ce in EXILL, Ge (green) and LaBr$_3$ (blue). The gates in FATIMA detectors are marked with light gray. (b) The individual delayed time spectra for the subtraction of the time background.

(stop) is the anti-delayed spectrum, which corresponds to the condition that the 295 keV γ-ray of the $4_1^+ \rightarrow 2_1^+$ transition was recorded as the stop signal to the TAC. Both spectra show a slope on one of their sides (in the larger times for the delayed spectrum and in the smaller times for the anti-delayed spectrum).

Using the slope method the lifetime of the 2_1^+ state of ^{148}Ce was measured from both spectra. The error-weighted average value from the two spectra for the lifetime is $\tau_{2_1^+} = 1.466\ (50)$ ns. The individual values from each spectrum are 1.491 (67) ns from the delayed spectrum and 1.433 (75) ns from the anti-delayed spectrum. The fit regions of the slope containing the lifetime information were selected by fitting the slope over small time intervals of $\sim$ 1 ns and defining the region where the slope was stable.

6.2.1 Background-subtracted time spectra

The reader should notice that there wasn't any kind of manipulation of the data up to this point. Any contributions in the time-spectrum, in the slope region, was assumed to be not of importance or affecting the slope in the spectra. In reality, as it can be seen in Figures 6.1c and 6.3a the energy spectra contain the typical Compton contribution [56].

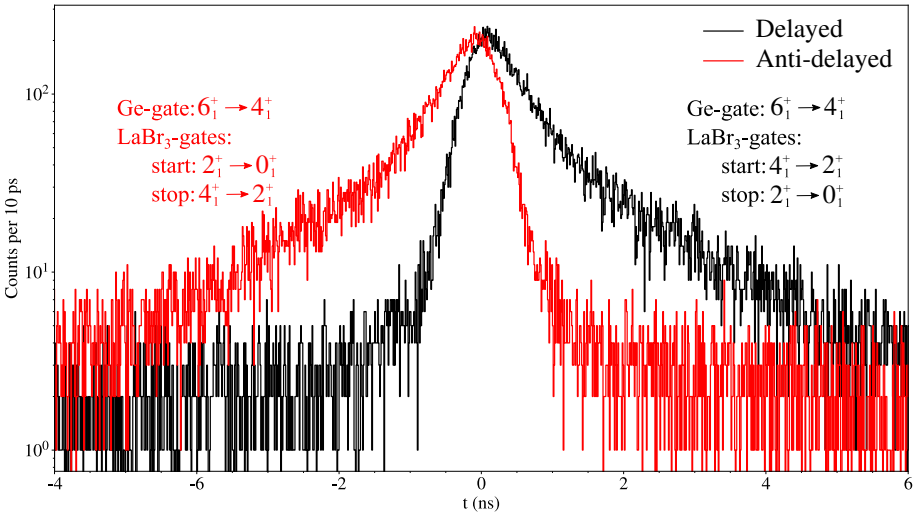

Figure 6.4.: The two un-manipulated time-difference spectra are shown, delayed and anti-delayed, for the life-time of the 2_1^+ state of ^{148}Ce. The energy gate-conditions are given for each spectrum.

The energy gate-conditions performed include γ-rays from the background, e.g. Compton-events from higher-lying transitions. If the state, of which the Compton γ-rays originates from, has a long lifetime (in the ns region), then this event will contribute to the slope region of the time spectrum. If the lifetime is short (in the ps region) then the event will contribute to the prompt region of the time spectrum.

In order to subtract these contributions, the method from Ref. [52] was used and additional energy gate-conditions (background gates), A′ and B′, were defined (see Figure 6.3a) in the background-region of the peaks of the $LaBr_3$ spectra and the time-difference spectra generated following the coincidence logic AB-AB′-A′B+A′B′. The individuals spectra are shown in Figure 6.3b.

In figure 6.5 the resulting background-subtracted time-difference spectra are shown, delayed and anti-delayed. The lifetime was measured to be $\tau^{sub}_{2_1^+} = 1.430$ (83) ns [1]. The error includes the statistical error and the systematic error. The systematic error was checked by changing the position of the background gates, to A″ and B″ (see Table 6.1), and the fit region. The measured lifetime is in agreement

[1] The "*sub*" notation stands for the *background-subtracted time spectra* used.

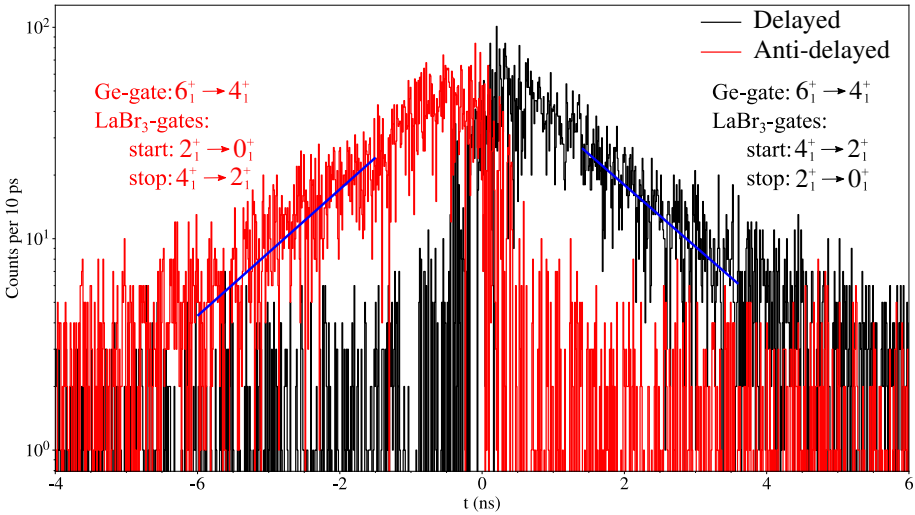

Figure 6.5.: The background-subtracted time-difference spectra, delayed and anti-delayed, for the life-time of the 2_1^+ state of ^{148}Ce are shown. The gate-conditions performed are also given. The fitted slopes are shown in blue. The gated cascade is shown in Figure 6.2.

with the literature value of 1.457 (87) ns [74], giving confidence to the method of handling the background. The lifetime is also in agreement (within the error-bars) with the one measured by the un-manipulated data. This shows that any contribution to the time spectrum was not placed on the region of the slope. For comparison, the two delayed time spectra together with the fit region of the slope are shown in Figure 6.6.

6.3 4_1^+ lifetime using the Generalized Centroid Difference method

For the 4_1^+ state the GCDM was used to determine the lifetime (in the picosecond range). The energy gate-condition, S2, in the EXILL Ge detectors was set to the $2_1^+ \rightarrow 0_1^+$ transition of ^{148}Ce at 158.468 (5) keV [10] for the pre-selection of the isotope of interest. The two γ-rays providing the time information were the one originating from the 6_1^+ state decaying to the 4_1^+ state with the energy 386.15 (20) keV [10] (for simplicity in this section refereed to as feeding γ-ray) and the one originating from the 4_1^+ state decaying to the 2_1^+ state with the energy 295.07 (9) keV [10] (for simplicity in this section refereed to as decaying γ-ray). The widths

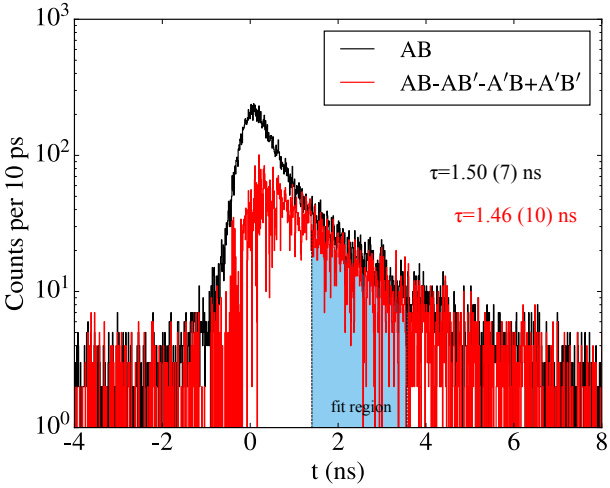

Figure 6.6.: Comparison of the un-manipulated (black) and background-corrected (red) delayed time spectra for the life-time of the 2_1^+ state of ^{148}Ce. The region of fit is shown and the lifetimes measured are given.

Table 6.1.: Width of the gate-conditions for all gate-conditions applied.

gate	transition	width of gate-condition (keV)
S1	$6_1^+ \rightarrow 4_1^+$	383-388
A	$2_1^+ \rightarrow 0_1^+$	153-163
A′	background	180-190
A″	background	185-195
B	$4_1^+ \rightarrow 2_1^+$	290-300
B′	background	311-321
B″	background	335-345
S2	$2_1^+ \rightarrow 0_1^+$	155-160
A_1	$4_1^+ \rightarrow 2_1^+$	290-300
A_1'	background	318-328
A_1''	background	323-333
B_1	$6_1^+ \rightarrow 4_1^+$	381-391
B_1'	background	409-419
B_1''	background	414-424

of the gate-conditions - the ranges of the gate-conditions - for all gate-conditions applied are shown in Table 6.1.

The gate-conditions applied to the $LaBr_3$ detectors, for the time-information, were verified to be clean of any contribution by producing the Ge spectrum by applying the same gate conditions on the Ge-$LaBr_3$-Ge sorted data. The energy spectra were produced by applying the S2 gate-condition on the Ge detectors and the A_1 gate-condition at the decaying γ-ray peak on the $LaBr_3$ detectors. The two Ge spectra produced are shown in Figure 6.7. The Figure 6.7a shows that the feeding γ-ray peak (at 386.15 (20) keV) on the $LaBr_3$ spectrum is clean of any contributions. Respectively, by exchanging the feeding and the decaying γ-rays on the gate-conditions presented before, the purity of the decaying γ-ray peak on the $LaBr_3$ spectrum was verified, see Figure 6.7b. The gate-condition at the decaying γ-ray peak is noted here as B_1.

The start and stop fast-timing matrices (Figures 6.8a and 6.8b) were produced by applying, additionally to the S2 gate-condition, the energy gate-condition, A_1. To obtain the time-difference spectra feeding and decaying γ-rays, the second energy gate-condition, B_1, was set in the FATIMA $LaBr_3$ detectors.

The two time-difference spectra are shown in Figure 6.9. The black curve (A_1B_1 delayed, the notation correspond to the gete-conditions applied) corresponds to the condition that the 295 keV γ-ray of the $4_1^+ \rightarrow 2_1^+$ transition was recorded in as stop signal to the TAC, delayed time spectrum. The blue one (A_1B_1 anti-delayed) is the anti-delayed spectrum, which corresponds to the condition that the 295 keV γ-ray of the $4_1^+ \rightarrow 2_1^+$ transition was recorded in as start signal to the TAC. Both spectra show the typical prompt shape (see Chapter 4).

The delayed spectrum is shifted to larger times, while the anti-delayed to smaller times. The centroid shift measured to be $\Delta C=66$ (3) ps. One can notice in Figures 6.7a and 6.7b the Compton-background [56] under both full-energy peaks of the feeding and the decaying γ-rays. This background contribute in the time spectrum. In order to remove this contribution two techniques were used and compared.

6.3.1 Interpolation of the time-background

As it can be seen in Figure 6.10 the full-energy peak of the feeding γ-ray is located on the Compton-edge [56] of the Compton-background. The exact location is not known (in the start, middle or end of the Compton-edge). All these three background shapes are possible and any shapes between them. The contribution of the background in the time spectrum on the location of the full-energy peak can be found by the interpolation of the timing of the Compton background [65]. The

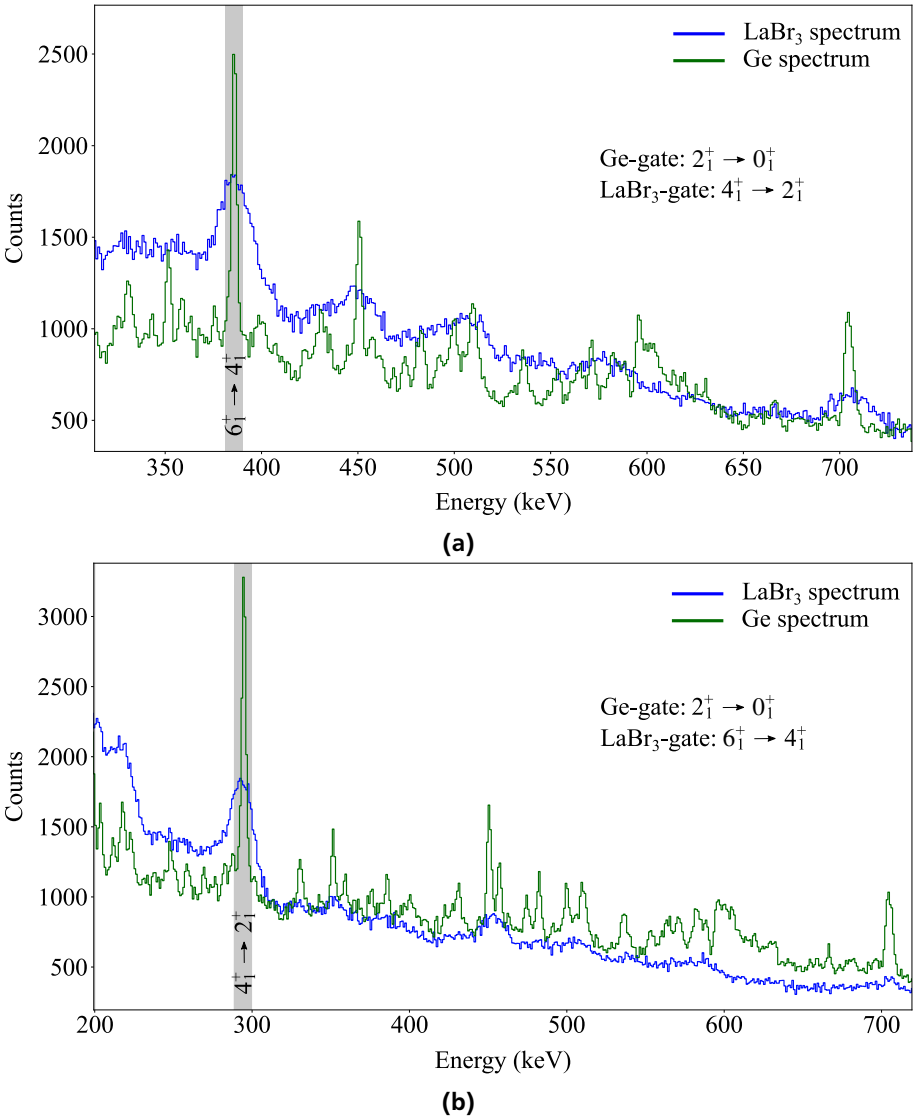

Figure 6.7.: Ge and $LaBr_3$ spectra for the verification of the purity of the energy gate conditions set on the $LaBr_3$ detectors for the life-time of the 4_1^+ state of ^{148}Ce. (a) For the $6_1^+ \rightarrow 4_1^+$ transition γ-ray at 386.15 (20) keV peak and (b) for the $4_1^+ \rightarrow 2_1^+$ transition γ-ray at 295.07 (9) keV. The energy gate conditions applied are also shown.

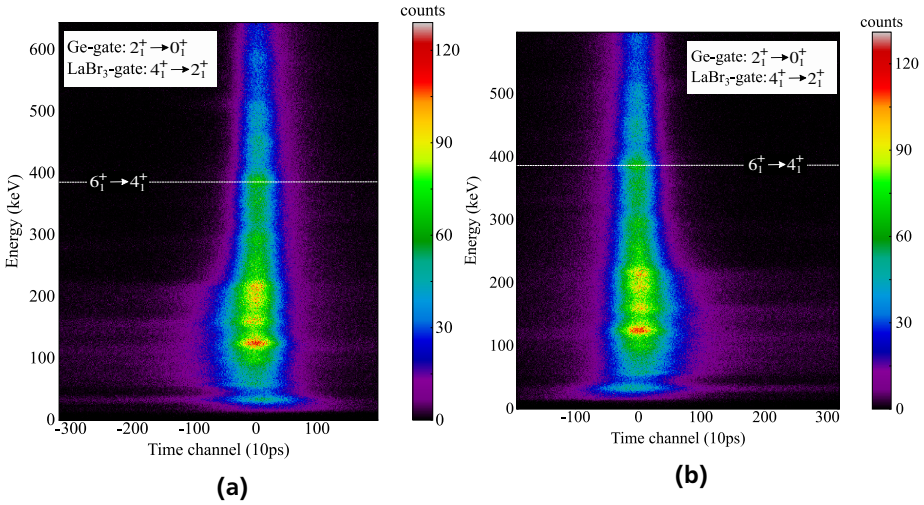

Figure 6.8.: The fast-timing matrices gated on the 158 keV ($2_1^+ \rightarrow 0_1^+$ transition) in the Ge and on 295 keV ($4_1^+ \rightarrow 2_1^+$ transition) in the $LaBr_3$ detectors for the life-time of the 4_1^+ state of ^{148}Ce. (a) Start- and (b) stop-matrix.

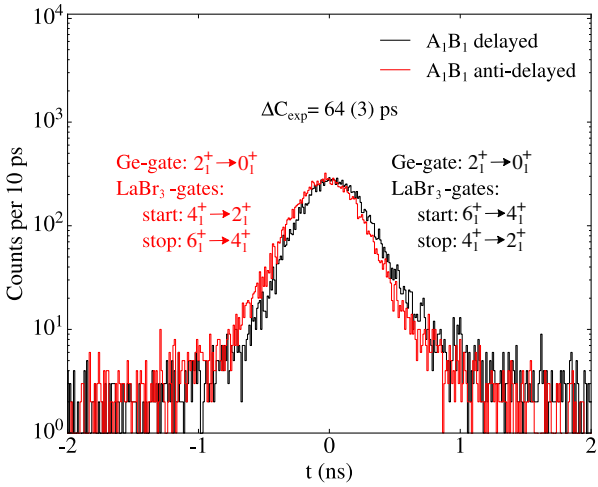

Figure 6.9.: The two time-difference spectra for the lifetime of the 4_1^+ state of ^{148}Ce. The energy gate-conditions are given for each spectrum.

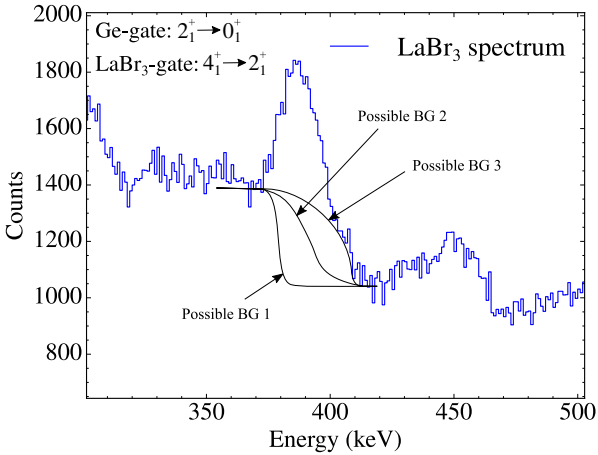

Figure 6.10.: In the figure three possible cases of the background under the full-energy peak of the 386 keV γ-ray of the $6_1^+ \rightarrow 4_1^+$ transition are shown. The real background is not known.

same treatment was followed in all publications of the EXILL&FATIMA campaign for lifetimes in the ps region [75, 71, 76, 77, 78].

With this time background correction the ΔC in equation (4.4) has to be corrected by a correction factor (t_{cor}). It will be

$$\Delta C = \Delta C_{exp} + t_{cor} = PRD + 2\tau, \tag{6.1}$$

where

$$t_{cor} = \frac{t_{cor}(E_{feeder}) + t_{cor}(E_{decay})}{2}, \tag{6.2}$$

with

$$t_{cor}(E_{f/d}) = \frac{\Delta C_{exp} - \Delta C_{BG}^{f/d}}{P/B(E_{f/d})}, \tag{6.3}$$

where $\Delta C^{f/d})_{BG}$ is the interpolated background timing in the location of the full-energy peak (feeder or decay) and P/B is the peak-to-background ratio [56] of the full-energy peak (feeder or decay). The t_{cor} contains the correction of the time background under both the feeding and the decaying γ-rays.

In Figure 6.11a the centroid-difference spectrum is plotted together with the Ge and $LaBr_3$ spectra. The centroid-difference spectrum is the spectrum of the centroid differences of the time spectra (start and stop) produced by applying the Ge gate-condition on the decay of the $2_1^+ \rightarrow 0_1^+$ transition of ^{148}Ce at 158.468 (5) keV, applying one $LaBr_3$ energy gate-condition on the decaying γ-ray and altering the second $LaBr_3$ energy gate-condition for the whole spectrum. The start spectrum was the one produced by the decaying γ-ray providing the start signal to the TAC and respectively the stop spectrum was produced by the decaying γ-ray providing the stop signal.

One can see that the centroid-difference values oscillates. The ΔC_{BG} in the location of the full-energy peak of the feeder γ-ray was interpolated by background regions of the centroid-difference spectrum. Regions which didn't show any contribution from peaks. These regions are marked by black cycles. The centroid-differences selected for the interpolation and the fitted curve are shown in Figure 6.11b. The behavior of the data points before and after the location of the full-energy peak supports the picture of the Compton edge.

The data points were fitted (red curve, the black dashed lines represent the errors on the fit) and the ΔC_{BG}^{f} was found to be 71 (3) ps at the location of the full-energy peak of the feeding γ-ray. The P/B was measured from the $LaBr_3$ spectrum (Figure 6.10) and found to be 0.40 (8). The background used was the one noted as "Possible BG 2". The errors given here includes the systematic errors defined by the different results of the P/B by choosing the other two possible backgrounds.

For the calculation of the $t_{cor}(E_{feeder})$ the following values were used: ΔC_{exp}= 66 (3) ps, ΔC_{BG}^{f}= 71 (3) ps and $P/B(E_f)$= 0.40 (8). All these resulted in $t_{cor}(E_{feeder})$= -13 (10) ps.

The same procedure was followed for the $t_{cor}(E_{decay})$. The analysis is shown in Figure 6.12. For the calculation of the $t_{cor}(E_{decay})$ the following values were used: ΔC_{exp}= 66 (3) ps, ΔC_{BG}^{d}= 31 (4) ps and $P/B(E_d)$= 0.57 (15). All these resulted in $t_{cor}(E_{decay})$= 60 (9) ps. The correction factor was measured to be t_{cor}= 24 (7) ps.

The PRD(E_{feeder}-E_{decay}) was measured to be -25 (2) ps by using the calibration shown in Chapter 5. The lifetime of the 4_1^+ state of ^{148}Ce by using the equation (6.1) was measured to be $\tau_{4_1^+}$= 58 (4) ps.

6.3.2 Background-subtracted prompt-shaped time spectra

The second technique used in order to remove the background contribution to the time spectrum was the one used in the case of the lifetime of the 2_1^+ state shown in

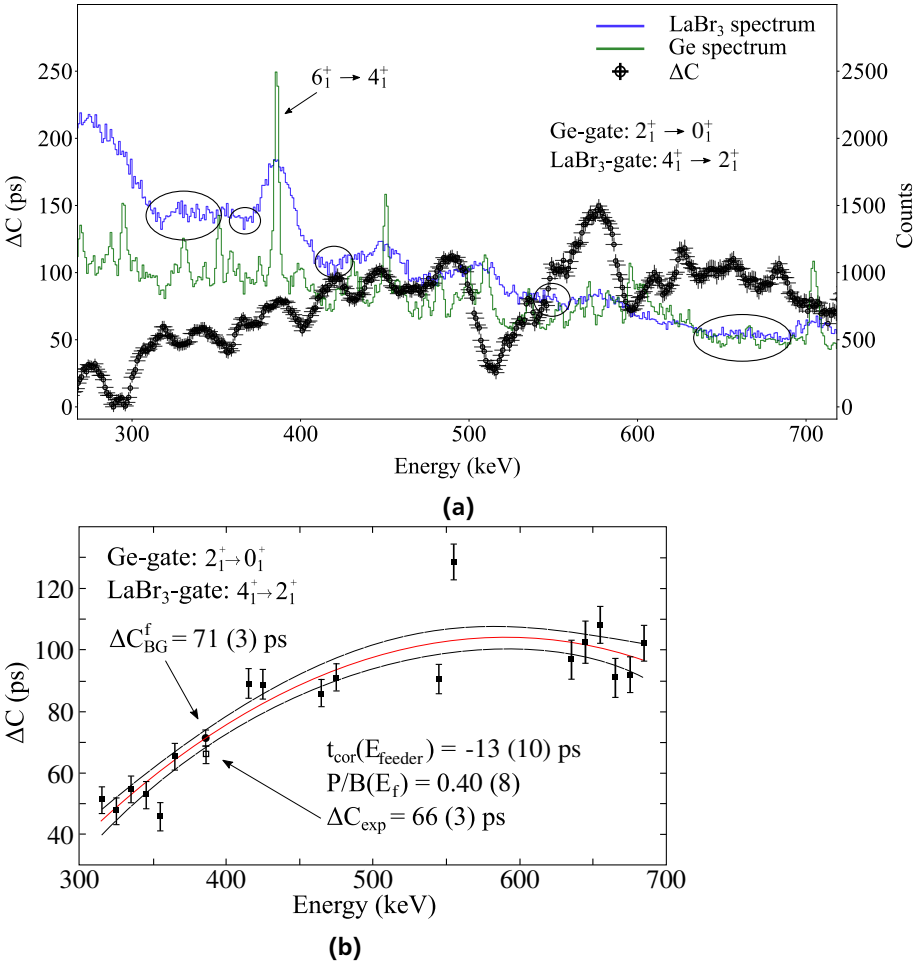

Figure 6.11.: (a) The centroid-difference spectrum, black points, for the interpolation of the time-background near the 386 keV peak of the $6_1^+ \rightarrow 4_1^+$ γ-ray. The energy step used for the second gate in the $LaBr_3$ detectors was 1 keV. The width of the energy gate was 10 keV. The whole energy spectrum was scanned. The Ge and $LaBr_3$ spectra generated for the definition of the background regions are also shown. (b) The fit for the interpolation of the time-background.

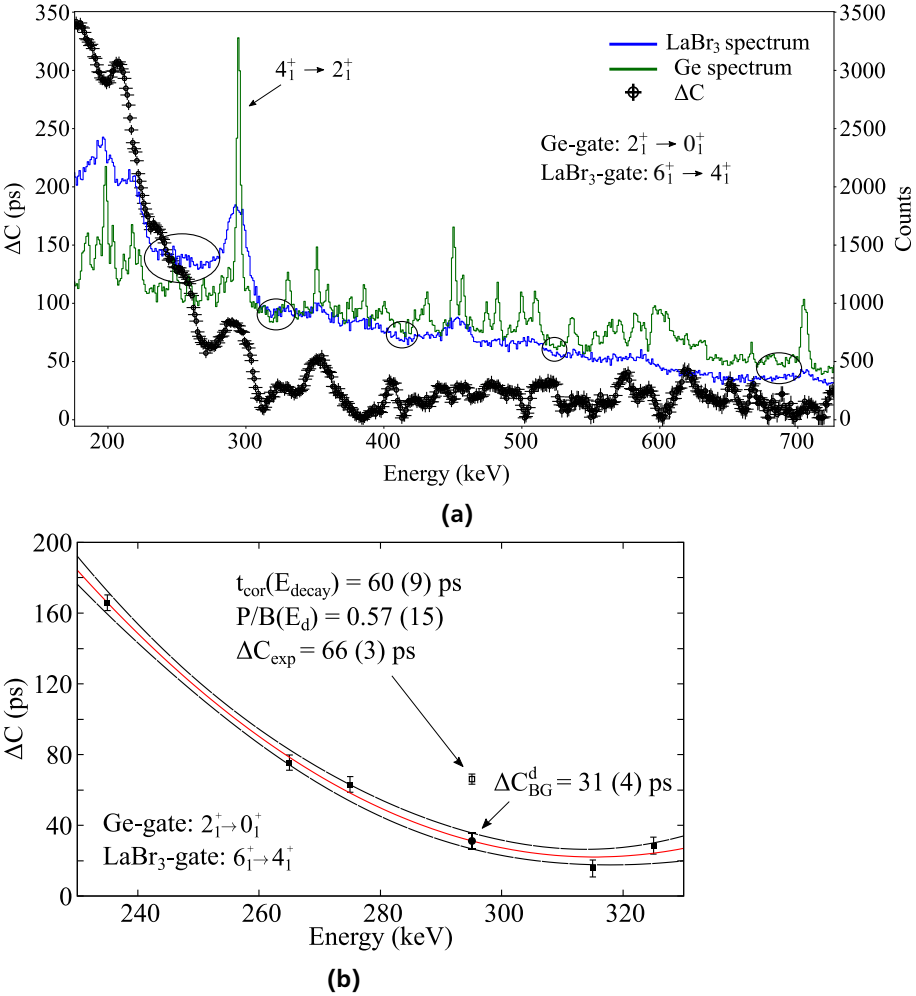

Figure 6.12.: (a) The centroid-difference spectrum, black points, for the interpolation of the time-background near the 295 keV peak of the $4_1^+ \rightarrow 2_1^+$ γ-ray. The energy step used for the second gate in the $LaBr_3$ detectors was 1 keV. The width of the energy gate was 10 keV. The whole energy spectrum was scanned. The Ge and $LaBr_3$ spectra generated for the definition of the background regions are also shown. (b) The fit for the interpolation of the time-background.

Section 6.2.1. The same method was followed, by setting additional energy gate-conditions (background gates), A_1' and B_1', (see Table 6.1) in the background-region of the peaks in the $LaBr_3$ spectra. The time-difference spectra were generated following the coincidence logic A_1B_1-A_1B_1'-$A_1'B_1$+$A_1'B_1'$. The individuals delayed time spectra are shown in Figure 6.13a. In figure 6.13b the resulting background-corrected time-difference spectra are shown, delayed and anti-delayed.

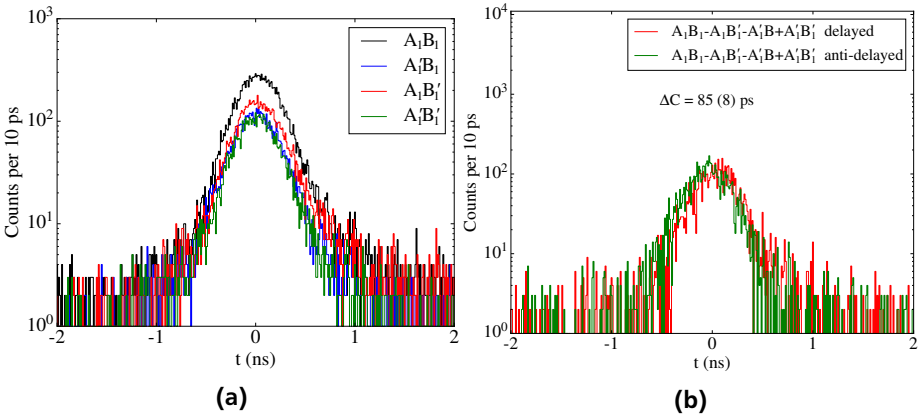

Figure 6.13.: (a) The individuals time spectra for the subtraction of the time background. (b) The delayed and anti-delayed time spectra following the coincidence logic A_1B_1-A_1B_1'-$A_1'B_1$+$A_1'B_1'$ for the lifetime of the 4_1^+ state of ^{148}Ce.

From the centroid difference (ΔC= 85 (8)), the PRD(E_{feeder}-E_{decay})= -25 (2) and the GCDM (equation (4.4)) the lifetime of the 4_1^+ state of ^{148}Ce was measured to be $\tau_{4_1^+}^{sub}$= 55 (6) ps [2]. The error includes the statistical error and the systematic error. The systematic error was checked by changing the position of the background gates, to A_1'' and B_1''.

6.4 Results and discussion

The determined lifetimes measured allow the calculation of the transition strengths (reduced transition probabilities). The lifetime (τ) of a state is connected with the transition probability $T_{fi}^{(\sigma\lambda)}$ [79] by

[2] The "*sub*" notation stands for the *background-subtracted time spectra* used.

$$\tau = \frac{1}{T_{fi}^{(\sigma\lambda)}}, \tag{6.4}$$

where

$$T_{fi}^{(\sigma\lambda)} = \frac{8\pi}{\hbar}\frac{\lambda+1}{\lambda[(2\lambda+1)!!]^2}\left(\frac{E_\gamma}{\hbar c}\right)^{2\lambda+1} B(\sigma\lambda; J_i \to J_f), \tag{6.5}$$

where σ denotes either the electric (E) or magnetic (M) character and λ the angular momentum of a transition between two states ($J_i^\pi \to J\pi_f$, where π, here, is the parity), $B(\sigma\lambda; J_i \to J_f)$ is the reduced transition probability, and E_γ the transition energy [79]. For electric transitions with angular momentum λ=2 the transition probability is given by [79]

$$T_{fi}^{(\sigma\lambda)} = 5.498 \times 10^{22}\frac{\lambda+1}{\lambda[(2\lambda+1)!!]^2}\left(\frac{E_\gamma}{197.33}\right)^{2\lambda+1} B(\sigma\lambda; J_i \to J_f), \tag{6.6}$$

in 1/s units. The B(Eλ) is in units of $e^2fm^{2\lambda}$. The reduced transition probability B(Eλ) is commonly used in *Weisskopf units* (W.u.), or *Weisskopf single-particle estimate*, [80]

$$B_W(E\lambda) = \frac{1.2^{2\lambda}}{4\pi}\left(\frac{3}{\lambda+3}\right)A^{2\lambda/3}e^2 f m^{2\lambda}, \tag{6.7}$$

where A is the atomic mass number.

The lifetimes measured are shown in Table 6.2. The notations are used, as in the text in the previous sections, for the different handling of the data to result on the lifetime. For the lifetime of the 2_1^+ state the two results, $\tau_{2_1^+}$ and $\tau_{2_1^+}^{sub}$, agrees between each other, within the errors. The same occurs for the transition strength B(E2; $2_1^+ \to 0_1^+$) as shown also in Table 6.2. The same occurs for the lifetime of the 4_1^+ state. The $\tau 4_1^+$ and the $\tau_{4_1^+}^{sub}$ (and the transition strength B(E2; $4_1^+ \to 2_1^+$)) agrees between each other, within the errors.

For the calculation of the $B_{4/2}$ ratio the $\tau_{2_1^+}$ and $\tau_{4_1^+}$ results will be used. The ratio results in the value $B_{4/2}$= 1.52 (11). The ratio seems to deviate from both the typical values for a vibrator and a rigid-rotor (2 and 1.4 respectively, see Chapters 1 and 2), setting the nucleus, together with its heavier $N = 90$ isotones, near the CP of the QSPT, as it is shown in Figure 6.14. If the $\tau_{2_1^+}^{sub}$ and the $\tau_{4_1^+}^{sub}$ values are adopted the resulting transition strengths ratio is $B_{4/2}^*$= 1.55 (19). The two values agree within the errors.

Table 6.2.: Lifetimes and transition strengths in ^{148}Ce obtained from the present work.

J_i^π	notation	τ	τ - lit.	J_f^π	$B(E2; J_i^\pi \rightarrow J_f^\pi)$
2_1^+	$\tau_{2_1^+}$	1.466 (50) ns	1.457 (87) ns [74]	0_1^+	85.2 (29) W.u.
2_1^+	$\tau^{sub}_{2_1^+}$	1.430 (82) ns	1.457 (87) ns [74]	0_1^+	87.3 (50) W.u.
4_1^+	$\tau_{4_1^+}$	58 (4) ps		2_1^+	129 (9) W.u.
4_1^+	$\tau^{sub}_{4_1^+}$	55 (6) ps		2_1^+	135 (15) W.u.

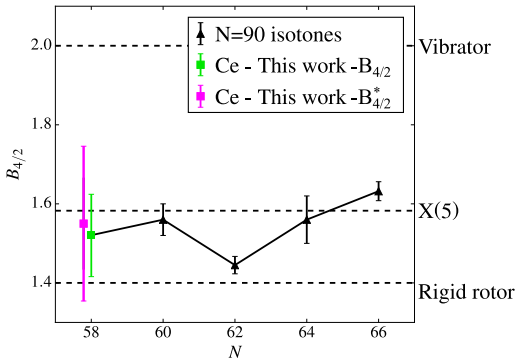

Figure 6.14.: The $B_{4/2}$ ratios of the N=90 isotones. The typical values (benchmarks) for the U(5) symmetry, SU(3) symmetry and the X(5) model (which describe nuclei near the CP of the QSPT) are marked. All N=90 isotones lies near the CP.

In order to understand the QSPT, in the following Chapters the experimental data for ^{148}Ce is being compared with (a) several geometrical models approximating the transitional region around X(5), and (b) microscopic calculations for this nucleus using the five-dimensional quadrupole collective Hamiltonian, equation (7.1). Additionally the whole N≈90 region is being investigated with the IBM-1 calculations. The trajectories of cerium, neodymium and samarium isotopic chains in the IBM symmetry triangle are showing the shape evolution along the chains.

7 Discussion

In the previous Chapter the analysis for the 2_1^+ and the 4_1^+ lifetimes was presented. The resulting observable connected with the lifetimes, the $B_{4/2}$ ratio, together with all known experimental observables for the nucleus will be compared with the geometrical models presented in Chapter 2. Additionally they will be used in order to analyze the nuclei near the N=90 QSPT within the IBM-1 (Chapter 3) in order to include the influence of the γ-softness in the shape of the nucleus. The purpose of both the comparison and the IBM-1 analysis is to understand the evolution of shapes along the QSPT. The increasing γ-softness along the isotopic chains of cerium, neodymium and samarium will be also investigated in order to understand the different evolution of the $R_{4/2}$ and $B_{4/2}$ ratios over the neutron number, shown in Figure 1.5.

7.1 Comparison of experimental data of ^{148}Ce with geometrical models

The ^{148}Ce isotope is on the low-Z boundary of the $N = 90$ QSPT. The experimental results, presented in Chapter 6, indicate that the isotope is near the CP of the QSPT. If the assumption that the isotope is not axially deformed (γ=0^o) is taken, the experimental data can be compared with the observables of the geometrical solutions presented in Chapter 2. By this comparison the shape of the nucleus can be approached. The $R_{4/2}$=2.86 ratio seems to set it before the CP and so the comparison with one of the X(5)-β^{2n} models can give more information about the "distance" from the CP.

The energy levels emanating from the X(5), X(5)-β^8 and CBS models and the experimentally measured levels for the N=90 isotones are plotted side by side in Figure 7.1. The values of the key observables $R_{4/2}$, $E_{0_2^+}/E_{2_1^+}$ and $B_{4/2}$ can be seen in Table 7.1. **One can perceive the good agreement of ^{148}Ce with the X(5)-β^8 model**. Additionally to the $s = 1$ band, the experimental $E_{0_2^+}$ of ^{148}Ce fits with the X(5)-β^8 prediction for $E_{0_2^+}$<$E_{6_1^+}$. The agreement is also supported by Figure 7.2, where the energy ratios $E(J^+)/E(2^+)$, with $J \leq 14$, are plotted for a vibrator, a rigid-rotor, X(5) and X(5)-β^{2n} models and the experimental data of ^{148}Ce. One can see that for increasing n, X(5)-β^{2n} models are approaching X(5). For $J \leq 6$ the experimental ratios seems to agree with all models. For $J > 6$ the experimental data fit with high precision with the X(5)-β^8 model.

As it was explained before, nuclei with fitting observables with the X(5)-β^{2n} are on the spherical side of the CP. By making the assumption that ^{148}Ce is axially symmetric (γ=0^o), the agreement with X(5)-β^8 shows that the nucleus is placed near the CP. In the next Section this assumption will be checked by the investigation of the cerium isotopic chain, with N=86-90, within the IBM-1.

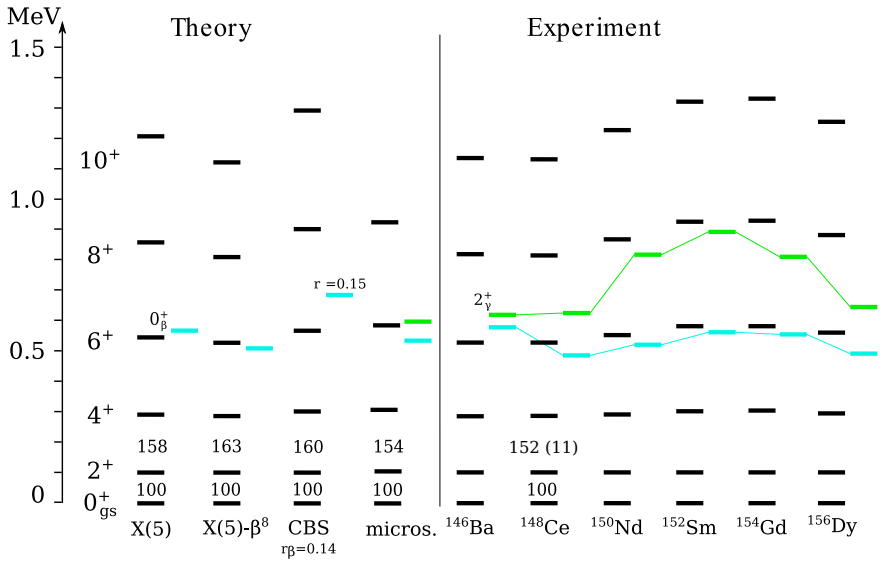

Figure 7.1.: Comparison of energy spectra between theories and the adopted experimental data for N=90 isotones. The energies of the levels of each isotope are normalized to the energy of the 2_1^+ state which is shifted to 100 keV. The 0_2^+ states are plotted with blue and the 2_γ^+ states are plotted with green. The $B(E2)$ values presented are normalized at $B(E2; 2_1^+ \rightarrow 0_1^+) = 100$. One can see the good agreement of the experimental data for ^{148}Ce with the X(5)-β^8 model and the microscopic calculations. The trend of the 2_γ^+ states shows increasing γ-softness around ^{152}Sm.

7.2 Isotopic chains in the IBM symmetry triangle

The importance of the axially asymmetry will be shown in this Section by investigating the isotopic chains of cerium, neodymium and samarium (around N=90)

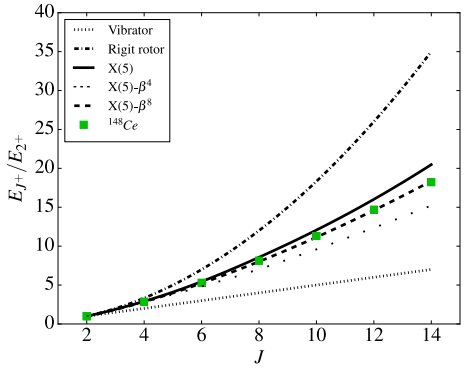

Figure 7.2.: Comparison of energy ratios $E(J^+)/E(2^+)$ between a vibrator, a rigid-rotor, X(5) and X(5)-β^{2n} models and the experimental data of ^{148}Ce.

Table 7.1.: Comparison between experimental data of ^{148}Ce with geometrical models and the microscopic calculations.

	X(5)	X(5)-β^8 [18]	CBS [17] $r_\beta = 0.14$	Microscopic calculations	^{148}Ce Exp.
$R_{4/2}$	2.90	2.85	3.01	2.99	2.86
$E_{0_2^+}/E_{2_1^+}$	5.65	5.09	6.80	5.21	4.86
$B_{4/2}$	1.58	1.63	1.60	1.54	1.52(11)

within the IBM-1 (Chapter 3). For all the isotopes in the N=90 QSPT region the crossing of the $R_{4/2}$ and the $R_{0\gamma}$ contours is unique and allow their placement in the triangle. The IBM-1 calculations were performed with IBAR code for the corresponding N_B. The corresponding N_B had to be used as the contours for all observables are changing for different N_B [21].

7.2.1 IBM-1 calculations - Cerium isotopic chain

In Figure 7.3b the placement of the ^{148}Ce isotope is shown. For ^{148}Ce the experimental data for the two observables are: $R_{4/2} = 2.86$ and $R_{0\gamma} = -1.38$. The fitting $R_{4/2}$ contour is crossing the fitting $R_{0\gamma}$ contour in one point, with coordinates $\zeta = 0.64$ and $\chi = -0.94$. The same method has been used in order to define the trend of the cerium isotopic chain into the triangle. In Figure 7.4a the placements of the even-even cerium isotopes with N=86-90 are shown together with the PT-lines for the corresponding valance boson numbers N_B=6-8. For ^{144}Ce the energy of the 0_2^+ is not known experimentally, so the area inside the triangle where it is placed was defined with the energy ratio $R_{4/2}$. This contour is "vertical" so the χ parameter could not be determined at all and the ζ parameter was only limited between 0.5 and 0.6.

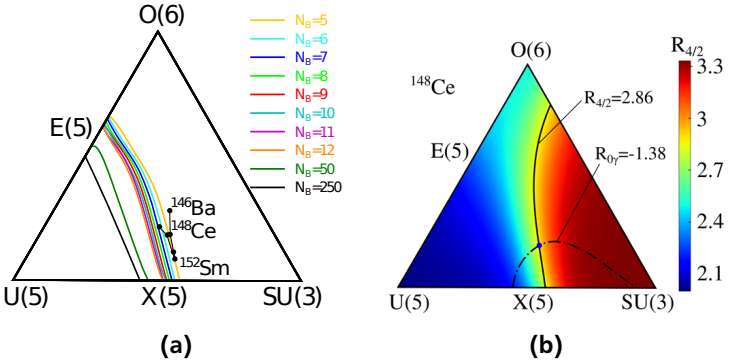

Figure 7.3.: (a) PT-lines for several boson numbers 5-12, 50 and 250. The placement of all N=90 isotones, with Z=56-64, in the IBM symmetry triangle is shown. (b) Placement of ^{148}Ce in the symmetry triangle.

The ^{146}Ce isotope is placed on the spherical side of the PT-line for N_B=7 and ^{148}Ce on the deformed side of the PT-line for N_B=8. This means that the CP of

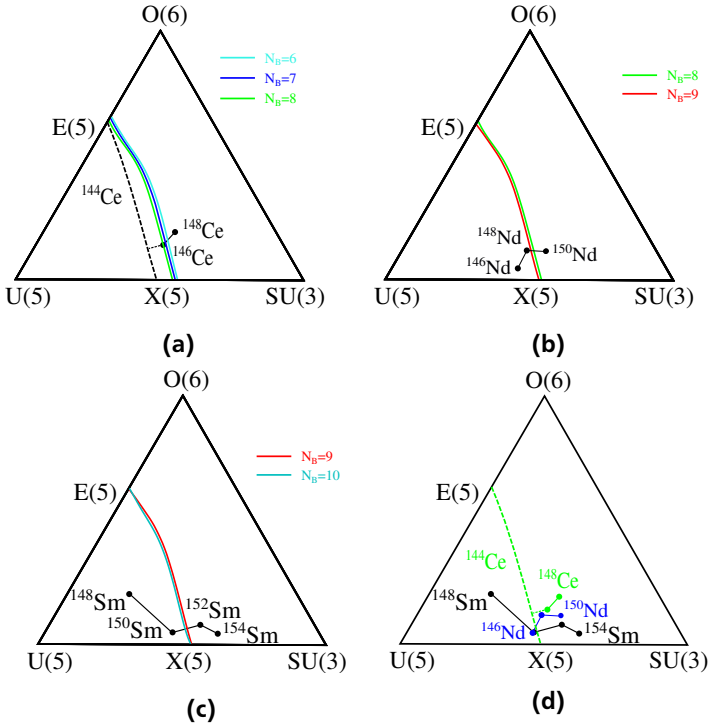

Figure 7.4.: Trajectories of the (a) cerium, (b) neodymium and (c) samarium isotopic chains in the IBM symmetry triangle. ^{144}Ce is placed along the black dashed line (which corresponds in the $R_{4/2}$ contour) because the $E(2^+_\gamma)$ energy is not known. (d) All trajectories plotted together for easier comparison.

the QSPT is between the two isotopes. For ^{146}Ce, the potential minimum is located at β=0, hence the nucleus in its ground state is dominated by a spherical configuration, and in the opposite side, for ^{148}Ce the minimum is located at $\beta \neq$0, hence the nucleus in its ground state is dominated by a deformed configuration. **The deformed picture for ^{148}Ce is in contradiction to the results of the analysis within the geometrical models, and X-β^8 in particular which describes nuclei before the QSPT, where the spherical minimum contributes mostly to the nuclear shape.**

The isotopic chain is not near the base of the triangle indicating some γ-softness. The coordinates of the isotopes in the triangle can been seen in Table 7.2. In the table the $\gamma_{eff.}^{appr.}$ are also given for the cerium isotopes. They were calculated as described in Chapter 3, by the code IBAR for the corresponding ζ,χ and N_B and the equations (3.12) and (3.14). For ^{144}Ce the calculations could not be done because of the undefined χ parameter. The values show that the γ-softness for both the N=88 and N=90 isotopes is $\gamma_{eff.}^{appr.} \approx 10^o$.

7.2.2 IBM-1 calculations - Neodymium and samarium isotopic chains

The placement of the even-even samarium isotopes (with N=86-92) into the triangle (see Figure 7.4b) reveals the lower γ-softness of the isotopic chain for N=88-92. Again the crossing from the spherical side to the deformed side of the CP of the PT is between the N=88 and N=90 isotopes, like in the cerium isotopic chain, but the χ parameters along the samarium chain are decreasing, showing less γ deformation, with increasing neutron number. The whole isotopic chain for N=88-92 stays near the base of the triangle (U(5)-SU(3) leg). The $\gamma_{eff.}^{appr.}$ values calculated for the samarium isotopes show a drastic decreasing of the γ-softness for increasing neutron number from N=86 to N=90 (see Figure 7.5a). The near to zero value for ^{152}Sm explains the good description of the isotope by the CBS model which considers the γ-part of the nuclear potential as an harmonic oscillator (potential minimum at γ=0) [17].

For the neodymium isotopic chain the placement of the isotopes is shown in Figure 7.4c. Again the crossing from the spherical side to the deformed side of the CP of the PT is between the N=88 and N=90 isotopes, as in cerium and samarium isotopic chains. From Figure 7.5a and the $\gamma_{eff.}^{appr.}$ values the same picture as for samarium isotopic chain seems to occur. The $\gamma_{eff.}^{appr.}$ values show a drastic decreasing of the γ-softness for increasing neutron number from N=88 to N=90.

Table 7.2.: Coordinates of isotopes in the IBM symmetry triangle. *The placement of ^{144}Ce in one spot was not possible because the energy of the 0_2^+ state is not experimentally known. The isotope was placed in an area instead, using the energy ratio $R_{4/2}$. The $\gamma_{eff.}^{appr.}$, calculated from the $K_3^{appr.}$ parameter as described in Chapter 3, is given for each isotope. The N=90 isotones are in "bold" for easier comparison.

Isotope	ζ	χ	$\gamma_{eff.}^{appr.}$
^{146}Ba	**0.69**	**-0.78**	**12^o**
^{144}Ce*	0.5 to 0.6	0 to $-\sqrt{7}/2$	
^{146}Ce	0.59	-1.02	10^o
^{148}Ce	**0.64**	**-0.94**	**9^o**
^{146}Nd	0.50	-1.17	12^o
^{148}Nd	0.56	-1.04	14^o
^{150}Nd	**0.62**	**-1.08**	**5^o**
^{148}Sm	0.43	-0.68	23^o
^{150}Sm	0.51	-1.14	11^o
^{152}Sm	**0.61**	**-1.13**	**1^o**
^{154}Sm	0.65	-1.23	3^o
^{154}Gd	**0.63**	**-0.93**	**7^o**
^{156}Dy	**0.62**	**-0.87**	**8^o**

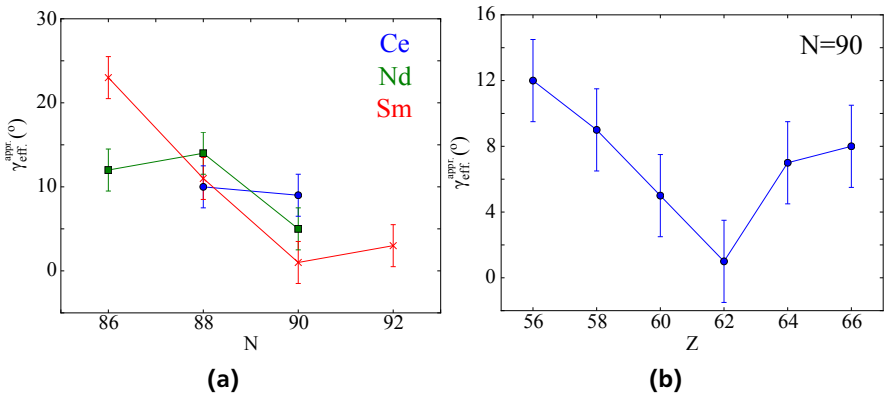

Figure 7.5.: The calculated $\gamma_{eff.}^{appr.}$ for (a) the cerium, neodymium and samarium isotopic chains and (b) for the N=90 isotones.

7.2.3 Crossing χ parameter

For each isotopic chain there is a crossing χ-parameter where the line connecting the N=88 and N=90 isotopes is crossing the PT-line for the boson number of the N=90 isotope of the isotopic chain. As can be seen in Figure 7.4d the crossing χ-parameter is increasing for decreasing Z (-1.13 for samarium, -1.06 for neodymium and -1 for cerium). This picture can be connected with the different derivatives of the binding energy for different N_B[22].

In Figure 7.6 the first derivative of the binding energy over ζ for several boson numbers and χ parameters are shown. Each line depends on a N_B and χ parameter combination (N_B ,χ). Those combinations correspond on the N_B of the N=90 isotope and the crossing χ-parameter of each isotopic chain (plotted in black). Additionally the line for N_B =250 and χ=-1 is plotted in blue (multiplied by 0.05 for easier comparison). One can see in Figure 7.6 that the discontinuity of a first-order PT develops only in the large N_B limit (N_B =250). For small N_B it is smoothed out, less for samarium and more for neodymium and cerium.

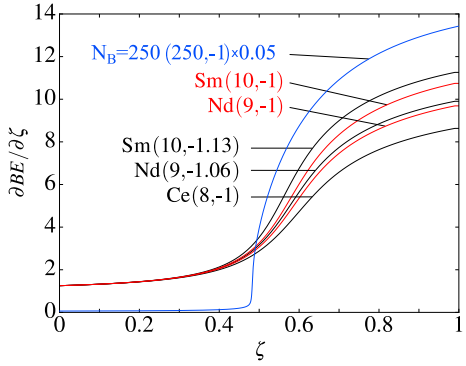

Figure 7.6.: First derivative of the binding energy for multiple N_B and χ parameters. Each line corresponds in a N_B and χ parameter combination (N_B ,χ). The N_B =250 line is multiplied by 0.05 for easier comparison.

The difference between samarium, neodymium and cerium is mainly due to the different crossing χ-parameter and less to the different N_B. Changes on the latter are causing smaller changes in the binding energy, as it can be seen in the comparison of the Ce(8,-1) line with the two red lines in Figure 7.6, which correspond to the same χ parameter for N_B=9 and 10, i.e. for neodymium and samarium isotopes on N=90.

As γ-softness increases from samarium to cerium (for N=90), by decreasing Z, and in the same time the crossing χ-parameter is increasing, the crossing of the PT-line is less orthogonal. The smoothed out picture can be interrelated with the changes of the structural fingerprints plotted in Figure 1.5a, where the decreasing sharpness of the transition from spherical to deformed structures for decreasing Z is shown. Hence the crossing χ-parameter, i.e. the γ-softness, can be associated with the sharpness of the QSPT. The same picture can be seen in the $R_{4/2}$ and $B_{4/2}$ observables from the IBM-1 calculations (Figure 7.7). This shows a connection between the non-orthogonal crossing of the PT-line in a finite-N system and the smoother $R_{4/2}$ and $B_{4/2}$ systematics.

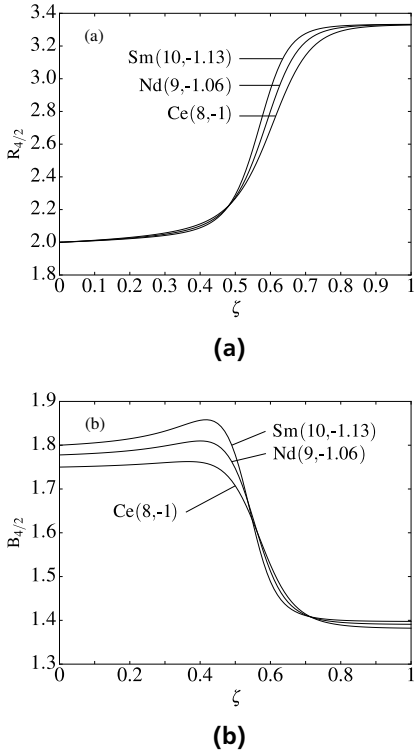

Figure 7.7.: (a) $R_{4/2}$ and (b) $B_{4/2}$ ratios from IBM-1 calculations. Each line depends on a N_B and χ parameter combination (N_B ,χ).

7.2.4 IBM-1 calculations - N=90 isotones

The same procedure for placing the nuclei in the IBM triangle has been followed to map the N=90 isotones, with Z=56-66, in the triangle. The resulting coordinates for the isotopes and their placement in the triangle can been seen in Table 7.2 and Figure 7.3a, where all N=90 isotones are shown together with the corresponding PT-line, calculated with the IBAR code for the corresponding valence boson number. All the N=90 isotones are placed on the deformed side of their corresponding PT-line.

Both ^{152}Sm and ^{150}Nd are located near the base of the triangle, revealing a high degree of axial symmetry, more for ^{152}Sm. The other isotopes, with lower and higher Z, are placed symmetrically around them and closer to the O(6) symmetry, revealing higher γ-softness. The same picture occurs for the N=90 isotones from the $\gamma_{eff.}^{appr.}$ parameters shown in Figure 7.5b. The minimum $\gamma_{eff.}^{appr.}$ value is observed for ^{152}Sm. In Figure 7.1 the energy spectra of the N=90 isotones are plotted, the 0_2^+ and the 2_γ^+ states are also plotted. The spacing between the 2_γ^+ and the 0_2^+ states peaks in ^{152}Sm, indicating the low γ-softness of the nucleus.

7.3 Microscopic calculations

The analysis within the geometrical models considers the γ part of the nuclear potential to be a harmonic oscillator around γ=0. For nuclei with low γ-softness this analysis and its results are reliable. From the IBM-1 analysis the cerium isotopic chain shows increased γ-softness. From the placement of ^{148}Ce in the IBM symmetry triangle and the calculation of the $\gamma_{eff.}^{appr.}$ parameter, the γ-deformation parameter seems to play some role in the shape of the nucleus ($\gamma_{eff.}^{appr.}$=9^o). Microscopic calculations were performed in order to reveal the γ-softness of the nucleus [81]. The calculations were made by Tamara Nikšić and Dario Vretenar using the five-dimensional quadrupole collective Hamiltonian,

$$\hat{H}_{coll} = \hat{T}_{vib} + \hat{T}_{rot} + V_{coll}, \tag{7.1}$$

as described in Ref. [82] [1].

In Figure 7.8 the potential energy surface of ^{148}Ce is plotted. The equilibrium minimum (red dot) is located at $\beta \approx 0.25$, indicating some β-deformation.

[1] The interested reader can read more about microscopic analysis of the $N = 90$ QSPT region in Refs. [82, 83] and [84].

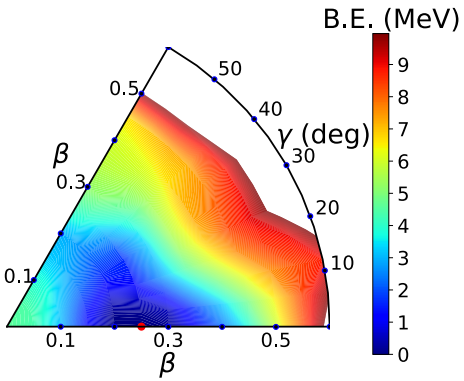

Figure 7.8.: Self-consistent triaxial quadrupole constrained energy surfaces in the $\beta - \gamma$ plane ($0 \leq \gamma \leq 60°$) of ^{148}Ce. The calculations were made by Tamara Nikšić and Dario Vretenar using the five-dimensional quadrupole collective Hamiltonian (equation (7.1)) [81].

In comparison with the results, in Ref. [82], for ^{152}Sm, ^{154}Gd and ^{156}Dy the β-deformation is smaller in the ^{148}Ce. Around the minimum there is an area with low values which shows higher γ-softness. Additionally, the collective wave functions, plotted in Figure 7.9, appear to display mixing in the γ direction. A minimum on $\gamma \approx 25\,°$ appears on the evolution of the second exited band, on the 2_2^+ excited state (Figures. 7.9b and 7.9e). And a minimum on $\gamma \approx 40\,°$ appears on the 0_3^+ excited state (Figure 7.9c).

The agreement of the microscopic calculations with the experimental data can be seen in Figure 7.1 and Table 7.1 where the spectrum and observables emanating from the calculations are shown next to the adopted values for ^{148}Ce. The transition strengths, $B(E2; 2_1^+ \rightarrow 0_1^+)$ and $B(E2; 4_1^+ \rightarrow 2_1^+)$, agree with the experimentally measured ones. From the calculations $B(E2; 2_1^+ \rightarrow 0_1^+)$=80 W.u. and $B(E2; 4_1^+ \rightarrow 2_1^+)$=123 W.u., resulting on the ratio $B_{4/2}$=1.54. From this comparison the scenario of the increased γ-softness of ^{148}Ce, compared to ^{150}Nd and ^{152}Sm, is verified by the microscopic calculations.

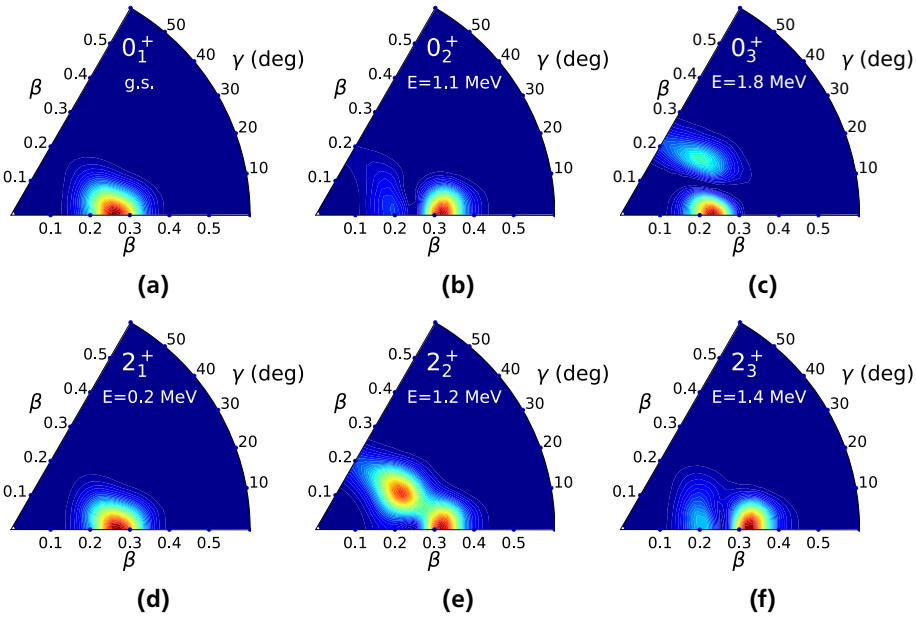

Figure 7.9.: (a-c) Probability distributions in the $\beta - \gamma$ plane for the lowest collective 0^+ states of ^{148}Ce. (d-f) Probability distributions in the $\beta - \gamma$ plane for the lowest 2^+ collective states of ^{148}Ce. The calculations were made by Tamara Nikšić and Dario Vretenar using the five-dimensional quadrupole collective Hamiltonian (equation (7.1)) [81].

8 Summary and outlook

The investigation of the QSPT in the even-even N=90 isotones [15], with Z=58-60 was presented in this doctoral thesis. The work was focused on the low-Z boundary of the N=88-90 QSPT. The structural observable $B_{4/2}$ of the ^{148}Ce was extracted for the first time by the experimental measurement of the lifetime of the 2_1^+ and 4_1^+ states with fast electronic timing techniques. The data were collected within the EXILL&FATIMA campaign which took place at the high-flux reactor at the ILL in Grenoble, France. Cold neutrons from the reactor were used to induce fission of ^{235}U and ^{241}Pu [60, 61], while the de-excitations of the fission fragments (among them the nucleus of interest, ^{148}Ce) were recored by a hybrid array of Ge and Ce-doped $LaBr_3$ detectors, the EXILL&FATIMA spectrometer [65, 66]. The two types of detectors allowed the selection of the cascade of interest and the measurement of the lifetimes. For the lifetime measurements the slope [51] method and the GCSM [53] were used. In the analysis multiple techniques were used to subtract the time-background contribution. The resulting lifetimes, $\tau_{2_1^+}$= 1.466 (50) ns and $\tau_{4_1^+}$= 58 (4) ps, entered the $B_{4/2}$= 1.52 (11) value, placing the nucleus near the CP of the QSPT.

Experimental observables, such as the $R_{4/2}$ and $B_{4/2}$ ratios and the location of the 0_2^+ state, were compared with geometrical models near the CP of the QSPT. The agreement with the X(5)-β^8 model seemed to imply dominant sphericity of ^{148}Ce. A deeper analysis which takes the finite size of the quantum system and the γ-degree of freedom into account, the analysis within the IBM-1, implied that ^{148}Ce is actually deformed. This picture was also supported by microscopic calculations. Furthermore, within the IBM-1, it was shown that the evolution of the QSPT at $N = 90$ is smoothed out as a function of decreasing proton number due to finite-N effects and increasing γ-softness.

For further understanding of the QSPT in the even-even N=90 isotones experimental structural observables should be measured with higher precision. This can be done by new experiments with higher precision on the selection of the nucleus on interest. In 2018 a fission experiment was performed in ILL where the prompt γ-rays could be selected over the γ-rays followed by the β-decay of the fission fragment. The selection was possible by placing the fission target in a liquid-scintillator and distinguish the γ-rays in coincidence with the β-particles from the ones in coincidence with the recoil of the fission fragments. With a better selection-mechanism

the lifetimes of higher-energy states would also be possible to be measured and transition strengths to be extracted.

Furthermore, microscopic calculations for cerium isotopes around ^{148}Ce would help on the understanding of the evolution of the γ-softness in the isotopic chain.

A Supplementary data for the IBM-1

A.1 $R_{4/2}$ derivative and the PT-line($R_{4/2}$)

A direct observable of the nucleus' shape, also experimentally accessible, is the energy spectrum. The energy ratio $R_{4/2} = E(4_1^+)/E(2_1^+)$ reveals the shape of the nucleus. It is shown that the CP of the PT occurs near to the turning point of the $R_{4/2}$, hence where the first derivative peaks [15, 20]. In Figure A.1 the $R_{4/2}$ and the first derivatives for $N_B = 8$ and multiple χ variables are plotted. For $\chi = 0$ the derivative peaks at $\zeta_{crit} = 0.56$, for infinite number of valence bosons $\zeta_{crit} = 0.5$. This difference occurs because of the finite number of bosons. The CPs for different χ variables was mapped into the IBM symmetry triangle. They form a line, for now on referred to as PT-line($R_{4/2}$). In Figure A.2 the PT-line($R_{4/2}$) is plotted for $N_B = 8$ and $N_B = 10$. The calculations have been made with IBAR code which performs IBM-1 calculations [42]. The PT-lines($R_{4/2}$) is not near the corresponding ζ_{deg} lines defined by Eqs. 3.8 and 3.10. The reason for this is the kinetic energy of the nucleus which is taken into account on the IBM-1 calculations.

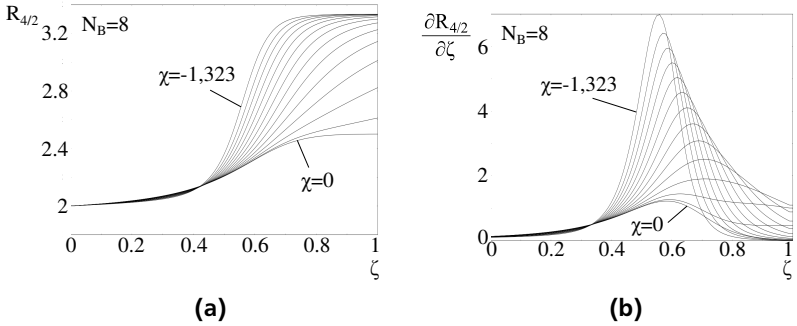

Figure A.1.: The $R_{4/2}$ and the first derivatives for $N_B = 8$ and multiple χ variables. χ step ≈0.1

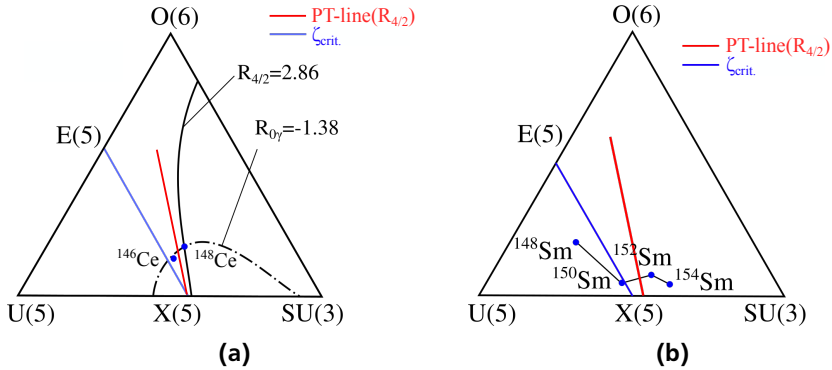

Figure A.2.: The placement of the isotopic chains together with the PT-lines($R_{4/2}$) defined by IBAR from the derivative of the $R_{4/2}$ and the ζ_{crit} defined by Eqs. 3.8 and 3.10 (a) for cerium and (b) samarium. The PT-lines($R_{4/2}$) differ from the ζ_{crit} lines. The QSPT occurs between the N=88 and N=90 isotopes.

B Supplementary data for the analysis

B.1 SOCOv2, commands and files

Command used for the event-building:

```
./soco2 event-builder -C ~/calib.conf -s ~/shifts -c ~/
    channel.conf -r ~/requirements.conf -o ~/out_folder -w
    20
```

`requirements.conf` file:

```
#type    min      max
#ft-triples (Clo-La-La):
CLOVER   1        4        #max 4 to allow for addback
LaBr     2        2
TAC      1        1
```

Command used for the gating:

```
./soco2 gate-spectra -C ~/calib.conf -c ~//channel.conf -e
    ~/exclude.conf -s ~/shifts -b ~/bgo.thresholds -a -g /
    gates.conf -o ~/out_folder -t ~/TAC-shiftij.conf ~/file.
    rlist
```

`gates.conf` file:

```
#ADDBACK type threshold_min threshold_max
ADDBACK CLOVER 384 389
ADDBACK LABR 293 298
```

`exclude.conf` file:

```
#LaBr_ID LaBr_ID
128      129
128      130
128      134
```

```
128     135
129     130
130     131
130     132
131     132
132     133
132     134
133     134
134     135
136     137
136     138
136     142
136     143
137     138
138     139
138     140
139     140
140     141
140     142
141     142
142     143
```

TAC-shiftij.conf file:

```
#LaBr_ID  LaBr_ID  TAC_ID  shift(channels)
128       129      144     144.4
128       130      144     128.6
128       131      144     138.6
128       132      144     32.2
...
140       143      156     62.6
141       142      157     31
141       143      157     21.8
142       143      158     79.2
```

Command used for the fast-timing matrix:

```
./soco2 ft-matrix -C ~/calib.conf -c ~/channel.conf -e ~/
    exclude.conf -s ~/shifts -b ~/bgo.thresholds -a -g ~/
    gates.conf -o ~/out_folder -t ~/TAC-shiftij.conf ~/file.
    rlist
```

Bibliography

[1] Davies Paul. *Forces of Nature*. Cambridge Univ. Press, 1986.

[2] *Quark*. In: *Encyclopædia Britannica*. Encyclopædia Britannica, inc., 2018.

[3] Roderick V Reid. *Local phenomenological nucleon-nucleon potentials*. In: *Ann. Phys.* 50.3 (1968), pp. 411 –448. DOI: 10.1016/0003-4916(68)90126-7.

[4] Yu. Ts. Oganessian et al. *Synthesis of the isotopes of elements 118 and 116 in the* ^{249}Cf *and* ^{245}Cm $+^{48}$ Ca *fusion reactions*. In: *Phys. Rev. C* 74 (2006), p. 044602. DOI: 10.1103/PhysRevC.74.044602.

[5] Maria Goeppert Mayer. *On Closed Shells in Nuclei. II*. In: *Phys. Rev.* 75 (1949), pp. 1969–1970. DOI: 10.1103/PhysRev.75.1969.

[6] Otto Haxel, J. Hans D. Jensen, and Hans E. Suess. *On the "Magic Numbers" in Nuclear Structure*. In: *Phys. Rev.* 75 (1949), pp. 1766–1766. DOI: 10.1103/PhysRev.75.1766.2.

[7] A. Bohr. *Mat. Fys. Medd. K. Dan. Vidensk. Selsk. 26, 14*. 1952.

[8] J. P. Delaroche et al. *Structure of even-even nuclei using a mapped collective Hamiltonian and the D1S Gogny interaction*. In: *Phys. Rev. C* 81 (2010), p. 014303. DOI: 10.1103/PhysRevC.81.014303.

[9] F. Iachello and A. Arima. *The interacting boson model*. Cambridge University Press, 2006.

[10] *Nuclear Data Sheets website*. URL: http://www.nndc.bnl.gov/ensdf/ (visited on 09/15/2018).

[11] R. F. Casten. *Nuclear Structure from a Simple Perspective*. Oxford University Press, 2005.

[12] E. A. McCutchan, D. Bonatsos, and N. V. Zamfir. *Connecting the X(5)-β^2, X(5)-β^4, and X(3) models to the shape/phase-transition region of the interacting boson model*. In: *Phys. Rev. C* 74 (2006), p. 034306. DOI: 10.1103/PhysRevC.74.034306.

[13] F. Iachello. *Dynamic Symmetries at the Critical Point*. In: *Phys. Rev. Lett.* 85 (2000), pp. 3580–3583. DOI: 10.1103/PhysRevLett.85.3580.

[14] F. Iachello. *Analytic Description of Critical Point Nuclei in a Spherical-Axially Deformed Shape Phase Transition*. In: *Phys. Rev. Lett.* 87 (2001), p. 052502. DOI: 10.1103/PhysRevLett.87.052502.

[15] R. F. Casten. *Shape phase transitions and critical-point phenomena in atomic nuclei*. In: *Nat. Phys.* 2 (2006), pp. 811–820. DOI: 10.1038/nphys451.

[16] R. F. Casten and N. V. Zamfir. *Empirical Realization of a Critical Point Description in Atomic Nuclei*. In: *Phys. Rev. Lett.* 87 (2001), p. 052503. DOI: 10.1103/PhysRevLett.87.052503.

[17] N. Pietralla and O. M. Gorbachenko. *Evolution of the "β excitation" in axially symmetric transitional nuclei*. In: *Phys. Rev. C* 70 (2004), p. 011304. DOI: 10.1103/PhysRevC.70.011304.

[18] D. Bonatsos et al. *Sequence of potentials interpolating between the U(5) and E(5) symmetries*. In: *Phys. Rev. C* 69 (2004), p. 044316. DOI: 10.1103/PhysRevC.69.044316.

[19] J. Jolie et al. *Quantum Phase Transition for γ-Soft Nuclei*. In: *Phys. Rev. Lett.* 87 (2001), p. 162501. DOI: 10.1103/PhysRevLett.87.162501.

[20] V. Werner et al. *Singular character of critical points in nuclei*. In: *Phys. Lett. B* 527.1 (2002), pp. 55 –61. DOI: 10.1016/S0370-2693(02)01160-7.

[21] D. Bonatsos et al. *Simple Empirical Order Parameter for a First-Order Quantum Phase Transition in Atomic Nuclei*. In: *Phys. Rev. Lett.* 100 (2008), p. 142501. DOI: 10.1103/PhysRevLett.100.142501.

[22] P. Koseoglou et al. *N=90 QSPT: Cerium, neodymium and samarium isotopic chains in the IBM symmetry triangle*. In: *Proceedings of the HNPS2018, the 27th Annual Symposium of the Hellenic Nuclear Physics Society*. Vol. 0,2018. 2019.

[23] A. Bohr and B. R. Mottelson. *Nuclear Deformation, Vol.2 of Nuclear Structure*. World scientific, Singapore, 1998.

[24] Elizabeth Anne Triano Ricard. *Critical phase/shape transitions in heavy nuclei*. PhD thesis. Yale University, 2006.

[25] L. Wilets and M. Jean. *Surface Oscillations in Even-Even Nuclei*. In: *Phys. Rev.* 102 (1956), pp. 788–796. DOI: 10.1103/PhysRev.102.788.

[26] A. E. L. Dieperink, O. Scholten, and F. Iachello. *Classical Limit of the Interacting-Boson Model*. In: *Phys. Rev. Lett.* 44 (1980), pp. 1747–1750. DOI: 10.1103/PhysRevLett.44.1747.

[27] J. N. Ginocchio and M. W. Kirson. *Relationship between the Bohr Collective Hamiltonian and the Interacting-Boson Model*. In: *Phys. Rev. Lett.* 44 (1980), pp. 1744–1747. DOI: 10.1103/PhysRevLett.44.1744.

[28] K. Dusling and N. Pietralla. *Description of ground-state band energies in well-deformed even-even nuclei with the confined β-soft rotor model*. In: *Phys. Rev. C* 72 (2005), p. 011303. DOI: 10.1103/PhysRevC.72.011303.

[29] A. Arima and F. Iachello. *Collective Nuclear States as Representations of a SU(6) Group*. In: *Phys. Rev. Lett.* 35 (1975), pp. 1069–1072. DOI: 10.1103/PhysRevLett.35.1069.

[30] O. Scholten, F. Iachello, and A. Arima. *Interacting boson model of collective nuclear states III. The transition from SU(5) to SU(3)*. In: *Ann. Phys.* 115.2 (1978), pp. 325 –366. DOI: 10.1016/0003-4916(78)90159-8.

[31] P. Cejnar, J. Jolie, and R. F. Casten. *Quantum phase transitions in the shapes of atomic nuclei*. In: *Rev. Mod. Phys.* 82 (2010), pp. 2155–2212. DOI: 10.1103/RevModPhys.82.2155.

[32] A. Arima and F. Iachello. *Interacting boson model of collective states I. The vibrational limit*. In: *Ann. Phys.* 99.2 (1976), pp. 253 –317. DOI: 10.1016/0003-4916(76)90097-X.

[33] A. Arima and F. Iachello. *Interacting boson model of collective nuclear states II. The rotational limit*. In: *Ann. Phys.* 111.1 (1978), pp. 201 –238. DOI: 10.1016/0003-4916(78)90228-2.

[34] A. Arima and F. Iachello. *Interacting boson model of collective nuclear states IV. The O(6) limit*. In: *Ann. Phys.* 123.2 (1979), pp. 468 –492. DOI: 10.1016/0003-4916(79)90347-6.

[35] D. D. Warner and R. F. Casten. *Revised Formulation of the Phenomenological Interacting Boson Approximation*. In: *Phys. Rev. Lett.* 48 (1982), pp. 1385–1389. DOI: 10.1103/PhysRevLett.48.1385.

[36] D. D. Warner and R. F. Casten. *Predictions of the interacting boson approximation in a consistent Q framework*. In: *Phys. Rev. C* 28 (1983), pp. 1798–1806. DOI: 10.1103/PhysRevC.28.1798.

[37] P. O. Lipas, P. Toivonen, and D.D. Warner. *IBA consistent-Q formalism extended to the vibrational region*. In: *Phys. Lett. B* 155.5 (1985), pp. 295 –298. DOI: 10.1016/0370-2693(85)91573-4.

[38] E. A. McCutchan, N. V. Zamfir, and R. F. Casten. *Mapping the interacting boson approximation symmetry triangle: New trajectories of structural evolution of rare-earth nuclei*. In: *Phys. Rev. C* 69 (2004), p. 064306. DOI: 10.1103/PhysRevC.69.064306.

[39] A. E. L. Dieperink and O. Scholten. *On shapes and shape phase transitions in the interacting boson model*. In: *Nucl. Phys. A* 346.1 (1980), pp. 125 –138. DOI: 10.1016/0375-9474(80)90492-3.

[40] J. N. Ginocchio and M. W. Kirson. *An intrinsic state for the interacting boson model and its relationship to the Bohr-Mottelson model*. In: *Nucl. Phys. A* 350.1 (1980), pp. 31 –60. DOI: 10.1016/0375-9474(80)90387-5.

[41] P. Van Isacker and Jin-Quan Chen. *Classical limit of the interacting boson Hamiltonian*. In: *Phys. Rev. C* 24 (1981), pp. 684–689. DOI: 10.1103/PhysRevC.24.684.

[42] R.J. Casperson. *IBAR: Interacting boson model calculations for large system sizes*. In: *Comput. Phys. Commun.* 183.4 (2012), pp. 1029 –1035. DOI: 10.1016/j.cpc.2011.12.024.

[43] L. D. Landau and E. M. Lifshitz. *Statistical Physics, Course of Theoretical Physics*. Vol. V.1. Oxford: Butterworth-Heinemann, 2001.

[44] W.-T. Chou, N. V. Zamfir, and R. F. Casten. *Unified description of collective nuclei with the interacting boson model*. In: *Phys. Rev. C* 56 (1997), pp. 829–838. DOI: 10.1103/PhysRevC.56.829.

[45] E. A. McCutchan and R. F. Casten. *Crossing contours in the interacting boson approximation (IBA) symmetry triangle*. In: *Phys. Rev. C* 74 (2006), p. 057302. DOI: 10.1103/PhysRevC.74.057302.

[46] Krishna Kumar. *Intrinsic Quadrupole Moments and Shapes of Nuclear Ground States and Excited States*. In: *Phys. Rev. Lett.* 28 (1972), pp. 249–253. DOI: 10.1103/PhysRevLett.28.249.

[47] D Cline. *Nuclear Shapes Studied by Coulomb Excitation*. In: *Annu. Rev. Nucl. Part. S.* 36.1 (1986), pp. 683–716. DOI: 10.1146/annurev.ns.36.120186.003343.

[48] R.V. Jolos et al. *Shape invariants in the multiple "Q-excitation" scheme*. In: *Nucl. Phys. A* 618.1 (1997), pp. 126 –140. DOI: 10.1016/S0375-9474(97)00046-8.

[49] V. Werner, C. Scholl, and P. von Brentano. *Triaxiality and the determination of the cubic shape parameter K_3 from five observables*. In: *Phys. Rev. C* 71 (2005), p. 054314. DOI: 10.1103/PhysRevC.71.054314.

[50] K.E.G. Löbner. *The electromagnetic interaction in nuclear spectroscopy*. Ed. by W.D. Hamilton. Amsterdam North-Holland Pub. Co, 1975, p. 173.

[51] P. C. Simms, N. Benczer-Koller, and C. S. Wu. *New Application of Delayed Coincidence Techniques for Measuring Lifetimes of Excited Nuclear States—Ca^{42} and Sc^{47}*. In: *Phys. Rev.* 121 (1961), pp. 1169–1174. DOI: 10.1103/PhysRev.121.1169.

[52] V. Werner et al. *Evolution of collectivity near mid-shell from excited-state lifetime measurements in rare earth nuclei*. In: *Phys. Rev. C* 93 (2016), p. 034323. DOI: 10.1103/PhysRevC.93.034323.

[53] J.-M. Régis et al. *The generalized centroid difference method for picosecond sensitive determination of lifetimes of nuclear excited states using large fast-timing arrays*. In: *Nucl. Instrum. Methods Phys. Res. A* 726 (2013), pp. 191 –202. DOI: 10.1016/j.nima.2013.05.126.

[54] J.-M. Régis et al. *The mirror symmetric centroid difference method for picosecond lifetime measurements via γ–γ coincidences using very fast LaBr3(Ce) scintillator detectors*. In: *Nucl. Instrum. Methods Phys. Res. A* 622.1 (2010), pp. 83 –92. DOI: 10.1016/j.nima.2010.07.047.

[55] H. Mach, R.L. Gill, and M. Moszyński. *A method for picosecond lifetime measurements for neutron-rich nuclei: (1) Outline of the method*. In: *Nucl. Instrum. Methods Phys. Res. A* 280.1 (1989), pp. 49 –72. DOI: 10.1016/0168-9002(89)91272-2.

[56] Gordon Gilmore and John D. Hemingway. *Practical gamma-ray spectrometry*. John Wiley & sons, 1995, p. 314.

[57] Z. Bay. *Calculation of Decay Times from Coincidence Experiments*. In: *Phys. Rev.* 77 (1950), pp. 419–419. DOI: 10.1103/PhysRev.77.419.

[58] J.-M. Régis et al. *The time-walk of analog constant fraction discriminators using very fast scintillator detectors with linear and non-linear energy response*. In: *Nucl. Instrum. Methods Phys. Res. A* 684 (2012), pp. 36 –45. DOI: https://doi.org/10.1016/j.nima.2012.04.088.

[59] M. Moszyński and B. Bengtson. *Status of timing with plastic scintillation detectors*. In: *Nucl. Instrum. Methods* 158 (1979), pp. 1 –31. DOI: 10.1016/S0029-554X(79)90170-8.

[60] D. Biswas et al. *EXILL - FATIMA*. In: *Institut Laue-Langevin (ILL)* (2013). DOI: 10.5291/ill-data.bag-03-3.

[61] D. Balabanski et al. *EXILL - Pu241 spectroscopy*. In: *Institut Laue-Langevin (ILL)* (2013). DOI: 10.5291/ill-data.bag-03-4.

[62] M. Jentschel et al. *EXILL—a high-efficiency, high-resolution setup for γ-spectroscopy at an intense cold neutron beam facility*. In: *JINST* 12.11 (2017), P11003. DOI: 10.1088/1748-0221/12/11/p11003.

[63] H. Abele et al. *Characterization of a ballistic supermirror neutron guide*. In: *Nucl. Instrum. Methods Phys. Res. A* 562.1 (2006), pp. 407 –417. DOI: 10.1016/j.nima.2006.03.020.

[64] W Urban et al. *New instrumentation for precise (n,γ) measurements at ILL Grenoble*. In: *JINST* 8.03 (2013), P03014. DOI: 10.1088/1748-0221/8/03/p03014.

[65] J.-M. Régis et al. *Germanium-gated γ-γ fast timing of excited states in fission fragments using the EXILL&FATIMA spectrometer*. In: *Nucl. Instrum. Methods Phys. Res. A* 763 (2014), pp. 210 –220. DOI: 10.1016/j.nima.2014.06.004.

[66] J. Jolie et al. *Test of the SO(6) selection rule in 196Pt using cold-neutron capture*. In: *Nucl. Phys. A* 934 (2015), pp. 1 –7. DOI: 10.1016/j.nuclphysa.2014.11.008.

[67] *EXOGAM website*. URL: http://pro.ganil-spiral2.eu/laboratory/detectors/exogam (visited on 12/06/2018).

[68] F. Azaiez. *EXOGAM: a γ-ray spectrometer for radioactive beams*. In: *Nucl. Phys. A* 654.1, Supplement 1 (1999), pp. 1003c –1008c. DOI: 10.1016/S0375-9474(00)88588-7.

[69] J. Simpson et al. *The EXOGAM array: A radioactive beam gamma-ray spectrometer*. English. In: *Acta Phys. Hung. NS-H* 11.1-2 (2000), pp. 159–188.

[70] J.-M. Régis *et al. The generalized centroid difference method for picosecond sensitive determination of lifetimes of nuclear excited states using large fast-timing arrays*. In: *Nucl. Instrum. Methods Phys. Res. A* 726 (2013), p. 191. DOI: 10.1016/j.nima.2013.05.126.

[71] S. Ilieva et al. *Measurement of picosecond lifetimes in neutron-rich Xe isotopes*. In: *Phys. Rev. C* 94 (2016), p. 034302. DOI: 10.1103/PhysRevC.94.034302.

[72] J.-M. Régis et al. *Reduced γ–γ time walk to below 50 ps using the multiplexed-start and multiplexed-stop fast-timing technique with LaBr3(Ce) detectors*. In: *Nucl. Instrum. Methods Phys. Res. A* 823 (2016), pp. 72 –82. DOI: 10.1016/j.nima.2016.04.010.

[73] Nima Saed-Samii. Diploma Thesis. Institut für Kernphysik, Universität zu Köln. 2013.

[74] N. Nica. *Nuclear Data Sheets for A = 148*. In: *Nucl. Data Sheets* 117 (2014), pp. 1 –229. DOI: 10.1016/j.nds.2014.02.001.

[75] J.-M. Régis et al. *$B(E2; 2_1^+ \rightarrow 0_1^+)$ value in ^{90}Kr*. In: *Phys. Rev. C* 90 (2014), p. 067301. DOI: 10.1103/PhysRevC.90.067301.

[76] P. Spagnoletti et al. *Half-life of the $15/2^+$ state of ^{135}I: A test of E2 seniority relations*. In: *Phys. Rev. C* 95 (2017), p. 021302. DOI: 10.1103/PhysRevC.95.021302.

[77] J.-M. Régis et al. *Abrupt shape transition at neutron number $N = 60$: $B(E2)$ values in ^{94,96,98}Sr from fast $\gamma - \gamma$ timing*. In: *Phys. Rev. C* 95 (2017), p. 054319. DOI: 10.1103/PhysRevC.95.054319.

[78] S. Ansari et al. *Experimental study of the lifetime and phase transition in neutron-rich ^{98,100,102}Zr*. In: *Phys. Rev. C* 96 (2017), p. 054323. DOI: 10.1103/PhysRevC.96.054323.

[79] Jouni Suhonen. *From Nucleons to Nucleus Concepts of Microscopic Nuclear Theory*. Springer, Berlin, Heidelberg, 2007.

[80] V. F. Weisskopf. *Radiative Transition Probabilities in Nuclei*. In: *Phys. Rev.* 83 (1951), pp. 1073–1073. DOI: 10.1103/PhysRev.83.1073.

[81] P. Koseoglou et al. *Low-Z boundary of the $N = 88$—90 shape phase transition: ^{148}Ce near the critical point*. (Submitted).

[82] Z. P. Li, T. Nikšić, and D. Vretenar. *Coexistence of nuclear shapes: self-consistent mean-field and beyond*. In: *J. Phys. G Nucl. Part. Phys.* 43.2 (2016), p. 024005. DOI: 10.1088/0954-3899/43/2/024005.

[83] Z. P. Li et al. *Microscopic analysis of nuclear quantum phase transitions in the $N \approx 90$ region*. In: *Phys. Rev. C* 79 (2009), p. 054301. DOI: 10.1103/PhysRevC.79.054301.

[84] T. T. Nikšić et al. *Microscopic Description of Nuclear Quantum Phase Transitions*. In: *Phys. Rev. Lett.* 99 (2007), p. 092502. DOI: 10.1103/PhysRevLett.99.092502.

Acronyms

ADC	analog-to-digital converter
BE	binding energy
BGO	bismuth germanate ($Bi_4Ge_3O_{12}$)
CBS	confined β-soft
CFD	constant fraction discriminator
CP	critical point
ECQF	extended constant Q formalism
FAN	fan-in/fan-out modules
FWHM	full width at half maximum
GCDM	generalized centroid difference method
Ge	high purity germanium
IBM	interacting boson model
ILL	Institut Laue-Langevin
PMT	photomultiplier tube
PRD	prompt response difference
PT	phase transition
PT-lines	phase transition lines (trajectories of $\zeta_{QSPT}(N_B, \chi)$ points, see Chapter 3.
QSPT	quantum shape phase transition
sub	background-subtracted
TAC	time-to-amplitude converter
ΔC	centroid difference

List of Figures

List of Tables

List of Publications

Publications in refereed journals

S. Stoulos, A. Ioannidou, E. Vagena, **P. Koseoglou** and M. Manolopoulou
Post-Chernobyl ^{137}Cs in the atmosphere of Thessaloniki: a consequence of the financial crisis in Greece
Journal of environmental radioactivity ***128*** *(2014) p.68.*

P. Koseoglou, E. Vagena, S. Stoulos and M. Manolopoulou
Neutron spectrum determination in a sub-critical assembly using the multi-disc neutron activation technique
Radiation Effects and Defects in Solids ***171*** *(2016) p.766.*

H. N. Liu, A. Obertelli, P. Doornenbal, C. A. Bertulani, G. Hagen, J. D. Holt, G. R. Jansen, T. D. Morris, A. Schwenk, R. Stroberg, N. Achouri, H. Baba, F. Browne, D. Calvet, F. Château, S. Chen, N. Chiga, A. Corsi, M. L. Cortés, A. Delbart, J.-M. Gheller, A. Giganon, A. Gillibert, C. Hilaire, T. Isobe, T. Kobayashi, Y. Kubota, V. Lapoux, T. Motobayashi, I. Murray, H. Otsu, V. Panin, N. Paul, W. Rodriguez, H. Sakurai, M. Sasano, D. Steppenbeck, L. Stuhl, Y. L. Sun, Y. Togano, T. Uesaka, K. Wimmer, K. Yoneda, O. Aktas, T. Aumann, L. X. Chung, F. Flavigny, S. Franchoo, I. Gašparić, R. -B. Gerst, J. Gibelin, K. I. Hahn, D. Kim, T. Koiwai, Y. Kondo, **P. Koseoglou**, J. Lee, C. Lehr, B. D. Linh, T. Lokotko, M. MacCormick, K. Moschner, T. Nakamura, S. Y. Park, D. Rossi, E. Sahin, D. Sohler, P.-A. Söderström, S. Takeuchi, H. Törnqvist, V. Vaquero, V. Wagner, S. Wang, V. Werner, X. Xu, H. Yamada, D. Yan, Z. Yang, M. Yasuda, L. Zanetti
How Robust is the N = 34 Subshell Closure? First Spectroscopy of ^{52}Ar
Physical Review Letters ***122****, 072502, (2019).*

P. Koseoglou, V. Werner, N. Pietralla, S. Ilieva, T. Nikšić, D. Vretenar, M. Thürauf, C. Bernards, A. Blanc, A. M. Bruce, R. B. Cakirli, N. Cooper, L. M. Fraile, G. de France, M. Jentschel, J. Jolie, U. Köster, W. Korten, T. Kröll, S. Lalkovski, H. Mach, N. Mărginean, P. Mutti, Z. Patel, V. Paziy, Zs. Podolyák, P. H. Regan, J.-M. Régis, O. J. Roberts, N. Saed-Samii, G. S. Simpson, T. Soldner, C. A. Ur, W. Urban, D. Wilmsen, E. Wilson

Low-Z boundary of the $N = 88 - 90$ shape phase transition: ^{148}Ce near the critical point
(Submitted).

Publications in conference proceedings

P. Koseoglou, V. Werner, N. Pietralla, S. Ilieva, C. Bernards, A. Blanc, A.M. Bruce, R. B. Cakirli, N. Cooper, G. de France, M. Jentschel, J. Jolie, U. Koester, T. Kröll, P. Mutti, Z. Patel, V. Paziy, Zs. Podolyak, P. H. Regan, J.–M. Régis, O. J. Roberts, N. Saed–Samii, G. S. Simpson, T. Soldner, C. A. Ur, W. Urban, D. Wilmsen, E. Wilson
Lifetime of the 4_1^+ state of ^{148}Ce and its $B_{4/2}$ ratio
Proceedings of the 3rd one-day workshop on New Aspects and Perspectives in Nuclear Physics (2016) 50.

J. Vesic, M. Gorska, A. Jhingan, P. Boutachkov, I. Kojouharov, H. Schaffner, S. Saha, M. Cappellazzo, E. Kluge, **P. Koseoglou**, J. Gerl, H. J. Wollersheim
Charged Particle detectors for LEB-NUSTAR
Proceedings of the DAE-BRNS Symp. on Nucl. Phys. ***61*** *(2016).*

M. Scheck, S. Mishev, V.Yu. Ponomarev, O. Agar, T. Beck, A. Blanc, R. Chapman, U. Gayer, L.P. Gaffney, E.T. Gregor, J. Keatings, **P. Koseoglou**, U. Köster, K.R. Mashtakov, D. O'Donnell, H. Pai, N. Pietralla, D. Savran, J.F. Smith, P. Spagnoletti, G.S. Simpson, M. Thürauf, V. Werner
β DECAY AS A NEW PROBE FOR THE LOW-ENERGY E1 STRENGTH
Acta Phys. Pol. B vol. ***48*** *(2017) No3.*

P. Koseoglou, V. Werner, N. Pietralla, S.Ilieva, M. Thürauf, C. Bernards, A. Blanc, A. M. Bruce, R. B. Cakirli, N. Cooper, L. M. Fraile, G. de France, M. Jentschel, J. Jolie, U. Koester, W. Korten, T. Kröll, S. Lalkovski, H. Mach, N. Mărginean, P. Mutti, Z. Patel, V. Paziy, Z. Podolyák, P. H. Regan, J.-M. Régis, O. J. Roberts, N. Saed-Samii, G. S. Simpson, T. Soldner, C. A. Ur, W. Urban, D. Wilmsen, E. Wilson
The boundary of the N=90 shape phase transition: 148Ce
Journal of Physics: Conference Series ***1023*** *(2018) 012022.*

P. Koseoglou, V. Werner, N. Pietralla, D. Bonatsos
N=90 QSPT: Cerium, neodymium and samarium isotopic chains in the IBM symmetry triangle

Proceedings of the HNPS2018, the 27th Annual Symposium of the Hellenic Nuclear Physics Society, Vol. ***0, 2018*** *(2019).*

M. Rudigier, R. L. Canavan, P. H. Regan, P.-A. Söderström, M. Lebois, J. N. Wilson, N. Jovancevic, S. Bottoni, M. Brunet, N. Cieplicka-Oryńczak, S. Courtin, D. T. Doherty, K. Hadynska-Klek, M. Heine, L. W. Iskra, V. Karayonchev, A. Kennington, **P. Koseoglou**, G. Lotay, G. Lorusso, M. Nakhostin, C. R. Nita, S. Oberstedt, Zs. Podolyak, L. Qi, J.-M.Régis, R. Shearman, P. M. Walker, W. Witt
ISOMER SPECTROSCOPY AND SUB-NANOSECOND HALF-LIVE DETERMINATION IN ^{178}W USING THE NuBALL ARRAY
Acta Phys. Pol. B ***50****, 661 (2019).*

N. Jovančević, M. Lebois, J. N. Wilson, D. Thisse, L. Qi, I. Matea, F. Ibrahim, D. Verney, M. Babo, C. Delafosse, F. Adsley, G. Tocabens, A. Gottardo, Y. Popovitch, J. Nemer, R. Canavan, M. Rudigier, K. Belvedere, A. Boso, P. Regan, Zs. Podolyak, R. Shearman, M. Bunce, P. Inavov, S. Oberstedt, A. Lopez-Martens, K. Hauschild, J. Ljungvall, R. Chakma, R. Lozeva, P.-A. Söderström, A. Oberstedt, D. Etasse, D. Ralet, A. Blazhev, R.-B. Gerst, G. Hafner, N. Cieplicka-Oryńczak, Ł.W. Iskra, B. Fornal, G. Benzoni, S. Leoni, S. Bottoni, C. Henrich, **P. Koseoglou**, J. Wiederhold, I. Homm, C. Surder, T. Kroll, D. Knezevic, A. Dragic, L. Cortes, N. Warr, K. Miernik, E. Adamska, M. Piersa, K. Rezynkina, L. Fraile, J. Benito Garcia, V. Sanchez, A. Algora, P. Davies, V. Guadilla-Gomez, M. Fallot, T. Kurtukian-Nieto, C. Schmitt, M. Heine, D. Reygadas Tello, M. Yavachova, M. Diakaki, F. Zeiser, W. Paulson, D. Gestvang
SPECTROSCOPY OF NEUTRON INDUCED REACTIONS WITH THE ν-BALL SPECTROMETER
Acta Phys. Pol. B ***50****, 297 (2019).*

Publications in progress and technical reports

P. Koseoglou, M. L. Cortés, J. Gerl, T. Habermann, I. Kojouharov, C. Lizarazo, N. Pietralla, H. Schaffner, S. Stoulos, E. Vagena, J. Vesic
Neutron flux mapping in an ion-beam environment employing an improved neutron activation technique using thick foils
GSI Scientific Report 2016 p.184-185 (2017).

W. Witt, **P. Koseoglou**, I. Kojouharev, J. Gerl
Tests of Sunpower CryoTel CT Stirling cooling engine for DEGAS

GSI Scientific Report 2016 p.186-187 (2017).

P. Koseoglou, V. Werner, P.-A. Söderström, M. Lettmann, N. Pietralla, P. Doornenbal, A. Obertelli, N. Achouri, H. Baba, F. Browne, D. Calvet, F. Château, S. Chen, N. Chiga, A. Corsi, M. L. Cortés, A. Delbart, J-M. Gheller, A. Giganon, A. Gillibert, C. Hilaire, T. Isobe, T. Kobayashi, Y. Kubota, V. Lapoux, H. Liu, T. Motobayashi, I. Murray, H. Otsu, V. Panin, N. Paul, W. Rodriguez, H. Sakurai, M. Sasano, D. Steppenbeck, L. Stuhl, Y. L. Sun, Y. Togano, T. Uesaka, K. Wimmer, K. Yoneda, O. Aktas, T. Aumann, L. X. Chung, F. Flavigny, S. Franchoo, I. Gasparic, R.-B. Gerst, J. Gibelin, K. I. Hahn, D. Kim, T. Koiwai, Y. Kondo, J. Lee, C. Lehr, B. D. Linh, T. Lokotko, M. MacCormick, K. Moschner, T. Nakamura, S. Y. Park, D. Rossi, E. Sahin, D. Sohler, S. Takeuchi, H. Toernqvist, V. Vaquero, V. Wagner, S. Wang, X. Xu, H. Yamada, D. Yan, Z. Yang, M. Yasuda and L. Zanetti
Spectroscopy of Sc isotopes between the N = 34 and N = 40 subshell closures
Riken Accelerator Progress Report 51 (2018) p.39.

P. Koseoglou, V. Werner, P.-A. Söderström, M. Lettmann, N. Pietralla, P. Doornenbal, A. Obertelli, N. Achouri, H. Baba, F. Browne, D. Calvet, F. Château, S. Chen, N. Chiga, A. Corsi, M. L. Cortés, A. Delbart, J-M. Gheller, A. Giganon, A. Gillibert, C. Hilaire, T. Isobe, T. Kobayashi, Y. Kubota, V. Lapoux, H. Liu, T. Motobayashi, I. Murray, H. Otsu, V. Panin, N. Paul, W. Rodriguez, H. Sakurai, M. Sasano, D. Steppenbeck, L. Stuhl, Y. L. Sun, Y. Togano, T. Uesaka, K. Wimmer, K. Yoneda, O. Aktas, T. Aumann, L. X. Chung, F. Flavigny, S. Franchoo, I. Gasparic, R.-B. Gerst, J. Gibelin, K. I. Hahn, D. Kim, T. Koiwai, Y. Kondo, J. Lee, C. Lehr, B. D. Linh, T. Lokotko, M. MacCormick, K. Moschner, T. Nakamura, S. Y. Park, D. Rossi, E. Sahin, D. Sohler, S. Takeuchi, H. Törnqvist, V. Vaquero, V. Wagner, S. Wang, X. Xu, H. Yamada, D. Yan, Z. Yang, M. Yasuda, L. Zanetti
First spectroscopy of neutron-rich Sc isotopes using FAIR instrumentation in the third SEASTAR campaign
GSI-FAIR Scientific Report 2017 p.138-139 (2018).

W. Witt, **P. Koseoglou**, P.-A. Söderström, E. Adamska, J. Gerl, I. Kojouharov, N. Pietralla
Characterization of a Sunpower CryoTel CT cooling engine for DEGAS
GSI-FAIR Scientific Report 2017 p.137 (2018).

Curriculum Vitae

Removed in this public version.

Acknowledgments

Firstly, I would like to express my sincere gratitude to my supervisor Prof. Norbert Pietralla for the continuous support of my Ph.D study and related research, for his motivation and immense knowledge. His guidance helped me in all the time of research and writing of this thesis. I could not have imagined having a better advisor and mentor for my Ph.D study.

I am grateful to Dr. Volker Werner, for everything he taught me and his guidance during my Ph.D study. I would like to thank him for all the support and guidance during the analysis presented in this thesis.

I consider myself fortunate for collaborating with these two scientists.

I would like to thank all the members of the Nuclear Physics group of TU Darmstadt for the interesting talks about physics and the nice times we have shared. Specially I would like to thank for their friendship Liliana, Cesar, Marc, Johannes - the best officemate - for the interesting conversations about fast-timing, quantum shape phase transition, movies and more, Waldemar, for the nice time we had in IKP, GSI and of course in Mainz's lab, and P.-A., for the nice conversations, scientific and not, which gave me a lot of times perspectives that I didn't think before.

I thank as well all the secretaries of the Institute, in particular Giovanna, for the countless times they helped me with the administrative procedures.

I would also like to thank Dr. Jürgen Gerl for welcoming me at the Gamma Spectroscopy group at GSI and supporting me on everything that I needed there. Many thanks also to all the members of the group, Ivan, Magda, Henning, Tobias, Michael, Jelena, Sudipta and Tugba for their help, advises and the good times we have shared.

Among all the wonderful people that have become my friends all these years in Darmstadt, I would like to give specially thanks to Sara and Ponsa for sharing all these nice moments.

Θα ήθελα να ευχαριστήσω όλους τους φίλους και τις φίλες μου που ήταν κοντά μου όλα αυτά τα χρόνια, την Σωτηρία, την Θεολογία, την Μιμή, τον Δημήτρη, τον Περικλή και πολλούς ακόμη. Ιδιαίτερα θα ήθελα να ευχαριστήσω τον Ραφαήλ, που χάρη σ'αυτόν δεν πέρασε ούτε μια μέρα που να μην χαμογελάσω, και την Βενετία, που πάντα μου μαθαίνει πράγματα.

Θα ήθελα να ευχαριστήσω την οικογένειά μου για όλη τους την υποστήριξη τα χρόνια που ήμουν μακριά τους, αλλά και για τα θεμέλια που έθεταν όσο μεγάλωνα και πάνω σε αυτά μπόρεσα να χτίσω.

I am also grateful to Prof. Denis Bonatsos and Prof. Rick F. Casten for useful discussions.

I also thank the Helmholtz Graduate School for Hadron and Ion Research for FAIR (HGS-HIRe) and the Federal Ministry of Education and Research (BMBF) for the academic and financial support they provided me at my Ph.D studies.

Erklärung gemäß §9 Promotionsordnung

Hiermit versichere ich, dass ich die vorliegende Dissertation selbstständig angefertigt und keine anderen als die angegebenen Quellen und Hilfsmittel verwendet habe. Alle wörtlichen und paraphrasierten Zitate wurden angemessen kenntlich gemacht. Die Arbeit hat bisher noch nicht zu Prüfungszwecken gedient.

Darmstadt,

_____

Datum und Unterschrift
(Pavlos Koseoglou)